AD A046236

CALCULATIONS OF EARTH PENETRATORS IMPACTING SOILS

Pacifica Technology

P.O. Box 148

Del Mar, California 92014

30 September 1975

(12) 110 P.

Final Report for Period April 1975 — August 1975

CONTRACT No. DNA 001-75-C-0148

R. L.

**APPROVED FOR PUBLIC RELEASE;
DISTRIBUTION UNLIMITED.**

AD No.

DDC FILE COPY

Prepared for

Director

DEFENSE NUCLEAR AGENCY

Washington, D. C. 20305

REPORT DOCUMENTATION PAGE		READ INSTRUCTIONS BEFORE COMPLETING FORM
1. REPORT NUMBER DNA 4189F	2. GOVT ACCESSION NO.	3. RECIPIENT'S CATALOG NUMBER
4. TITLE (and Subtitle) CALCULATIONS OF EARTH PENETRATORS IMPACTING SOILS		5. TYPE OF REPORT & PERIOD COVERED Final Report for Period April 1975—August 1975
		6. PERFORMING ORG. REPORT NUMBER PT-U75-0032
7. AUTHOR(s) R. L. Bjork		8. CONTRACT OR GRANT NUMBER(s) DNA 001-75-C-0148
9. PERFORMING ORGANIZATION NAME AND ADDRESS Pacifica Technology P.O. Box 148 Del Mar, California 92014		10. PROGRAM ELEMENT PROJECT, TASK AREA & WORK UNIT NUMBERS NWED Subtask Y99QAXSB048-02
11. CONTROLLING OFFICE NAME AND ADDRESS Director Defense Nuclear Agency Washington, D.C. 20305		12. REPORT DATE 30 September 1975
		13. NUMBER OF PAGES 112
14. MONITORING AGENCY NAME & ADDRESS(if different from Controlling Office)		15. SECURITY CLASS (of this report) UNCLASSIFIED
		15a. DECLASSIFICATION DOWNGRADING SCHEDULE

16. DISTRIBUTION STATEMENT (of this Report)

Approved for public release; distribution unlimited.

17. DISTRIBUTION STATEMENT (of the abstract entered in Block 20, if different from Report)

18. SUPPLEMENTARY NOTES

This work sponsored by the Defense Nuclear Agency under RDT&E RMSS Code B344075464 Y99QAXSB04802 H2590D.

19. KEY WORDS (Continue on reverse side if necessary and identify by block number)

Earth Penetrating Weapon Calculations in Soil

20. ABSTRACT (Continue on reverse side if necessary and identify by block number)

A set of five computations were conducted which concerned earth pene-trating weapons (EPW) impacting and penetrating two soil types. The pene-trators were 5 feet long, 6.5 inches in diameter, and had 9.25 CRH (tangent) ogival heads, blunted by a 45° half angle cone, 0.5 inches in height. Impact speeds of 500 and 3500 ft/sec were considered. The calculations were carried to 4 feet of penetration in four of the five cases, and to 3 feet in the other. The penetrators were assumed to be rigid bodies.

DD FORM 1473 1 JAN 73 EDITION OF 1 NOV 65 IS OBSOLETE

20. ABSTRACT (Continued)

The computed deceleration and stresses on the penetrator are presented, as well as the deformation field created in the soils. Computing zone sizes of 4.13 and 3 cm were used (1.63 and 1.12 inches).

The conclusion is reached that zoning finer than utilized in this or previous work is required to determine the correct decelerations and stresses on the vehicle. The zone size should be less than 2.5 cm in order to resolve the stress on the blunted nose and to determine the perturbation, which is considerable, on the stress and flow fields further back on the penetrator.
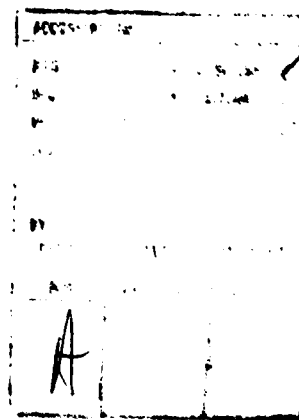
PREFACE

The work on this program was divided into two tasks which can be summarized as:

Task 1. A review of penetrator computations done by others, and

Task 2. A suite of computations utilizing knowledge gained in Task 1 and PacTech techniques.

The work on Task 1 was previous reported in, PT-U75-0013 dated April 30, 1975. This volume includes the computations, analysis and conclusions of Task 2.

1

TABLE OF CONTENTS

1. INTRODUCTION AND CONCLUSIONS

A number of system concepts have recently been proposed which utilize a wide variety of delivery and guidance systems to deliver a tactical nuclear device to a target area and penetrate the ground surface prior to detonation. The phenomenology discussed in this report is a required step in the evaluation of the loads that the vehicle and weapon package must survive prior to detonation.

If even shallow penetration is achieved, prompt radiation is suppressed as both a kill and collateral damage effect. The alteration of the remaining primary kill and collateral damage effects (air blast and ground motion) can be pretested to a limited extent with conventional explosives. The main disadvantage of penetrating weapons (compared to an air burst) is the enhancement of fallout. A slight reduction in air blast kill range is conceded, but ground motions are substantially enhanced.

Systems utilizing deeper penetrations (DOB) are proposed for use when the target is sufficiently hard (such as a runway or buried and surface fortifications) that the kill mechanisms of major interest are the ground motions (including cratering) and debris near or in the crater. The fallout hazard can be substantially reduced by this additional burial.

As the DOB is further increased, one of two phenomena occur. In a medium such as granite or basalt which can support a large amount of bulking, a mound will form. In a weaker material, the initial cavity collapses; and a crater with a radius and volume approximately equal to the cavity radius and volume is formed. In either case the cavity gases are essentially contained so there is no venting. The target kill mechanism is the resulting ground motion. This is by far the cleanest of the proposed EPW systems. However, design feasibility and the number of potential targets have as yet not been clearly defined.

To investigate the phenomenology of earth penetrating weapons (EPW), the Defense Nuclear Agency (DNA), conducted a series of experiments at the Defense Research Establishment Suffield (DRES) Watching Hill Site in Alberta, Canada in mid-July, 1974.[1] Two vertical firings of 400-pound penetrators, five feet in length, 6.5 inches in diameter were made at velocities of 300 and 500 ft/s. The projectiles were instrumented to provide deceleration history, and stress gauges were emplaced in the soil near the projectile's trajectory to measure the stress developed in the target.

Prior to the experiments, the Waterways Experiment Station had collected a great deal of data from nearby borings and excavations, and constructed a recommended set of material property data. In response to the calculators' request, the soil was divided into the four most representative layers. The top three layers turned out to be eight feet thick. Representative property data was supplied by WES for each layer.[2-4] This data was supplied to several calculators,[5-12] who performed detailed predictive calculations of the projectile deceleration, penetration depth, and stresses on the projectile and in the soil for the case of the test with the nominal 500 ft/s impact velocity. The calculations using empirical and analytical techniques are reviewed and compared in Reference 13. Those using finite difference techniques have been reviewed and compared in Reference 14.

From a post-shot excavation made at the shot site, WES discovered that the top 3 to 5 feet of the firing site had been regraded and was composed of fill material, rather than of the top layer (Layer 1) material which they had supposed.[13] In addition, the deceleration measurements disclosed that the material near a depth of 12 feet had characteristics which created especially high decelerations.[1,13]

The computations of this study consider the materials of Layer 1, and of the fill layer discovered postshot. The sequence of computations was laid out so as to permit comparisons between cases in which only one parameter had been altered, which provides an estimate of the relative importance of each parameter. The suite of computations is discussed in Section 2.

The inputs to the computations are discussed in Section 3, including the projectile geometry and mass, and the material properties used for the fill and Layer 1. The computational results are discussed in Section 4.

T'   ults indicate that the fill material produces less dece¹   than the material of Layer 1, so that the sequence of lay   the projectile passes, viz. fill to Layer 1, provides an   , ng sequence of decelerations. This provides a partial explanation for the apparent increase of deceleration with depth, which was initially a puzzling aspect of the experimental measurements. To complete the explanation of this phenomenon the properties of Layer 2 should be more carefully investigated. If, as expected, this results in higher computed decelerations than in Layer 1, a complete interpretation of this phenomenon would result.

All of our computations indicated that a "steady-state" flow field had arisen about the projectile after about 18 inches of penetration, after which the deceleration depends only on the projectile velocity, which changes relatively slowly with depth. Thus, it is necessary to compute only about 24 inches of penetration in a given material to establish the equilibrium value of deceleration at a given velocity. Conducting a sequence of such computations at various velocities would therefore provide a means to compute the projectile deceleration and loadings as a function of velocity for a given medium.

The zoning study indicated that three centimeter zones are not small enough to permit an accurate computation of the deceleration

and loading for projectiles with the blunted nose tips considered in this study. The inadequacy becomes worse at higher impact velocities. The zoning study should be continued to much smaller zone sizes to determine the required zoning fineness.

In Cases 2 through 5, the calculations utilized fits to the data furnished by WES, and did not include frictional forces between the soil and projectile. Using the material property data in this way will ultimately lead to a definite computed deceleration when sufficiently fine zones are used. Although these final values of deceleration are unknown at present, the values generated in this study suggest that little or no friction will have to be added to bring the computed decelerations into correspondence with the measured values. This conclusion of course applies only to the materials treated in this study, namely fill and Layer 1 material. In addition, it assumes that the measurements of deceleration were accurately conducted, and it should be pointed out that the measurements contain inexplicable oscillations which are still under investigation.

The calculations described herein, a first exploratory cut, were funded at the level of a sixth of a man-year. They reveal that finer zoning should be used to obtain quantitative improvements in the calculated stress on, and deceleration of, a blunted-tipped projectile. The computational techniques employed in this study have proved to be so efficient that it is easily feasible to use much finer zoning. All cases studied used 1500 cells and required expenditures of between 306 and 625 seconds of central processing (CPU) time on the CDC 7600 to compute four feet of penetration (5.1 to 10.4 minutes). Cells near the penetrator were integrated for 4000 to 8000 cycles, whereas those far from the penetrator required only 300 to 600 cycles. The code contains an automatic subcycling routine which selects the optimum region to be subcycled to advance the solution farthest in real time for a given expenditure of computer time. In addition, the use of automatic rezoning permitted the problems to be run to completion without manually rezoning the computing grid.

2. THE CALCULATIONS

Five calculations were conducted in this study, all using the vehicle geometry described in Section 3.1.

Case 1.

The soil used in this calculation had the properties originally specified by WES for Layer 1 of the Watching Hill Site. The impact velocity was 500 ft/sec. Friction was included in the form

$$|\tau| = \text{Min } \{0.6\sigma_n, \ 0.6 \ \frac{\gamma(\sigma_n)}{\sqrt{3}}\} \tag{2.1}$$

τ being applied so as to oppose the differential velocity between the soil and projectile. Near the penetrator, the computing zones were initially square in cross-section having sides of 4.1275 cm. This computation modeled as closely as possible that conducted by CRT.[10] Toward this end the CRT material property fit was used.

Case 2.

The specifications for this calculation are identical with those of Case 1 with a single exception. No friction was included in the model.

Case 3.

This calculation is identical with Case 2 in every respect except that the soil had the characteristics of the fill material which was discovered at the top of the Watching Hill Site after the shot.[13] The material properties of this material, and the fit used in the calculation are discussed in Section 3.2.

Case 4.

This calculation is identical in all respects with Case 3, except that an impact velocity of 3500 ft/sec was used.

Case 5.

This calculation was identical in all respects with Case 2, with the single exception that the computing zones near the vehicle were initially 3 cm in height and width.

TABLE 2.1

SUMMARY OF COMPUTATIONS					
Case	1	2	3	4	5
Friction	yes	no	no	no	no
Soil	Layer 1	Layer 1	Fill	Fill	Layer 1
Velocity (ft/s)	500	500	500	3500	500
Zone size (cm)	4.1275	4.1275	4.1275	4.1275	3
Decel (g's)	191.2	89.5	59.5	1982	81.9
Approximate measured deceleration (g's)*	75	75	20-90**	NA	75

*From Figure 5.1-1 (See Reference 13)

**There is an unexplained oscillation in the data from the 500 ft/s
test while the projectile is traversing the fill. The estimated
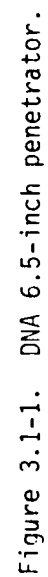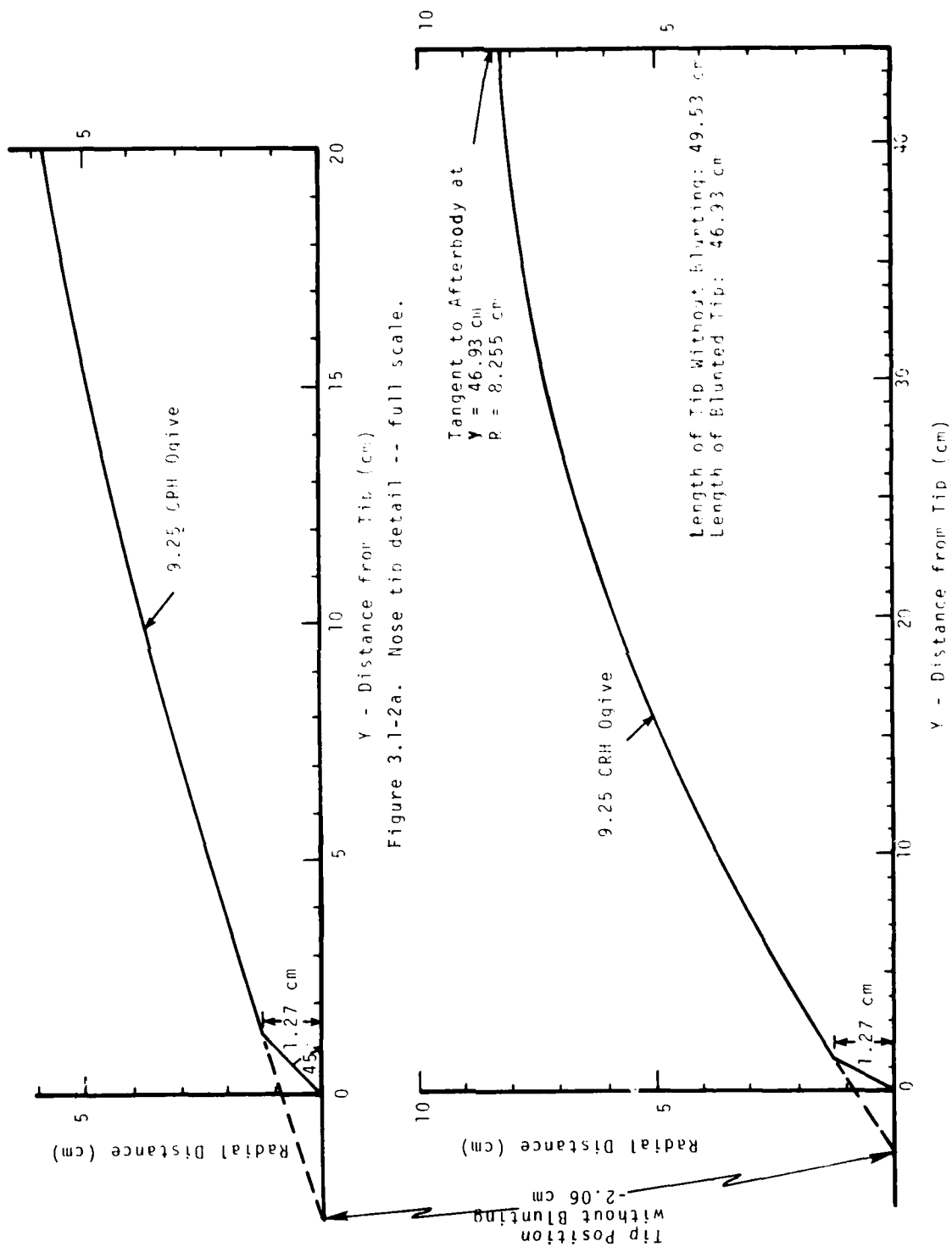average value is 50 g's.

3. INPUTS TO THE COMPUTATIONS

3.1 VEHICLE GEOMETRY

Figure 3.1-1 shows a drawing of the actual vehicle together with the manufacturing tolerances.[1] The cylindrical afterbody has a diameter of 6.5 in., and a length of 41.524 ± .03 in. The nose is ogival in character, being specifically a 9.25 caliber radius head (CRH) tangent. This means the outline of the nose is generated by a circle of radius 9.25 projectile diameters or 60.125 in. The circle is tangent to the afterbody at the point where it intersects it. As the figure shows, this implies that the circle center is at the same station as the forward part of the afterbody, and is offset from the vehicle centerline by 8.75 calibers or 56.875 in. If the nose were a complete ogive, it would have a length of 19.5 in. However, the nose is blunted by the addition of the conical tip 0.5 in. high having a 45° half angle. Milling off the conical tip reduces the length of the ogive by 2.602 cm, or 1.024 in., leading to an actual nose length of 18.476 in. The length of the afterbody plus the length of the blunted nose thus totals a nominal 60 in. As seen from the figure, the manufacturing specifications are that vehicle be 60.00 ± .06 in. in length.

Figure 3.1-2 shows two detailed drawings of the nose geometry. Figure 3.1-2a is a full-scale drawing of the first 20 cm of the nose. Figure 3.1-2b is full scale in the radial direction, but the Y-scale (distance from tip) is compressed by a factor of 2. In the calculations to be presented, the projectile is treated as a rigid body so that it always preserves the dimensions and configuration shown in the figure.

The weight of the vehicle is a nominal 400 lbs., and the equivalent value of 181,436 grams is used in the calculation. In the calculation, the afterbody was terminated flush at a distance of 60 in. from the nose tip. This neglects the screw-in insert

Figure 3.1-1. DNA 6.5-inch penetrator.

Figure 3.1-2a. Nose tip detail -- full scale.

Figure 3.1-2b. Nose tip geometry (Y: half scale, R: full scale).

12

shown in Figure 3.1-1. However, it was observed that the soil separated from the vehicle in the computation and contacted no portion of the afterbody, so that the flush termination did not influence the computed deceleration.

3.2 MATERIAL PROPERTIES OF THE FILL LAYER

3.2.1 The Data

Based on experimental data provided by WES,[15] an analytical
fit to the material properties of the fill layer was conducted
for use in these computations. The data transmitted by WES was a
series of recommended curves, based on the results of experiments
made on several samples. The final recommendations were constructed
using averages of the test results, combined with judgment as to
how the test data related to the material properties in situ.

Figures 3.2-1 through 3.2-4 contain the WES recommendations,
concerning the dynamic constitutive properties of the backfill
material encountered near the ground surface in DNA Penetration
Test 06, which was conducted near the PRAIRIE FLAT HEST TEST
Site at the Watching Hill Blast Range of the Defense Research
Establishment, Suffield (DRES), Alberta, Canada.

The data transmitted by WES consisted of the following:

1. A stress-strain loading curve in uniaxial strain
    up to a peak stress of $\sigma_z = 3.41 \times 10^8$ dyne/cm^2
    (4946 psi).

2. Stress-strain curves for unloading in uniaxial
    strain, beginning at various points on the UX loading
    curve. Three such curves were provided which begin
    on the loading curve at σ_z = 400, 1000, and 4946 psi.

3. Stress difference $(\sigma_z - \sigma_r)$ vs. mean stress curves
    for loading in uniaxial strain up to a mean stress
    of 425 psi.

4. Curves of stress difference vs. mean stress for
    unloading in uniaxial strain. Two such curves were
    provided corresponding to unloading from the uniaxial
    strain loading curve at σ_z = 400 and 1000 psi.

14

5. A failure envelope couched in terms of principal stress difference as a function of mean stress as deduced from triaxial strain tests. Data was presented up : a mean stress of 1650 psi.

The curves in Figur 3.2-1 through 3.2-4 are in terms of live stresses (i.e., the in situ state of stress corresponds to the origin of coordinates in the plot). The strains in these figures are expressed as engineering strains. Both stress and strain are considered positive in compression.

The depth of the backfill in the immediate vicinity of Test 06 varies from 3 to 5 feet. A backfill layer thickness of 4 feet was recommended by WES[15] for use in these calculations simulating the penetration event. Below the backfill, the recommended pretest Layer 1 properties still appear to be appropriate for the 4 to 8 foot depth range.

Laboratory test results from undisturbed samples obtained from the backfill zone in the post-test field investigation were used as the basis for developing the properties contained in Figures 3.2-1 through 3.2-4. These tests consisted of uncon-solidated-undrained uniaxial strain (UX) and triaxial compression (TX) tests. The test specimens exhibited a rather broad range of scatter in their water contents and densities. This is not unusual for a material of this type placed without any special controls. It is WES's judgment that the backfill should be treated as a uniform layer with the following representative composition properties:

Water Content (weight of H_2O per total wet weight) = 18%

Wet Unit Weight = 97 lb/ft^3 = 1.55449 g/cm^3

The triaxial tests conducted by WES contain uncertainties due to end-cap friction. The axial and radial strains, ε_a, and of ε_r are respectively determined from the overall shortening of the

15

specimen, and the radial deformation measurement at the specimen mid-
point. To accommodate the end-cap uncertainty, WES computed the
volumetric compaction, $\Delta v/v_0$ in two different ways. The first way
assumes that end-cap friction is negligible, and that the cylin-
drical specimen remains cylindrical. This leads to the equation

$$\frac{\Delta v}{v_0} = \varepsilon_a + 2\varepsilon_r - 2\varepsilon_r\varepsilon_a + \varepsilon_r^2 (\varepsilon_a - 1) + \ldots \qquad (3.2\text{-}1)$$

The second way assumes that high end-cap friction exists and that
the deformed specimen takes the shape of a double conic, pinched
at the midpoint. The volumetric compaction in this case is
calculated from

$$\frac{\Delta v}{v_0} = \varepsilon_a + \varepsilon_r - \varepsilon_r\varepsilon_a + \frac{\varepsilon_r^2}{3} (\varepsilon_a - 1) + \ldots \qquad (3.2\text{-}2)$$

When applied to a given set of data for the shear phase of a triaxial
test, the first equation will tend to minimize apparent compaction
and maximize apparent dilation. The latter formula has the opposite
effect. Examining the triaxial data with these factors in mind,
WES concluded that the backfill materials tested definitely do not
exhibit any significant dilation during straining in shear. They
either compact or remain at approximately constant volume depending
on which deformed shape is assumed. In view of this, an elastic,
ideally-plastic (EIP) type of constitutive model with a non-
associated flow rule is believed to be physically more appropriate
than one with an associated flow rule.

In constructing the recommended curves shown as Figures
3.2-1 through 3.2-4, WES intentionally made the curves stiffer
than any of the data actually taken. This was done to account
for differences in initial density, loading rate, and possible
sample disturbance. These changes manifest some of the judgments
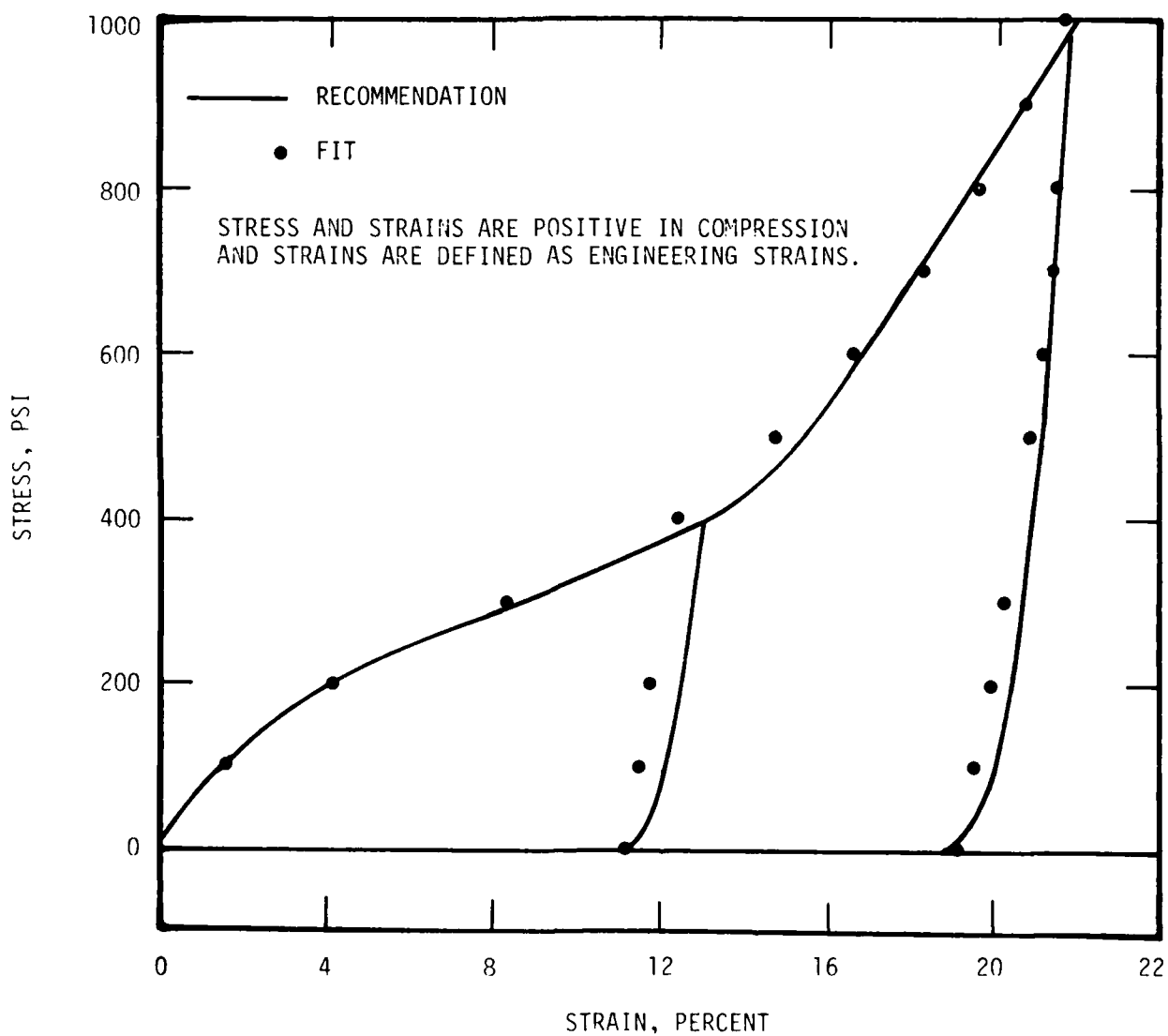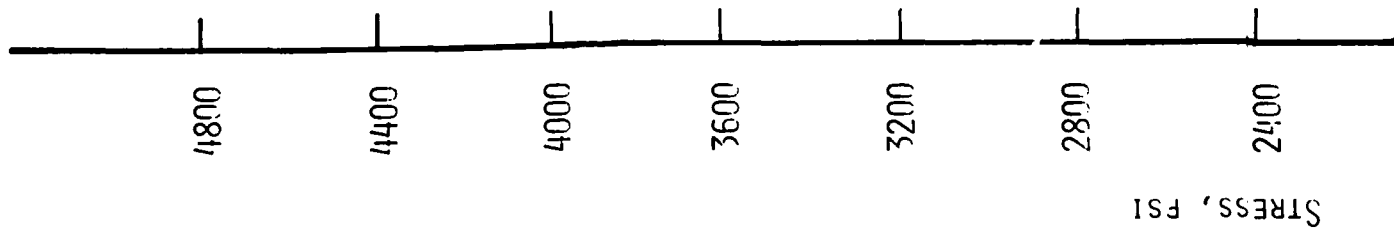which WES had to apply in formulating these recommended curves.

16

Figure 3.2-1. Preliminary recommendation of a vertical stress vs. vertical strain curve for the backfill material in a state of uniaxial strain.

Point T:

$\sigma_z = 4946$ psi $= 3.41 \times 10^8$ dynes/cm^2

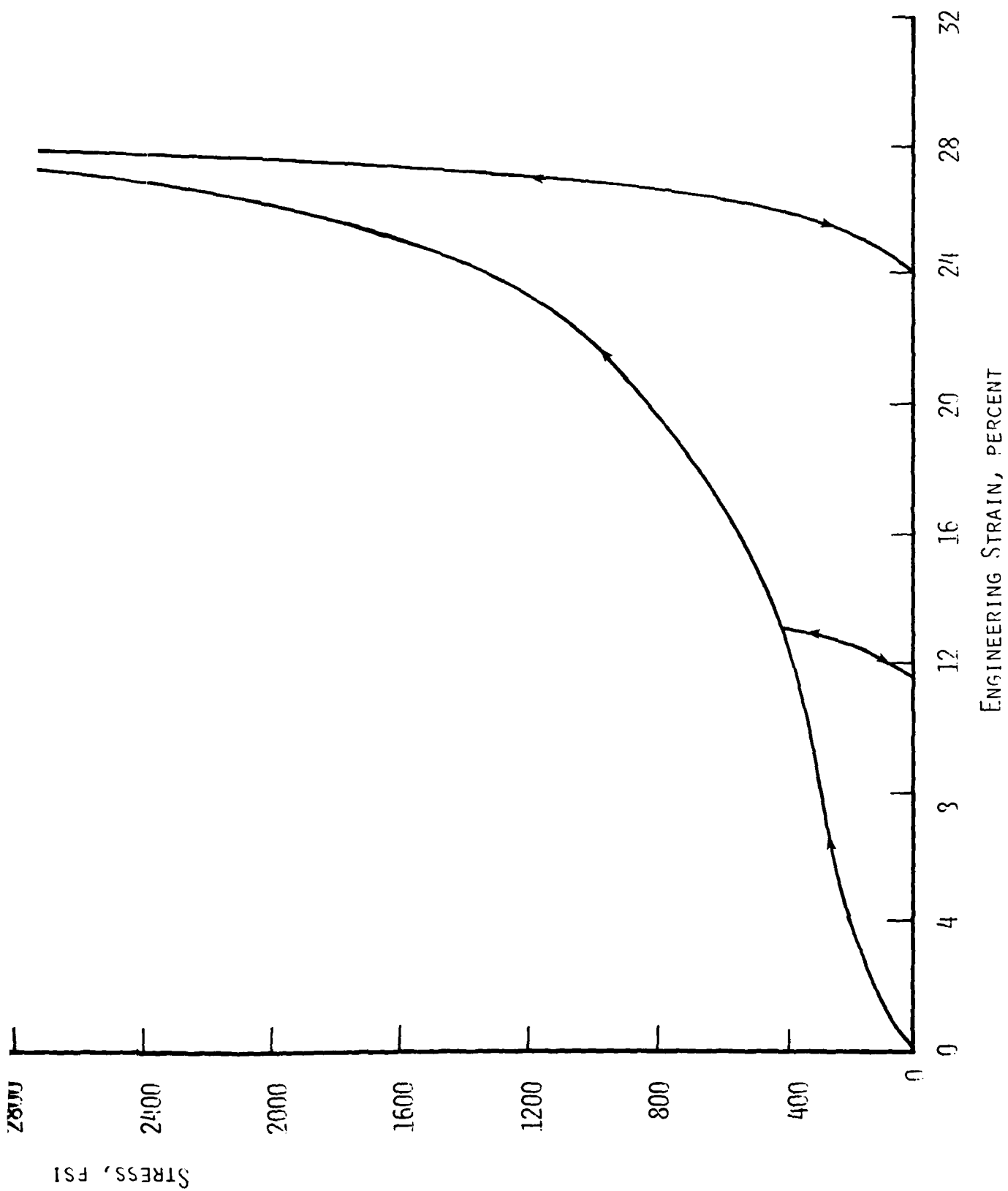$\varepsilon_z = 0.2813$

STRESS, PSI

4800 4400 4000 3600 3200 2800 2400
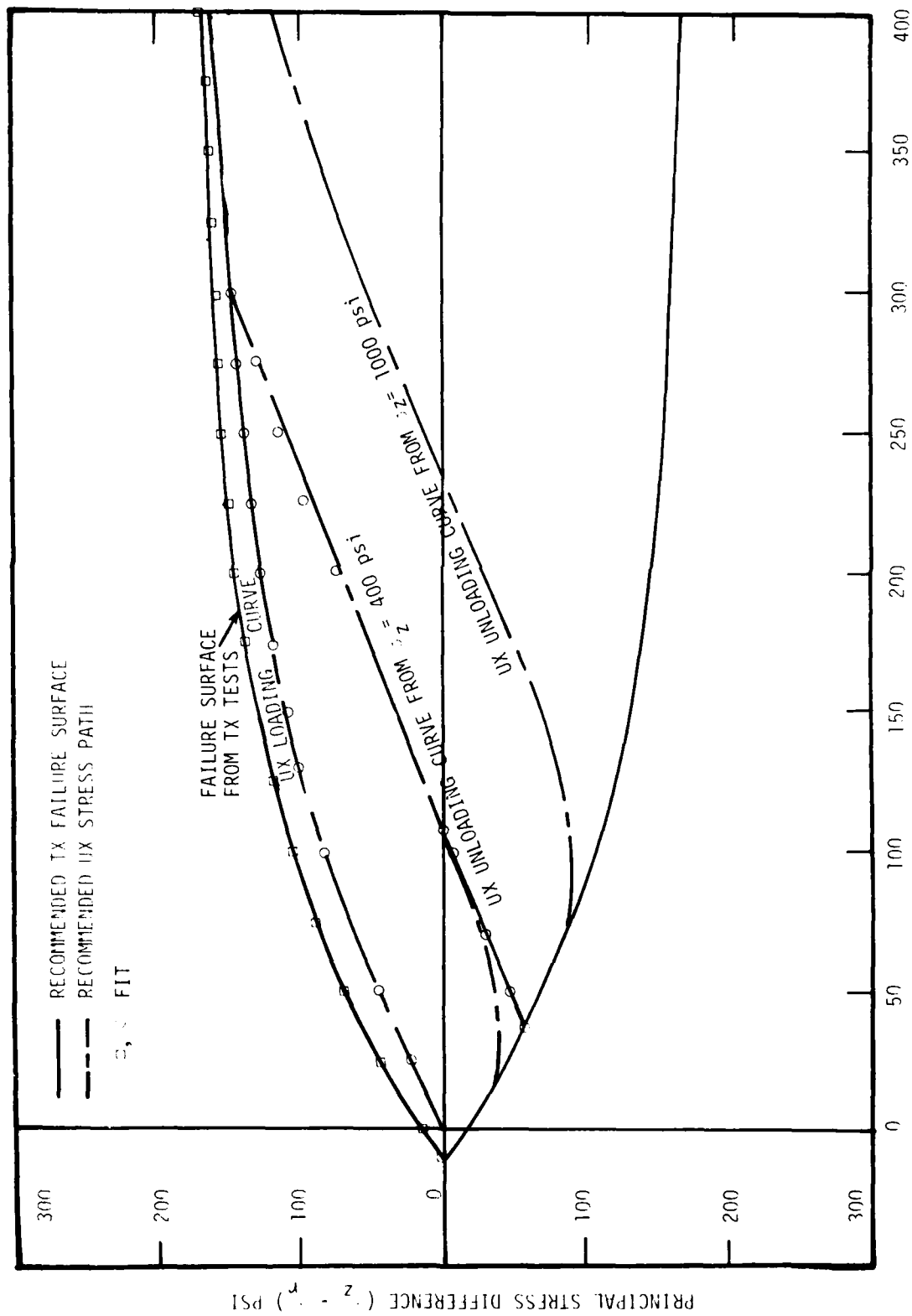
Figure 3.2-2. Recommendation of vertical stress vs vertical strain for the backfill material in a state of uniaxial strain.

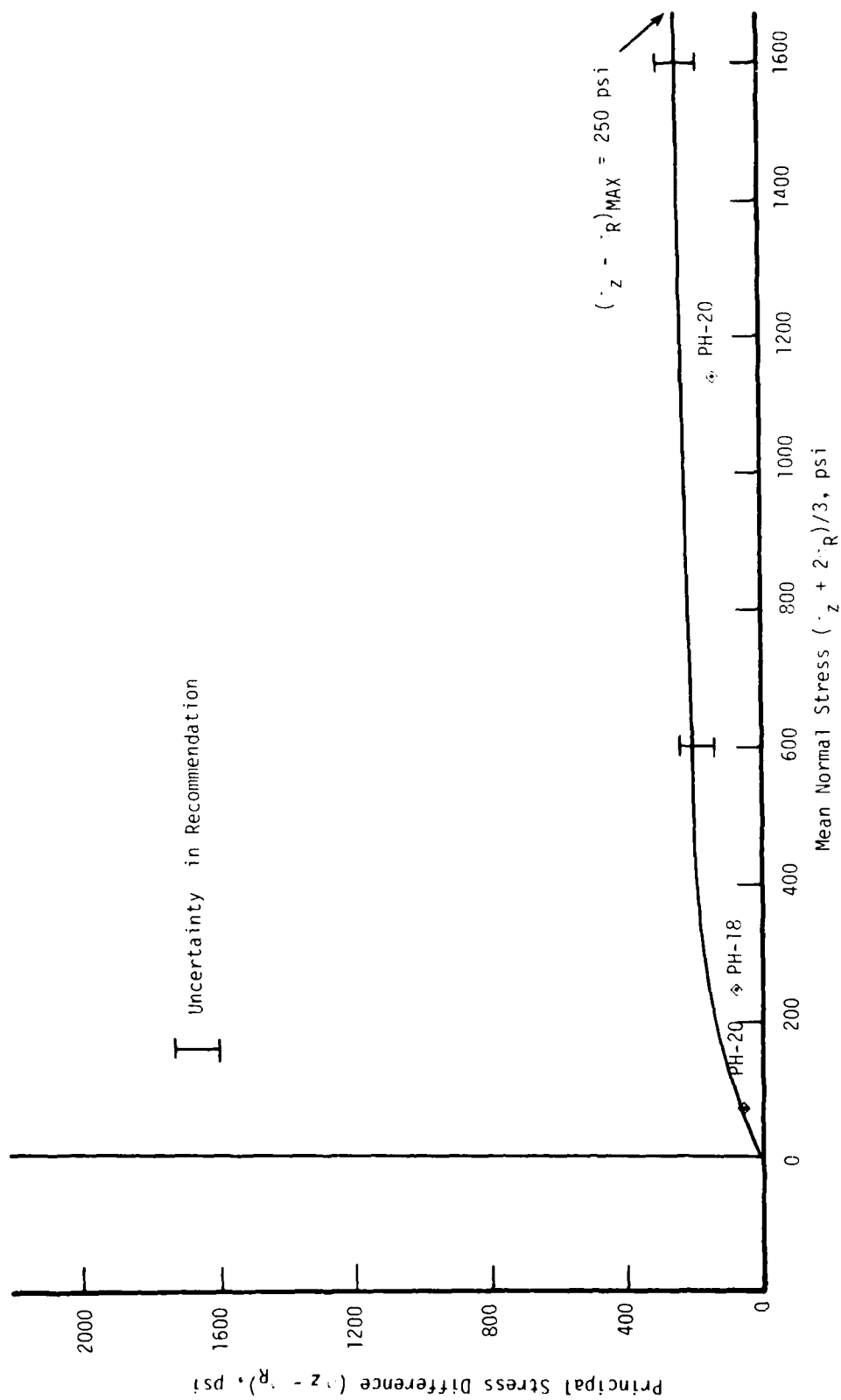Figure 3.2-3. Preliminary recommendation of UX stress path and TX failure surface for the backfill.

Figure 3.2-4. Recommendation of triaxial test failure surface for the backfill.

20

The recommended triaxial strain-based failure surface for the backfill material (Figures 3.2-3 and 3.2-4) represents a considerable reduction in shear strength from that of the pretest Layer 1 material. This curve was intentionally set above the available triaxial test data points because the test specimens had water contents higher than those judged to be representative of the entire stratum.

The stress paths for the uniaxial strain test shown in Figure 3.2-4 correspond to the uniaxial stress-strain curves shown in Figure 3.2-1. No stress path data were available on which to base the recommended curves, however, they are qualitatively similar to those recommended for the pretest Layer 1 material and the initial slope correlates with the expected values calculated from the initial moduli data extractable from the individual test results.

3.2.2 The Fit

The experimental data provided by WES are not sufficient to determine the equation of state of the material completely. The penetration process causes the soil to traverse different stress-strain paths than those along which data were provided. It is therefore necessary to make additional assumptions as to the constitutive relations in order to generate a material property model which applies to the region of stress-strain space encountered during penetration. In the absence of further data, these assumptions must be arbitrary to a great extent. They are restricted only by the requirements that the constitutive relations must satisfy the criteria of uniqueness and thermodynamic consistency. However, these requirements are very broad, as they must be to encompass every material in the world!

Specifically, the additional major assumptions were made that the loading and unloading bulk moduli are functions only of pressure, and that the loading and unloading rigidity moduli are functions only of $\sqrt{J_2}'$. Using these assumptions, the loading and unloading curves in uniaxial strain are considered to be reference curves which provide data to fit the loading and unloading moduli.

The reference curves used to find the loading moduli are the UX σ-ε loading curves, and UX Y-P loading curves.* As shown in Figure 3.2-2, the σ-ε loading curve provides data up to σ_z = 4946 psi (3.41×10^8 dynes/cm^2). The curve was arbitrarily extrapolated to higher values of stress by assuming continuity of the first derivative, and constancy of the second derivative. The UX Y-P loading curve is shown in Figure 3.2-3.

*To simplify reference to the data, the term, "UX σ-ε curves", refers to the stress-strain paths taken in uniaxial strain (Figures 3.2-1 and 3.2-2), while "UX Y-P" refers to the stress difference vs. mean stress plots (Figure 3.2-4).

22

It extends only up to a mean stress of 425 bars, so that it had
to be arbitrarily augmented above that mean stress. At a mean
stress of 425 bars, it falls about 5 psi beneath the failure
surface. It was assumed that it remained offset by 5 psi from
the failure surface which is given up to a mean stress of 1650 psi
in Figure 3.2-4. Both the failure surface and UX Y-P loading
curve were further augmented by assuming that the failure surface
approaches the value of 250 psi asymptotically at high mean
stress. The offset of 5 psi between the UX Y-P loading curve
and the failure surface was preserved throughout the entire region
of higher mean stress.

The reference curves used to determine the unloading moduli
are 1) the unloading UX $\sigma-\varepsilon$ curve shown in Figure 3.2-2, which is
tangent to the loading curve at 4946 psi, and 2) the UX Y-P curve
shown in Figure 3.2-4 which encounters the UX loading curve at
σ_z = 1000 psi. It was assumed that curve 1) is the limiting
unloading curve, and that it is tangent to the UX loading curve at
σ = 4946 psi, (Point T in Figure 3.2-2). If UX loading to a
higher stress occurs, the material will unload back along the
loading curve until Point T is reached, and it will then follow
the limiting unloading curve. Point T is the point at which all
voids are irreversibly crushed out.

Data on the Y-P unloading curve was provided only up to a
mean stress of 425 psi, and had to be arbitrarily augmented at
higher mean stress. This was done in a series of steps. First,
the augmented UX Y-P loading curve was used to determine the
stress difference which occurs in UX strain when σ_z = 1000 psi.
The reference unloading curve was then extrapolated from a mean
stress of 425 psi to this point, preserving the continuity of
its first derivative at P = 425 psi.

Having specified these curves up to a mean stress of 1000 psi,
it is possible to determine the rigidity modulus up to the stress

difference which occurs at 1000 psi. There remains the problem of defining it at higher values of the stress difference, or more generally, higher values of $\sqrt{J_2}'$. This was done in the following way. It was assumed that at a mean stress of 4946 psi, the voids are all crushed out, and the loading and unloading curves should be tangent at that point and identical at higher mean stresses. Thus, both G and its derivative with respect to $\sqrt{J_2}'$ are defined at Point T. The previous procedure defined both G and its first derivative with respect to $\sqrt{J_2}'$ at a mean stress of 1000 psi. Therefore, a simple polynomial fit was used to span the gap, preserving the continuity of G and its first derivative in the interval up to the point at which the voids are crushed out.

To construct our material model, we first fit $\sigma_z^L(\epsilon_z)$ and $\sigma_z^U(\epsilon_z)$ which are the loading and unloading curves in uniaxial strain. In this notation, it is assumed that the strain occurs in the Z direction, ϵ_z is the strain in that direction, and σ_z the associated stress. We next use the uniaxial strain loading and unloading curves to fit $Y^L(P)$ and $Y^U(P)$, where Y is defined through

$$Y^2 = \frac{3}{2} s_{ij} s_{ij} \tag{3.2-3}$$

so that in the case of uniaxial strain.

$$Y = |\sigma_z - \sigma_r| \tag{3.2-4}$$

On loading, σ_z is always greater than σ_r, and on unloading we conduct the fit only to the point where Y first becomes zero. Thus, σ_z is greater than σ_r throughout this entire loading-unloading cycle. For this loading and unloading region, we then have the identity

$$\sigma_z = P + \frac{2}{3} Y \tag{3.2-5}$$

This identity, and the fits of $\sigma_z(\epsilon_z)$ and $Y(P)$, permit us to solve for P as a function of ϵ_z. Since ϵ_z depends only on the volumetric strain in these uniaxial strain tests, this provides us with our pressure-volume relation.

Because the engineering strain, as defined by

$$\epsilon_z = \frac{v_0 - v}{v_0} \tag{3.2-6}$$

is used, the bulk modulus is prescribed by

$$K = - v \frac{\partial P}{\partial v} = \frac{d\sigma_z}{d\epsilon_z} \frac{1 - \epsilon_z}{1 + \frac{2}{3}\frac{dY}{dP}} \tag{3.2-7}$$

To obtain the rigidity modulus from these fits, we start with the definition

$$d\sigma_z = - (K + \frac{4G}{3}) \frac{dv}{v}$$

$$dP = - K \frac{dv}{v} \tag{3.2-8}$$

where $\frac{dv}{v}$ is the true incremental strain as used in our computations. This leads to the definition

$$G = \frac{3}{4} v \left(\frac{dP}{dv} - \frac{d\sigma_z}{dv}\right) = \frac{1}{2} \frac{(1 - \epsilon_z)\frac{dY}{dP}}{1 + \frac{2}{3}\frac{dY}{dP}} \frac{d\sigma_z}{d\epsilon_z} \tag{3.2-9}$$

To obtain the loading rigidity modulus, the loading fits are used, and the unloading modulus utilizes the unloading fits.

This approach permits us to conduct fits of the data itself, and then deduce the moduli from the fit. In conducting the fit it is necessary to insure the continuity of both the function and its first derivative. This is accomplished by breaking the independent variable into regions, conducting fits in each region

wherein the function and its first derivative are piece-wise
continuous, and matching the function and its first derivatives
at the intersection. Quadratic functions are especially suitable
for this purpose, because they can easily be inverted.
The approach has the virtue that if a loading-unloading calculation
in UX strain is conducted, the experimental data will be precisely
reproduced. Whereas the resulting moduli are continuous, their
derivatives may be discontinuous. However, the discontinuties
in the moduli derivatives leads to no difficulties.

The data provided by WES for the failure locus is
$(\sigma_z - \sigma_r)$ as a function of the mean stress. To accommodate this
description, we define a variable, Y through the relation

$$s_{ij} \, s_{ij} = \frac{2}{3} Y^2 \qquad\qquad (3.2\text{-}11)$$

where s_{ij} are the physical components of the stress deviator.
Because of the definition

$$\sqrt{J_2}' = \sqrt{\frac{1}{2} \, s_{ij} s_{ij}} \qquad\qquad (3.2\text{-}12)$$

Y and J_2' are related through

$$Y = \sqrt{3} \, J_2' \qquad\qquad (3.2\text{-}13)$$

For loadings in which the two minor principal stresses are equal,
Y becomes just the difference between the greatest and the least
principal stresses. Thus, for the case of uniaxial strain, or
triaxial loading, we have the relation

$$Y = |\sigma_z - \sigma_r| \qquad\qquad (3.2\text{-}14)$$

We fit Y as a function of mean stress by means of a series
of quadratic expressions, maintaining continuity of the function

and its first derivative. The fit has the general form

$$Y_F = B_0 + B_1 P + B_2 P^2 \tag{3.2-15}$$

The coefficients used in the fit are given in Table 3.2-1. The I-th set of coefficients is used when

$$PT(I - 1) \le P < PT(I), \tag{3.2-16}$$

The set corresponding to $I = 1$ is used when $P < PT (1)$.
In the case of unconfined compression, the two minor stresses are zero, and Y and P are related through

$$\sigma_z - \sigma_r = 3P \tag{3.2-17}$$

If σ_z is greater than σ_r, this has the form

$$Y_F = 3P \tag{3.2-18}$$

The unconfined yield stress is prescribed by the intersection of the line defined by Equation (3.2-18) and the parabolic section defined by Equation (3.2-5) with $I = 2$. The unconfined yield stress and corresponding mean stress found in this way are

$$Y_y = 1.5712 \times 10^6 \text{ dynes/cm}^2 = 22.79 \text{ psi}$$
$$\tag{3.2-19}$$
$$P_y = 5.376 \times 10^6 \text{ dynes/cm}^2 = 7.60 \text{ psi}$$

For a mean stress more tensile than 10 psi $= 6.894757 \times 10^5$ dynes/cm^2 Y is set uniformly to zero.

TABLE 3.2-1

		CONSTANTS FOR THE FIT TO THE FAILURE LOCUS		
I	P(I)	$B_0(I)$ (dyne/cm^2)	$B_1(I)$ dimensionless	$B_2(I)$ (cm^2/dyne)
1	-6.89475727+05	0.00000000	0.00000000	0.00000000
2	5.17106800+06	9.12224844+05	1.28626876+00	-5.33761018-08
3	1.20658252+07	1.35345691+06	1.11561462+00	-3.68752424-08
4	2.06842720+07	5.58223081+06	4.14663989-01	-7.82830145-09
5	2.75790292+07	1.11860145+07	-1.27176087-01	5.26957500-09
6	5.51580585+07	5.11682356+06	3.12954776-01	-2.70987310-09
7	4.48159224+08	1.33072241+07	1.59754809-02	-1.77977936-11
8	9.99999998+19	1.68818520+07	2.29902400-05	0.00000000

5.17+6 denotes 5.17×10^6, etc.

3.3 MATERIAL PROPERTIES OF LAYER 1

Since Case 1 was supposed to reproduce the calculation previously conducted by CRT for the Layer 1 as closely as possible, the CRT fit to the material properties[10] was used. To minimize the variations between Case 1 and Cases 2 and 5, the same fit was used in those calculations also.

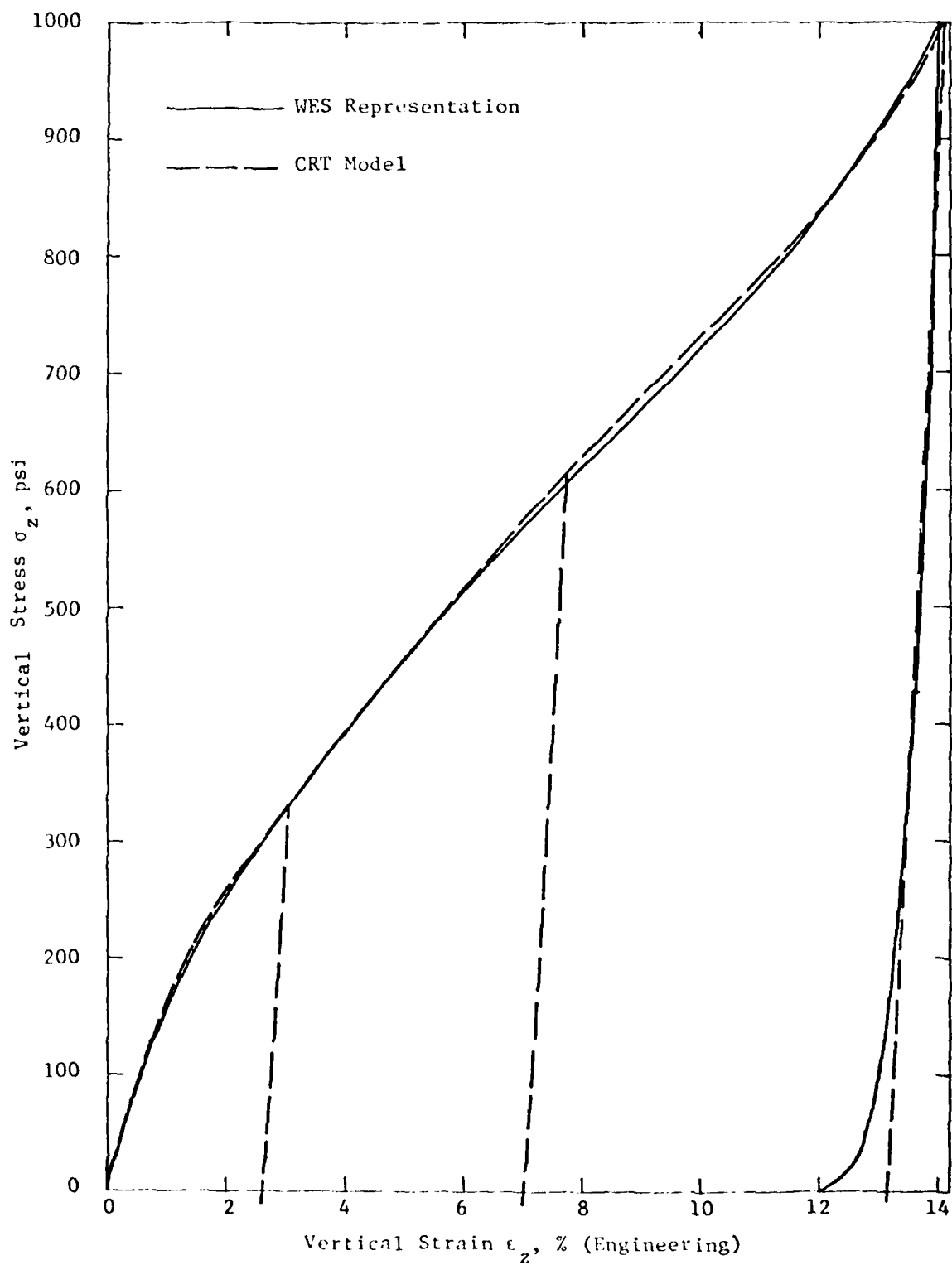As discussed more fully in Reference 14, the data on which this fit was based was supplied by WES. Figures 3.3-1 through 3.3-6 summarize the WES data, and compare it with the CRT fit.

Figure 3 3-1. Uniaxial Strain Load-Unload Paths for Layer 1.
(σ_z to 1000 psi)
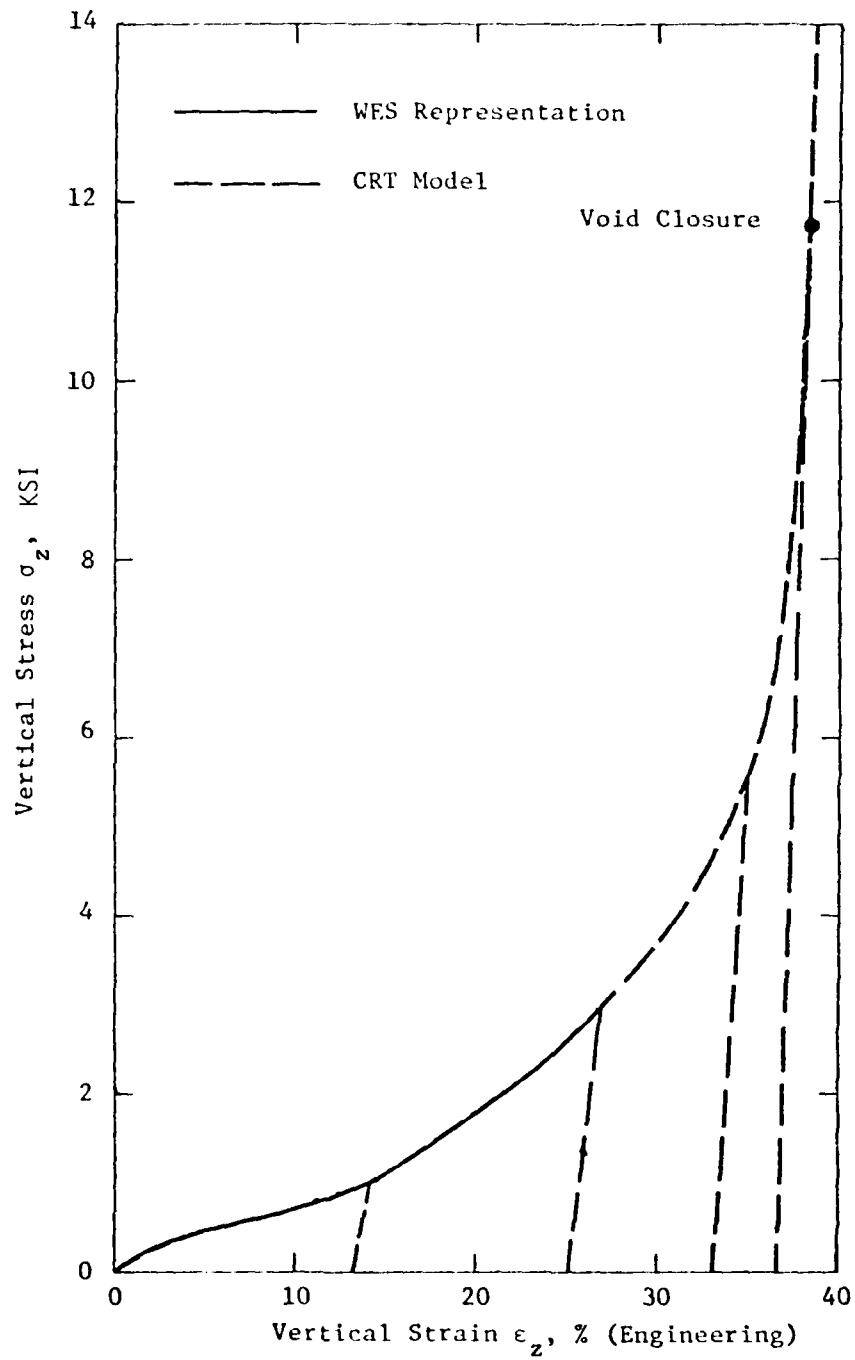
Figure 3.3-2. Uniaxial Strain Load-Unload Paths for Layer 1.
(σ_z to 14 KSI)
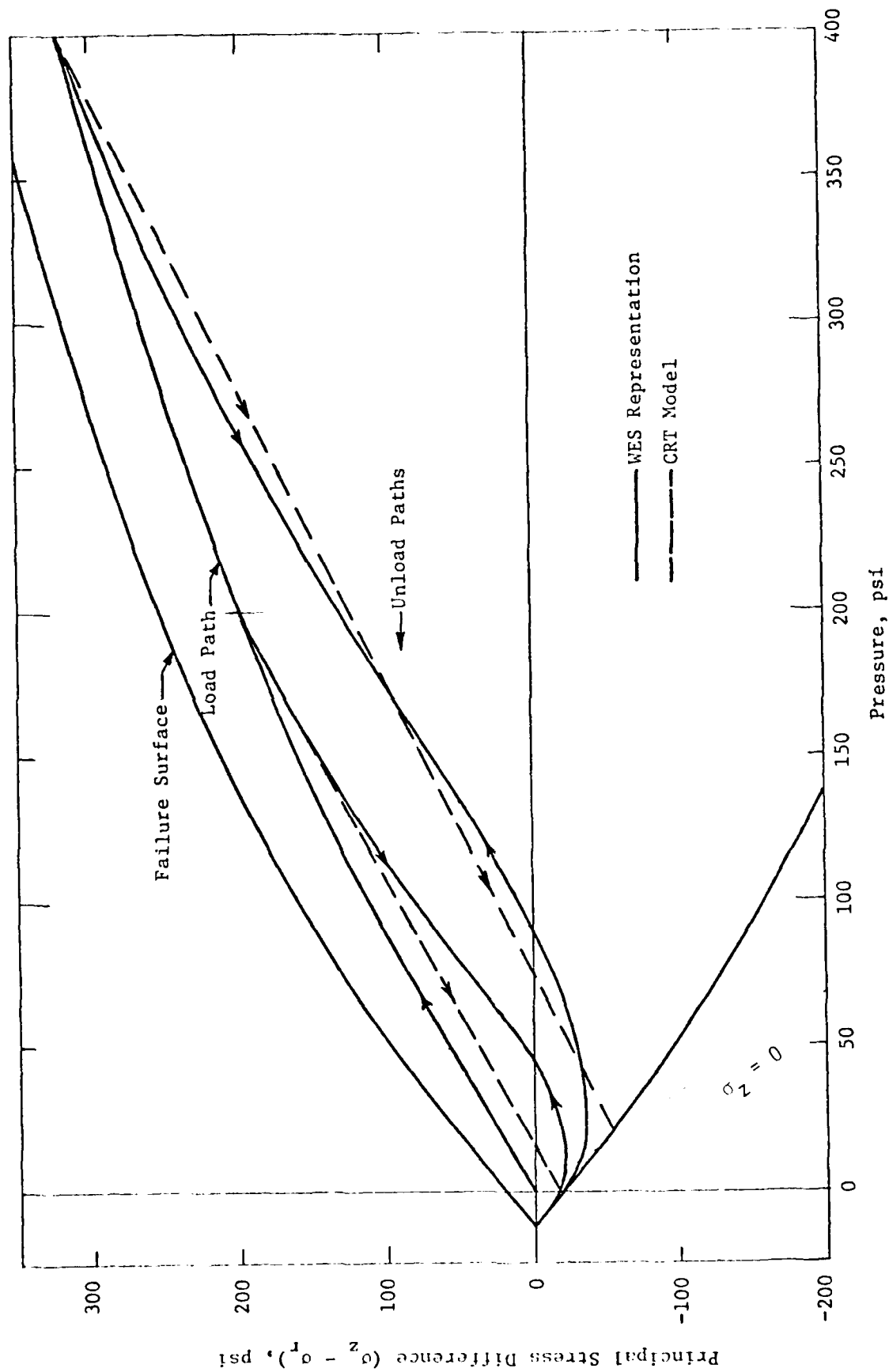
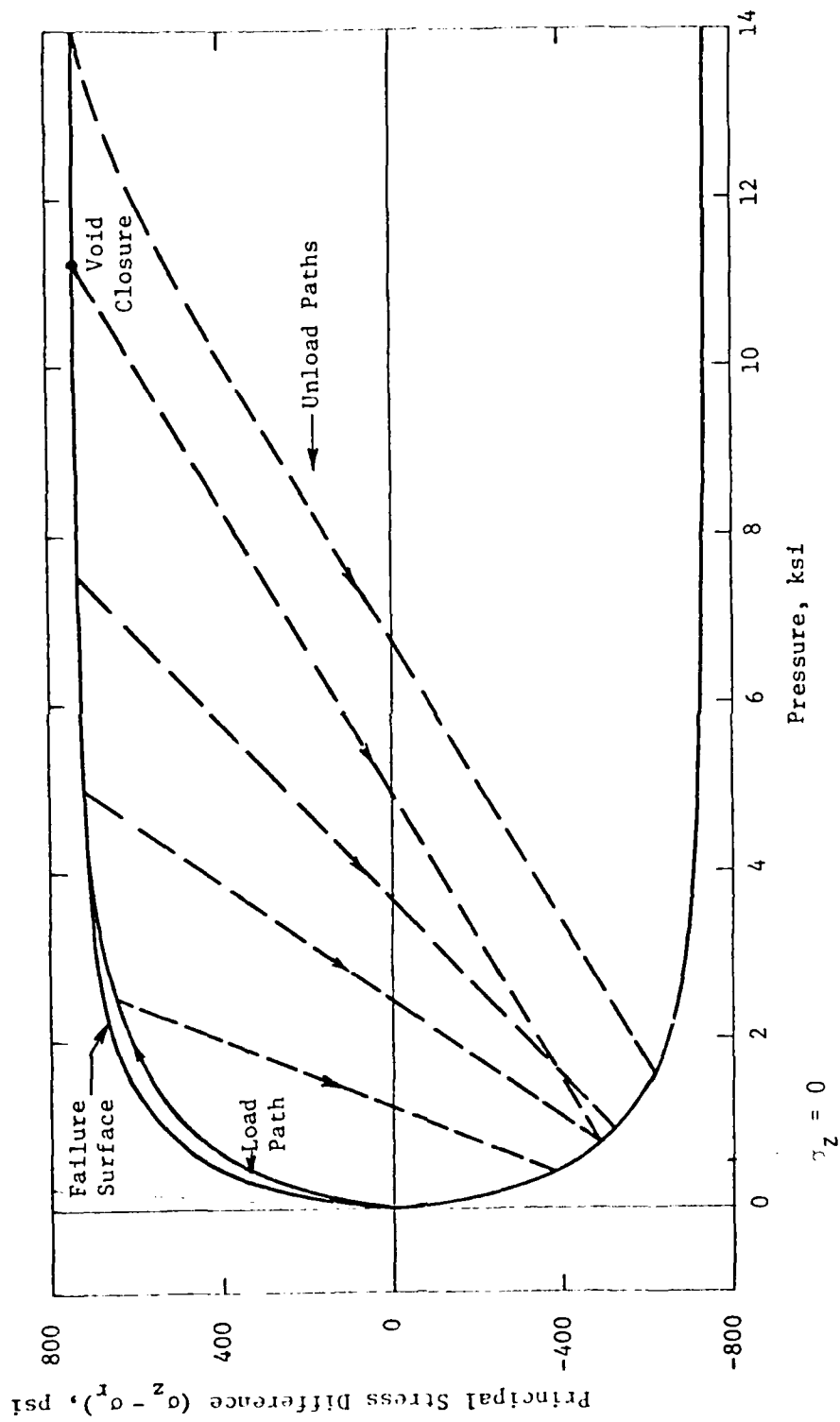Figure 3.3-3. Uniaxial Strain Stress Paths and Failure Surface for Layer 1 (P to 400 psi)

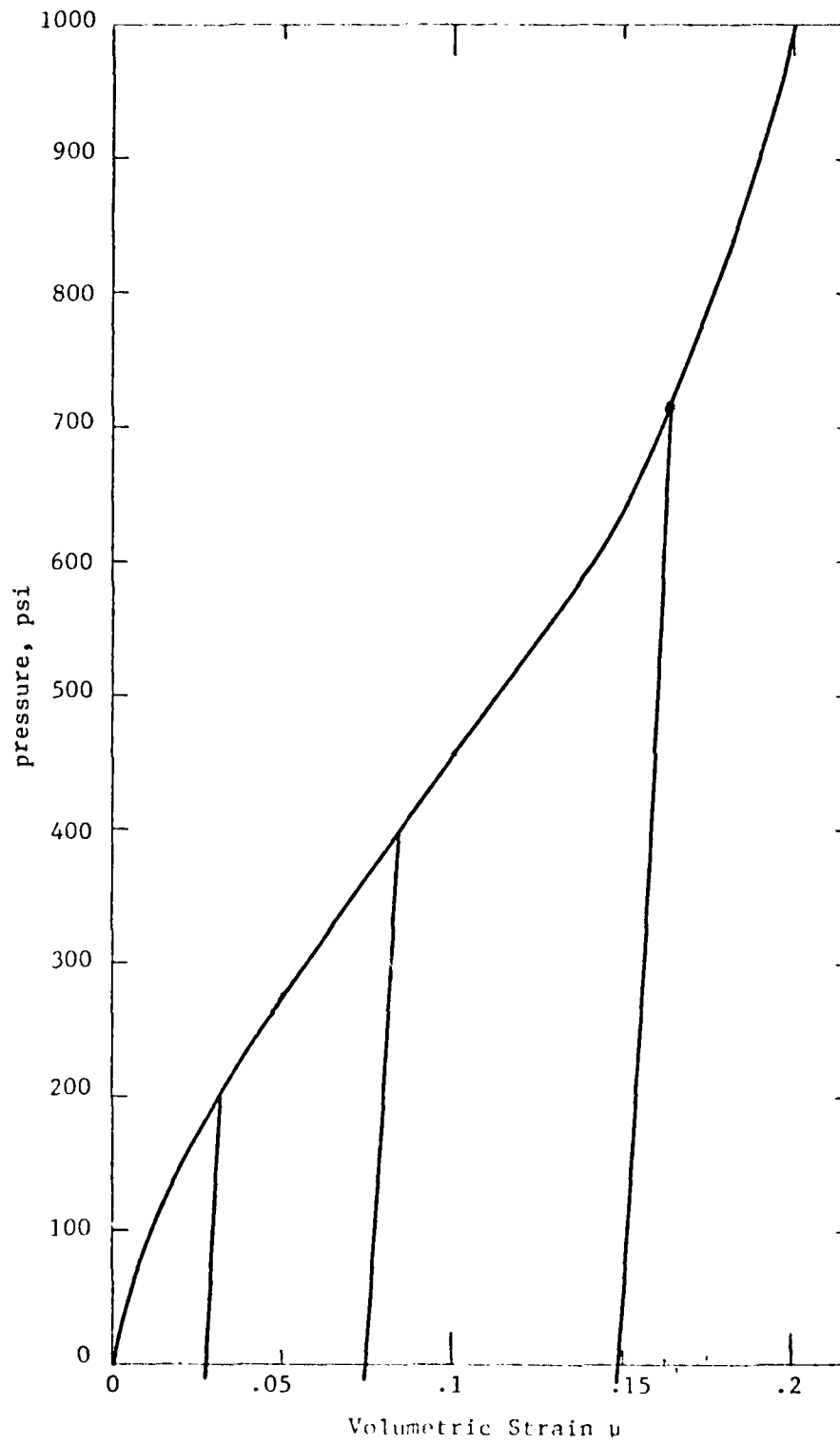Figure 3.3-4. Uniaxial Strain Stress Paths and Failure Surface in High-Pressure Region for Layer 1. (P to 14 ksi)

33

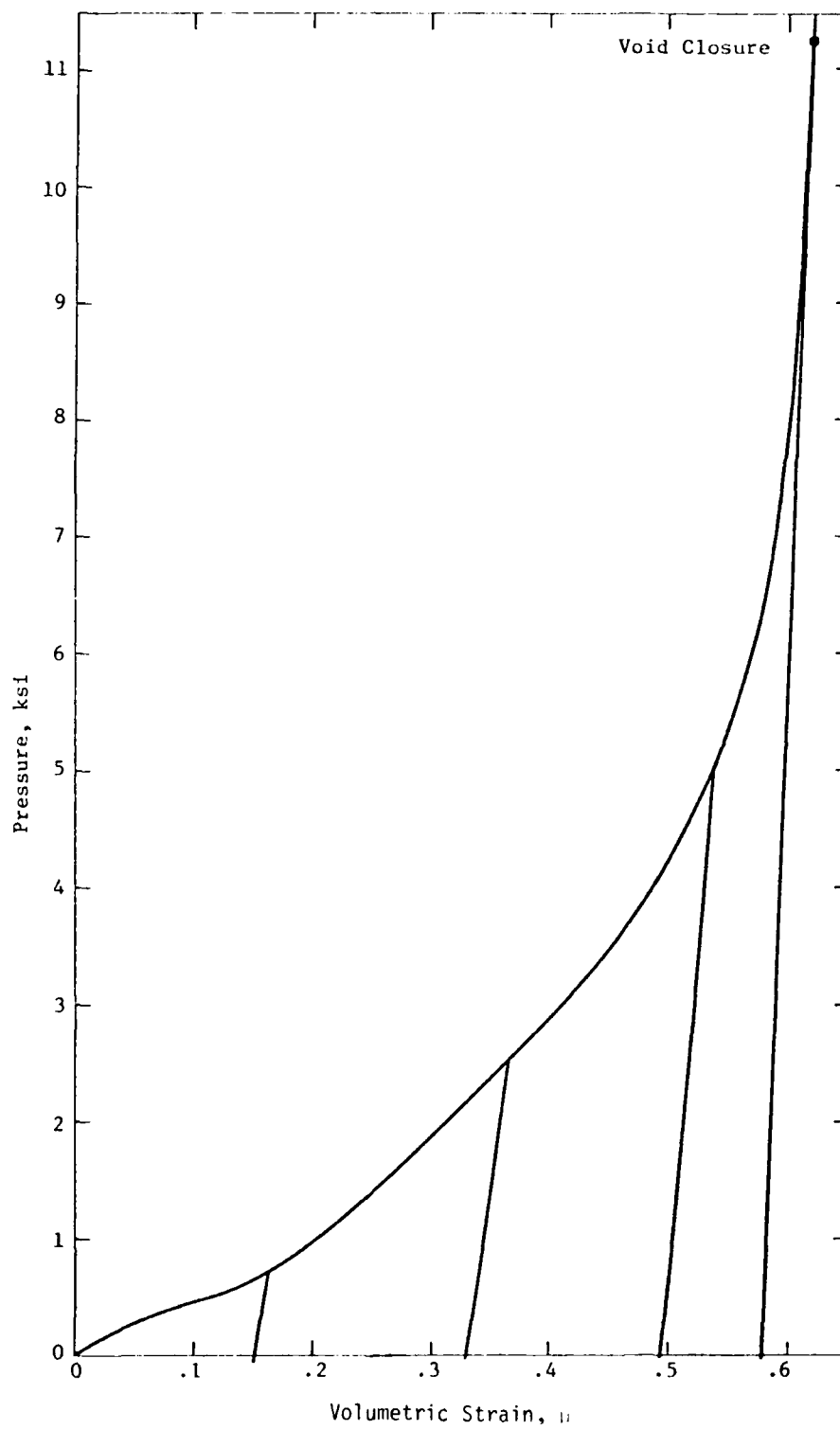Figure 3.3-5. Hydrostatic Load-Unload Paths for Layer 1.
(P to 1000 psi)

Figure 3.3-6. Hydrostatic Load-Unload Paths for Layer 1.
(P to 11.5 ksi)

35

4. CALCULATION RESULTS

4.1 Deceleration

The computated decelerations for the cases having impact
velocities of 500 ft/s are summarized in Figures 4.1-1 and
4.1-2. It was found that the velocity-time plots of Figure
4.1-1 were the most accurate means of determining the deceleration
as a function of time. The computed deceleration curves are
qualitatively similar for all four cases shown. After initial
impact, the deceleration increases smoothly as more and more of
the nose is buried. At the impact velocity of 500 ft/s, the
projectile penetrates about six inches per ms, so that it
requires about three milliseconds to bury the nose. It may be
seen from the Figure that a limiting value of deceleration is
reached by about three ms, after which the velocity-time
plot is essentially a straight line.

It might seem surprising that the limiting deceleration
is attained so rapidly. The reason is that the forces which
produce the deceleration are concentrated near the nose tip. By
the time the ogival portion has been buried, a "steady-state"
flow field has been established in the soil near the nose tip.
At that point in time, the forces near the tip become "constant".
The quotation marks have been used because the flow is "steady-
state" and the forces are "constant" on the time scale of a few
milliseconds which we are examining here. The flow field and
velocity field are velocity dependent, and will change as the
projectile's velocity decreases. In the cases we consider here,
the velocity changes on the order of a percent per millisecond,
and the deceleration and forces experience changes at a percentage
rate of the same order after "steady state" is attained.
This assertion is supported by the linearity of the velocity-time
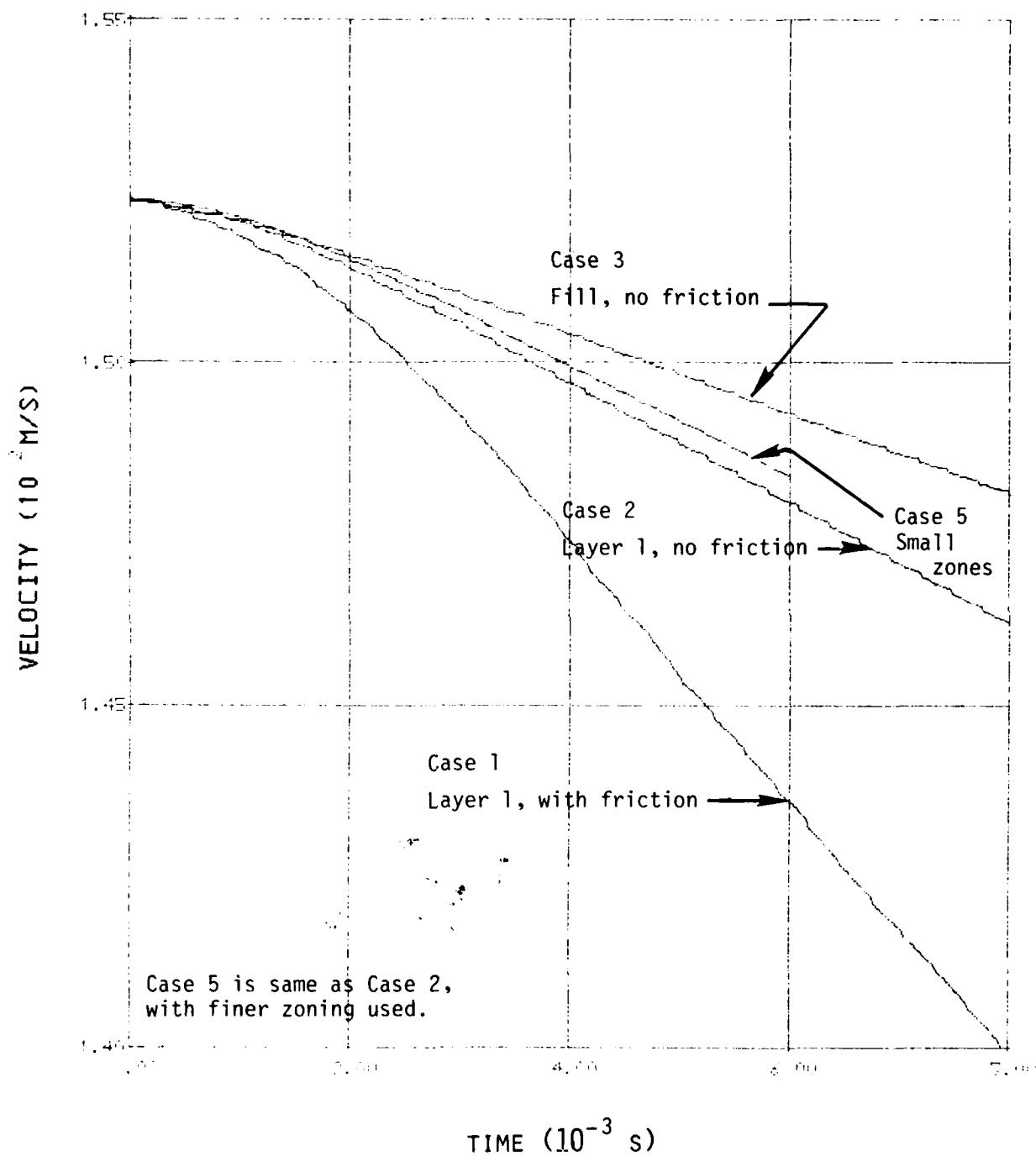plots after three milliseconds.

Figure 4.1-1. Velocity-time plots for EPW penetrations.
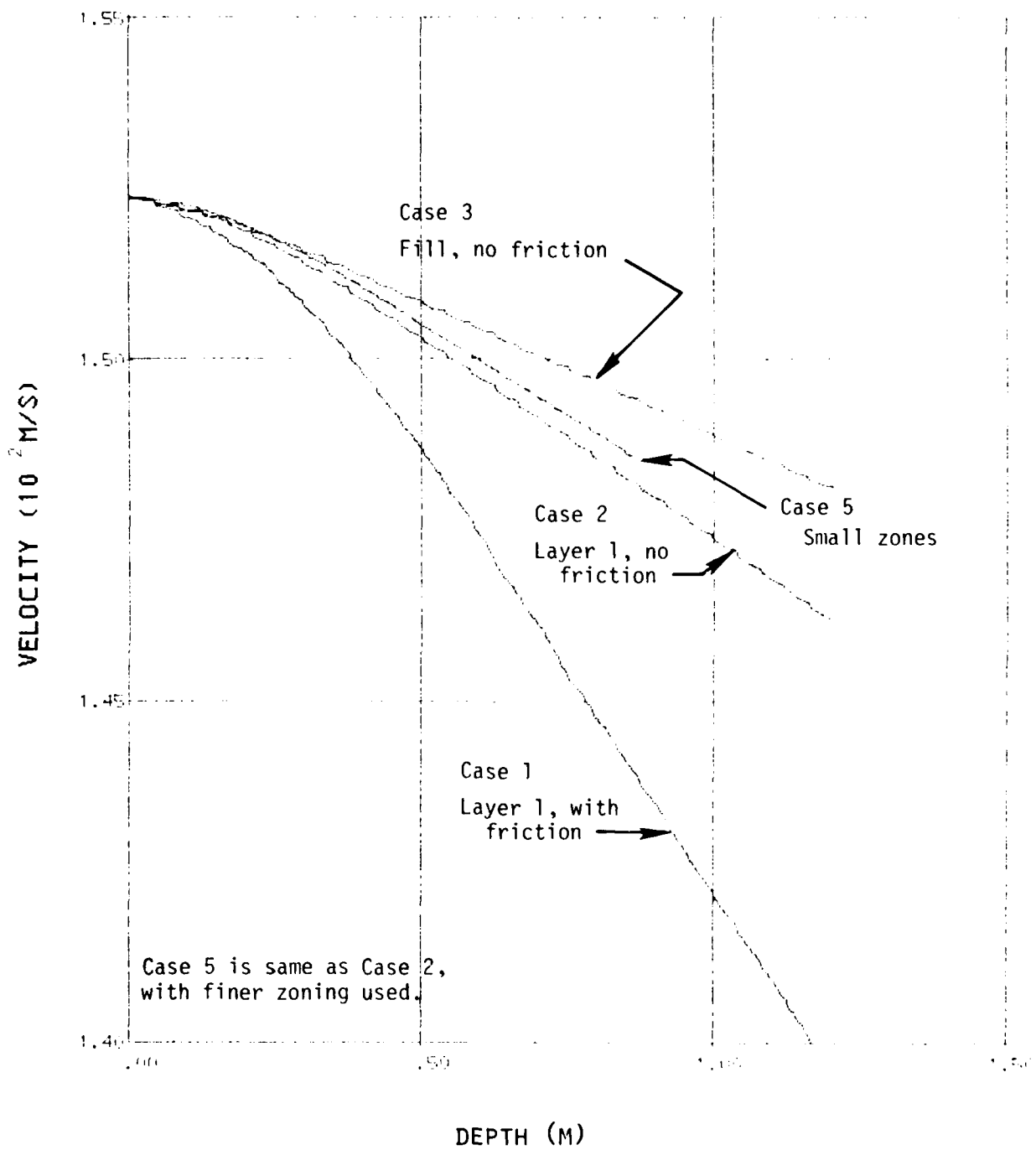Impact velocity is 500 ft/s = 152.4 m/s.

37

Figure 4.1-2. Velocity-depth cross plots for EPW penetrations.
Impact velocity is 500 ft/s = 152.4 m/s.

The velocity-time curves are not perfectly smooth, but exhibit peaks and valleys. In the linear region, the best estimate of deceleration is given by passing one straight line through the peaks, and another through the valleys. The two lines are essentially parallel, and lead to decelerations which typically differ by only 0.2%. The lines bound the velocity-time curves, and their average slope provides a good measure of the deceleration in the "steady-state" region. The decelerations so deduced are summarized in the following table.

	Deceleration (g's)		
Case	Curve through Velocity Peaks	Curve through Velocity Valleys	Average
1	191.04	191.44	191.24
2	89.79	89.81	89.80
3	59.46	59.52	59.49
*4			1982.00
5	81.95	81.84	81.90

*The curves for Case 4 are more irregular, and only the average value is given. (See Figure 4.3-3a.)

The peaks and valleys arise because of the finite size of the cells used in the computing grid. When the tip of the projectile first encounters a cell, the cell corner is given a sudden velocity increment in one computing cycle. The velocity increment is "felt" by the entire cell mass. The sudden change in cell momentum arising thereby produces a corresponding change in projectile momentum, and produces a valley. It would be more

39

accurate to impart the sudden velocity increment only to the mass
of the cell spanned by the wave arising from the collision, as
would occur in the case of infinitely fine zoning. It is
recognized that this phenomenon tends to overestimate the computed
deceleration.

The amount of the overestimate can be determined by a
zoning study in which the zone sizes are successively reduced in
a series of calculations. One would expect to find a limiting
zone size beyond which the computed deceleration did not vary
significantly. A step in this direction was taken in Cases 2
and 5, which differ only with respect to the zone size used.
Cases 2 and 5 utilized initially square zones having sides of
4.1275 and 3 cm, respectively. The masses of the cells initially
on axis were 343.5 and 131.8 gm. The computed decelerations
were 89.8 and 81.9 g's.

Although the decrease in computed decleration appears to
be modest, the finer zoning was found to produce a striking change
in the distribution of tractions* on the projectile, as will be
discussed more fully in Section 4.2. In view of this, one cannot
be certain that the 10% change in computed deceleration indicates
that the zoning is close to that required to compute the correct
deceleration. It is important to conduct computations with much
finer zoning to determine both the correctly-computed deceleration
and tractions* on the vehicle.

---

*Surface traction is a vector whose magnitude is the force per unit
area. The traction provides the proper boundary condition for the
stress field in the vehicle, which is $T^i = \sigma^{ij} n_j$, where T^i is the
traction, σ^{ij} is the stress in the vehicle evaluated at the surface,
and n_j is the unit outward vector normal to the surface.

4.2 Stress on the Projectile

As discussed in the previous section, the coarse computing cell size leads to irregularities in the deceleration. The same phenomenon leads to irregularities in the stress and velocity fields in the surrounding soil. As a result, it can be somewhat misleading to examine a snapshot of the stress and velocity fields at a particular time. It is much more accurate to conduct suitable time averages to determine the true values of these variables. Such time averages were conducted to find the stress on the projectile.

The averaging process is made more complex by the fact that the Lagrangian computing cells move along the projectile's surface. To accommodate this, the surface was divided into segments one-half inch (1.27 cm) in height, and the surface forces on each segment were monitored in time. The stations of the segment boundaries are tabulated in Table 4.2-2. For a given segment, the averaging process was conducted as follows. During each computing cycle, the Lagrangian nodes in contact with the segment were multiplied by Δt, and the sums $\sum_n F_x^n \Delta t^n$, $\sum_n F_y^n \Delta t^n$ were built up over a given time interval. The average is taken to be the quotient of these sums and the time interval. The time-averaged values in each segment after the steady-state was reached were determined, and are plotted in Figures 4.2-1 through 4.2-10.

The plots present the time-averaged force on each segment, the odd-numbered plots giving the axial components and the even-numbered plots giving the radial component. The axial forces are presented because they represent the relative contribution of each segment to the projectile's deceleration. The forces on the conical nose tip are not plotted in the Figures because they are so large that their plotting would produce poor scaling. Instead, they are called out in the figure captions. The area of the conical nose tip is 7.1659 cm^2.

41

To obtain the traction (force per unit area) on a segment, the force must be divided by the segment's area. The areas are tabulated in Table 4.2-2, and the tractions are presented in Figures 4.2-11 through 4.2-20. The tractions are the physical entities which provide the boundary condition for the stress field in the projectile.

As the soil flows around the shoulder of the conical tip, it separates from the projectile because of its inertia. This creates a free surface on the soil on which there is no traction, and the stress within the soil causes the surface to accelerate back to the projectile. This phenomenon leads to low average traction on the projectile's surface just above the conical tip, followed by a spike where the soil reattaches to the vehicle. The region of separation may be seen in the configuration plots of Section 4.3.

Because the cells are given too large a momentum by the conical tip (as discussed above), the region of separation is overestimated. This may be verified by comparing the force profiles for the coarse and fine zone cases shown in Figures 4.2-3 and 4.2-9. The coarse zoning leads to a wider region of separation, and a higher spike in force (and therefore traction) when reattachment occurs.

The forces and tractions which appear on the conical nose tip are inordinately large. The reason is that the zone size of all the cases is too large to resolve the true stress on the conical tip. When the tip first encounters the upper left hand corner of a zone on axis, (See the zone configuration plots in Figures 4.3-1 through 4.3-5) that corner is imparted in one or two time cycles the velocity required for it to travel along the tip. For an impact velocity of 500 ft/s, the increments in x and y velocity are on the order of 600 cm/s. For the purposes of computing momentum, each vertex in the computing grid has associated with it a quarter of the total cell mass of each adjoining cell, so that the momentum change in the cell is 6000(M/2) gm cm/s, since there are two adjoining cells for each

vertex on axis. The force on the nose tip was computed as the
time rate of change of momentum it created in the computing grid.
When the dimensions of a quarter-cell exceed the width of the
conical nose tip, as they do in all cases treated here, the tip
accelerates too much mass and the stress and force on the nose
tip is grossly overestimated, because the computing algorithms
overestimate the momentum increase for the reasons discussed
above.

The major point of this discussion is that to compute the
stress distribution on a blunted vehicle accurately, zone
sizes of 2, or perhaps even 1 cm should be used. This consider-
ation is particularly important because the stress distribution is
required to compute the structural response of the EPW.

The above discussion can be made more quantitative by
examining the forces and tractions computed in the various cases
of this study. These are summarized in Table 4.2-1.

TABLE 4.2-1

			SUMMARY OF FORCES AND TRACTIONS ON CONICAL NOSE TIP		
Case	Radial Force Dynes	Axial Force Dynes	% Contribution of nose tip to Deceleration	Axial Traction kbar	Radial Traction kbar
1	-7.0×10^9	9.7×10^9	28.7	1.35	-.977
2	-6.4×10^9	6.4×10^9	40.1	.888	-.888
3	-6.1×10^9	6.1×10^9	58.1	.852	-.852
4	-3.0×10^{11}	3.0×10^{11}	83.3	42.0	-42.0
5	-4.9×10^9	4.9×10^9	33.3	.678	-.678

The table shows that for all the frictionless cases
(2 through 5), the radial and axial force are the same, because the
frictionless 45^0 tip imparts equal x and y velocity increments
to the soil it encounters. Cases 2 and 5 are different only in
that Case 5 had 3 cm zones and Case 2 had 4.1275 cm zones.
The more finely zoned case has an axial force of 4.9×10^9
dynes, compared with the 6.4×10^9 dynes for coarser zoning.
The reduction in force is 23%, and is produced by a zone size
reduction of 27%. The axial forces further back on the ogive are
given in Figures 4.2-3 and 4.2-9, and it may be seen that they
are quite similar at distances greater than 12 cm above the tip.

Case 4 shows that this phenomenon will have a very important
influence on the computed deceleration at high velocity, since
the force on the conical tip is responsible for 83.3% of the
computed deceleration. It seems likely that the computed
deceleration for this case is seriously in error, and that smaller
zones should be used. This question could be resolved by using
successively finer zones until convergence to a common deceleration
was obtained.

TABLE 4.2-2

AREA OF PROJECTILE SEGMENTS USED TO MONITOR STRESS			
Lower Station of Segment cm	Segment Area cm^2	Lower Station of Segment cm	Segment Area cm^2
1.27	12.2493	24.13	53.5337
2.54	15.4303	25.40	54.9265
3.81	18.4963	26.67	56.2326
5.08	21.4496	27.94	57.4527
6.35	24.2927	29.21	58.5878
7.62	27.0275	30.48	59.6386
8.89	29.6562	31.75	60.6057
10.16	32.1806	33.02	61.4898
11.43	34.6027	34.29	62.2913
12.70	36.9240	35.56	63.0111
13.97	39.1464	36.83	63.6491
15.24	41.2715	38.10	64.2061
16.51	43.3005	39.37	64.6823
17.78	45.2350	40.64	65.07801
19.05	47.0764	41.91	65.3935
20.32	48.8258	43.18	65.6290
21.59	50.4844	44.45	65.7847
22.86	52.0534		

EPW PROBLEM 1

Impact speed: 500 ft/s
Soil type: Layer 1
Friction?: Yes
Initial zone size: 4.13 cm
Averaging interval: 3 - 8 ms

AXIAL FORCE (10⁹ DYNES)

10 cm.

5 cm.

DISTANCE FROM NOSE (10 CM)
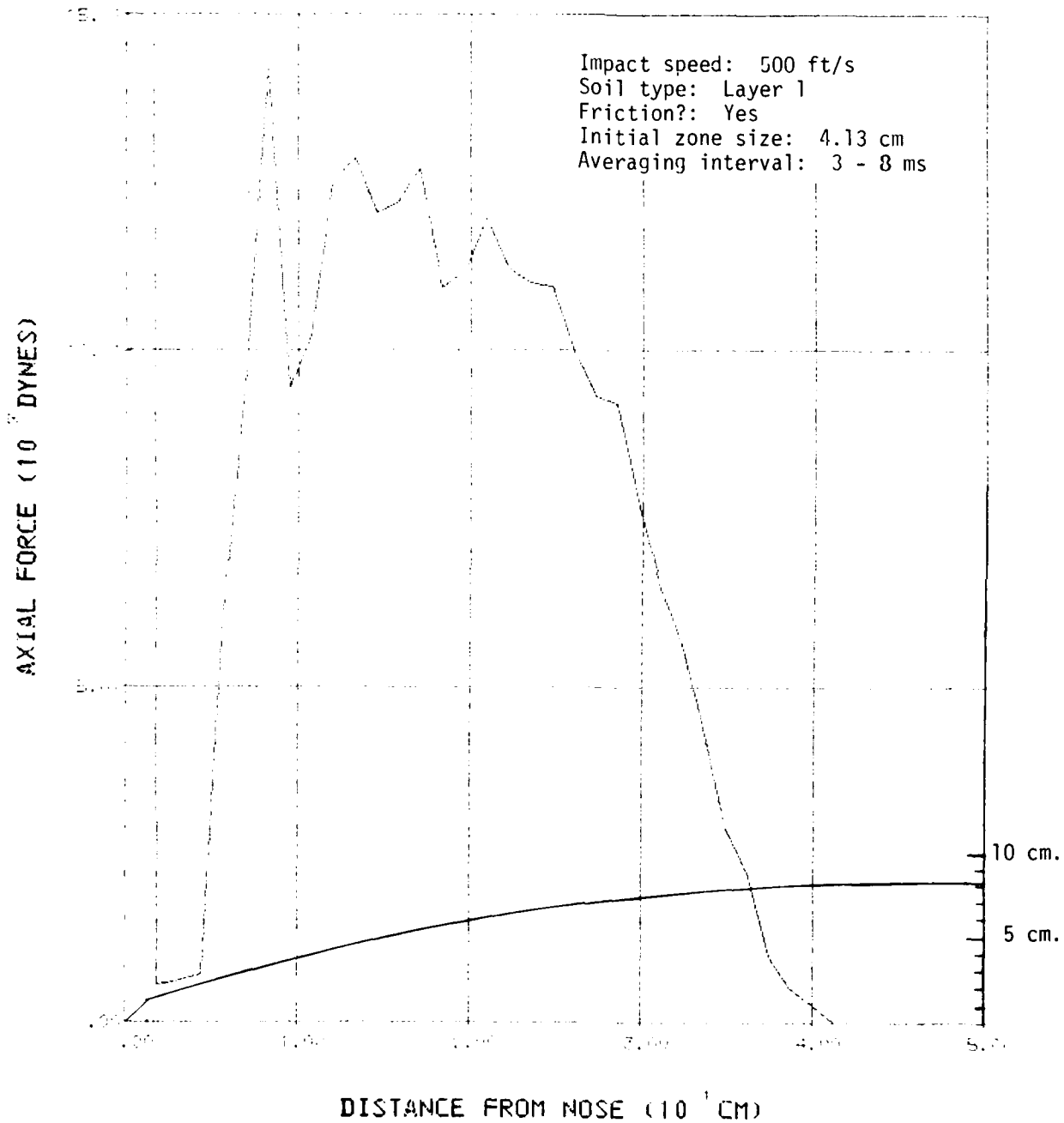
Figure 4.2-1. Time-averaged axial force profile for Case 1.
Force on conical tip = 9.7×10^9 dynes.

EPW PROBLEM 1

Impact Speed: 500 ft/s
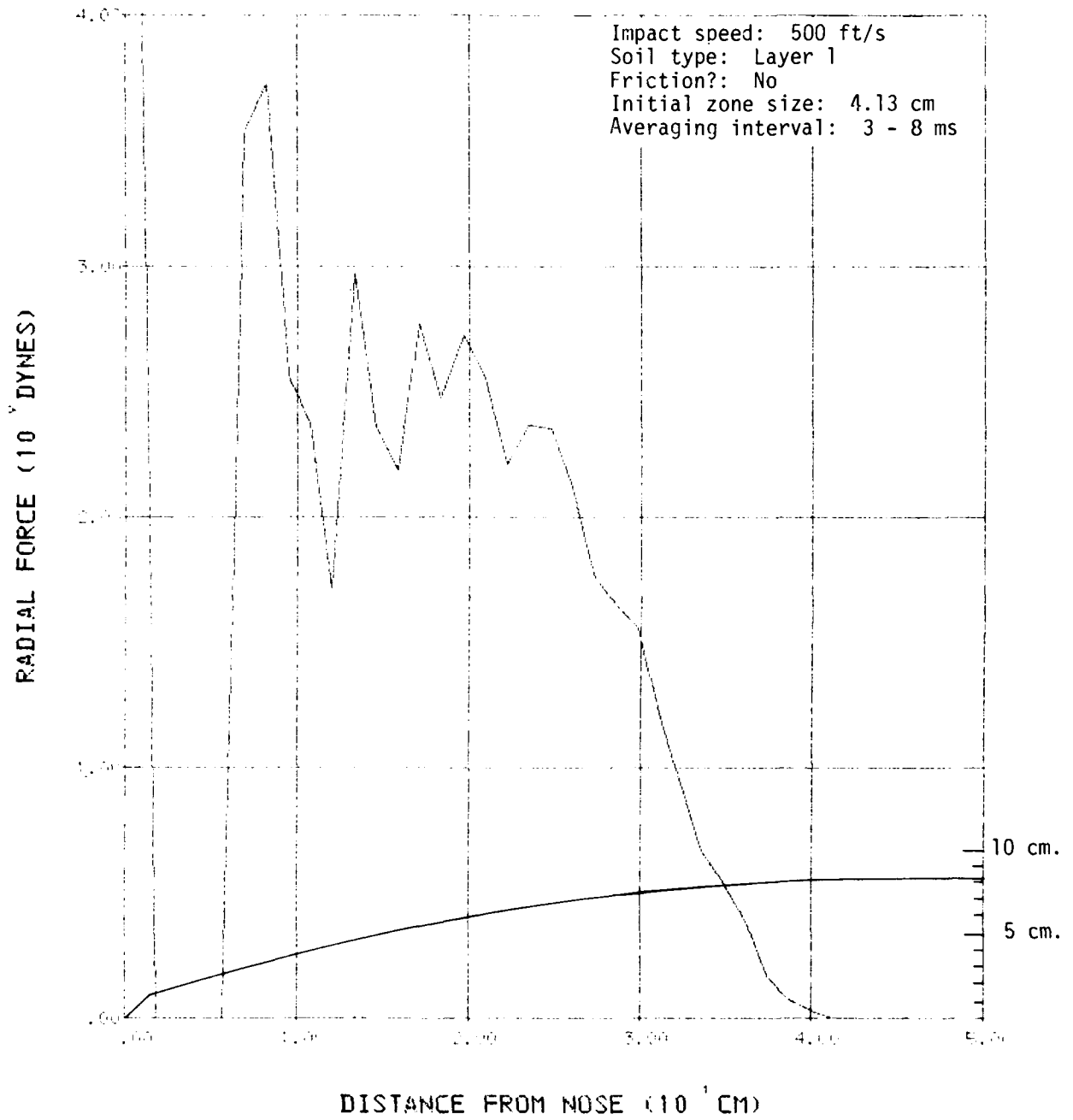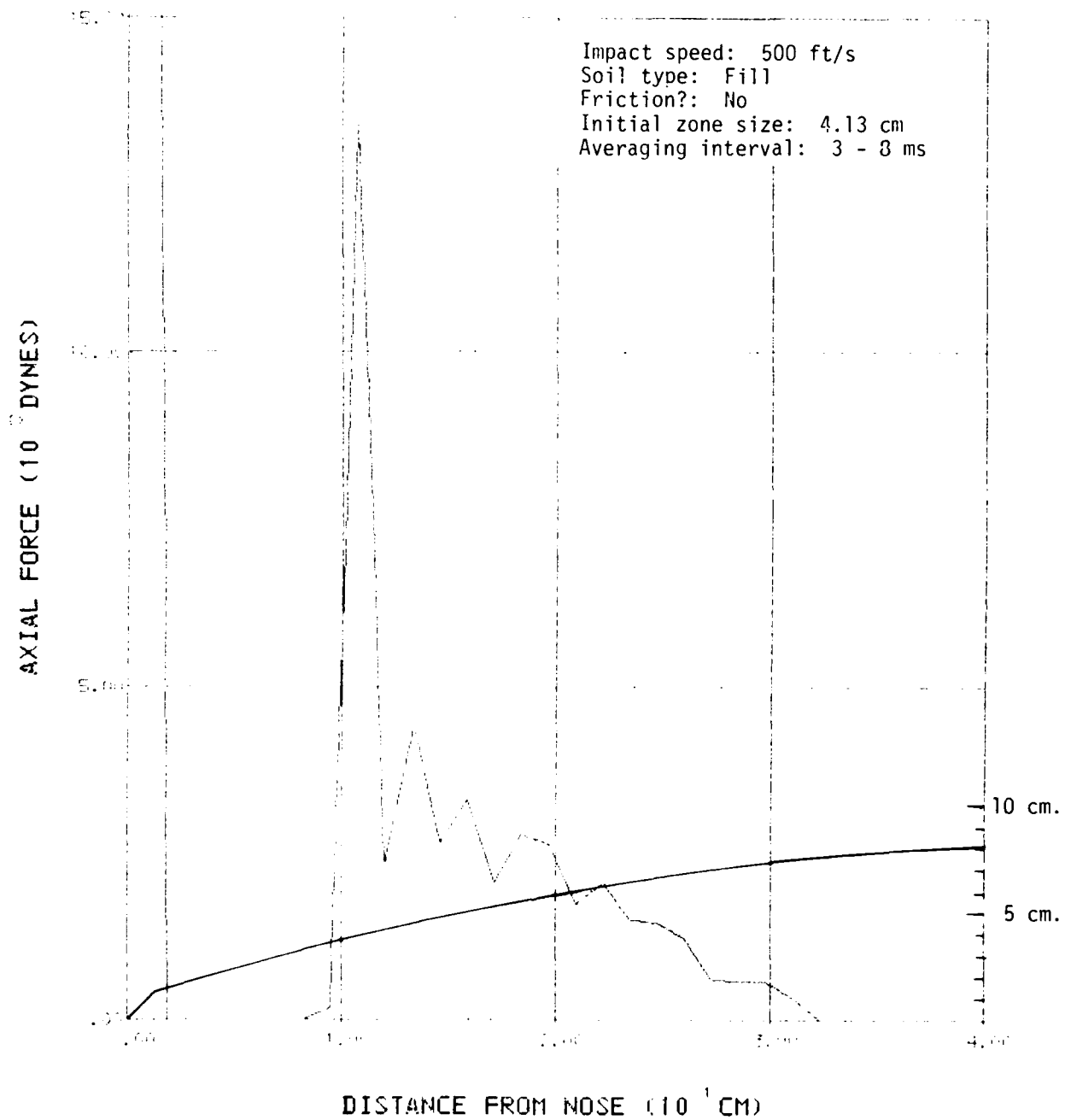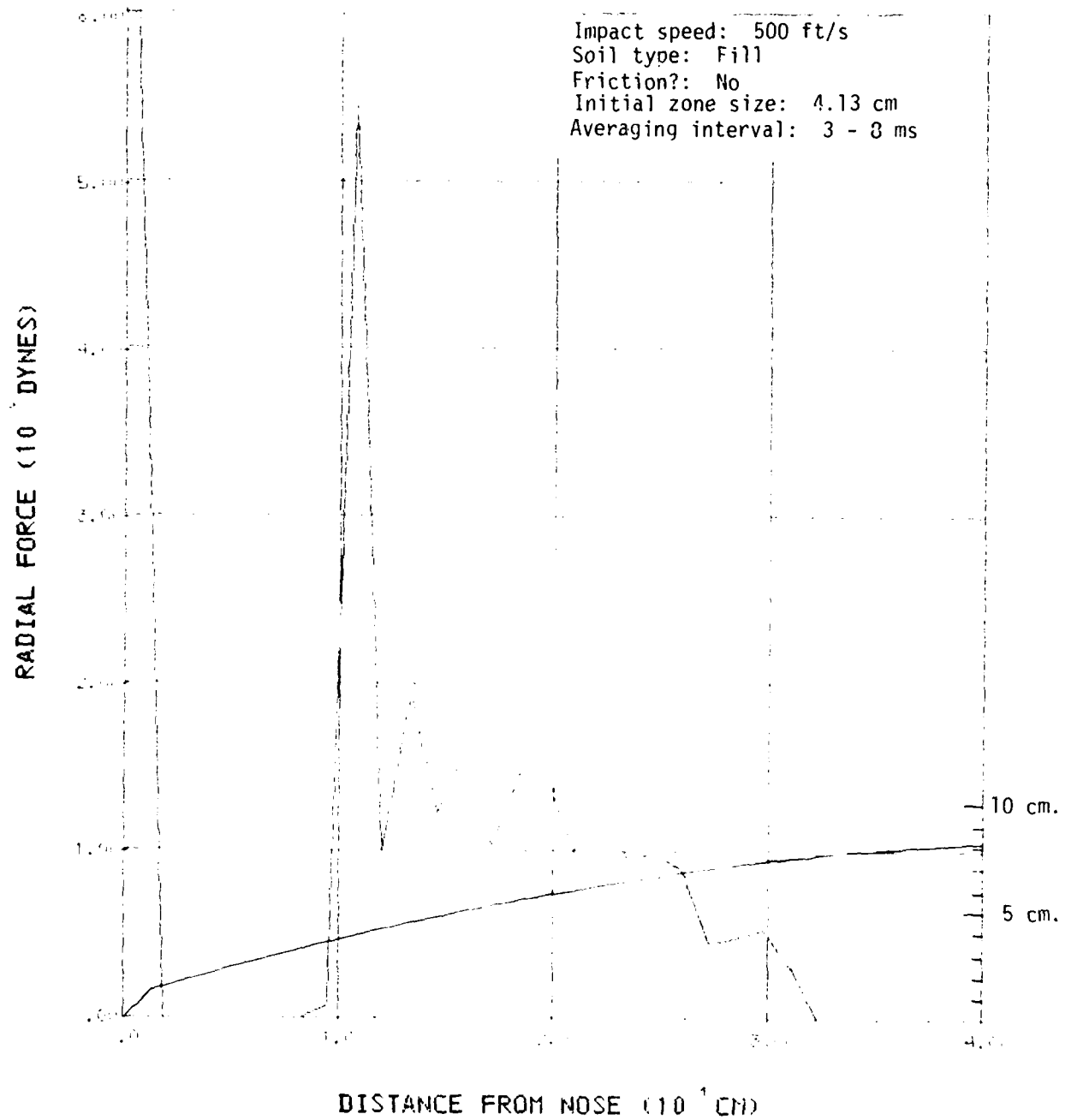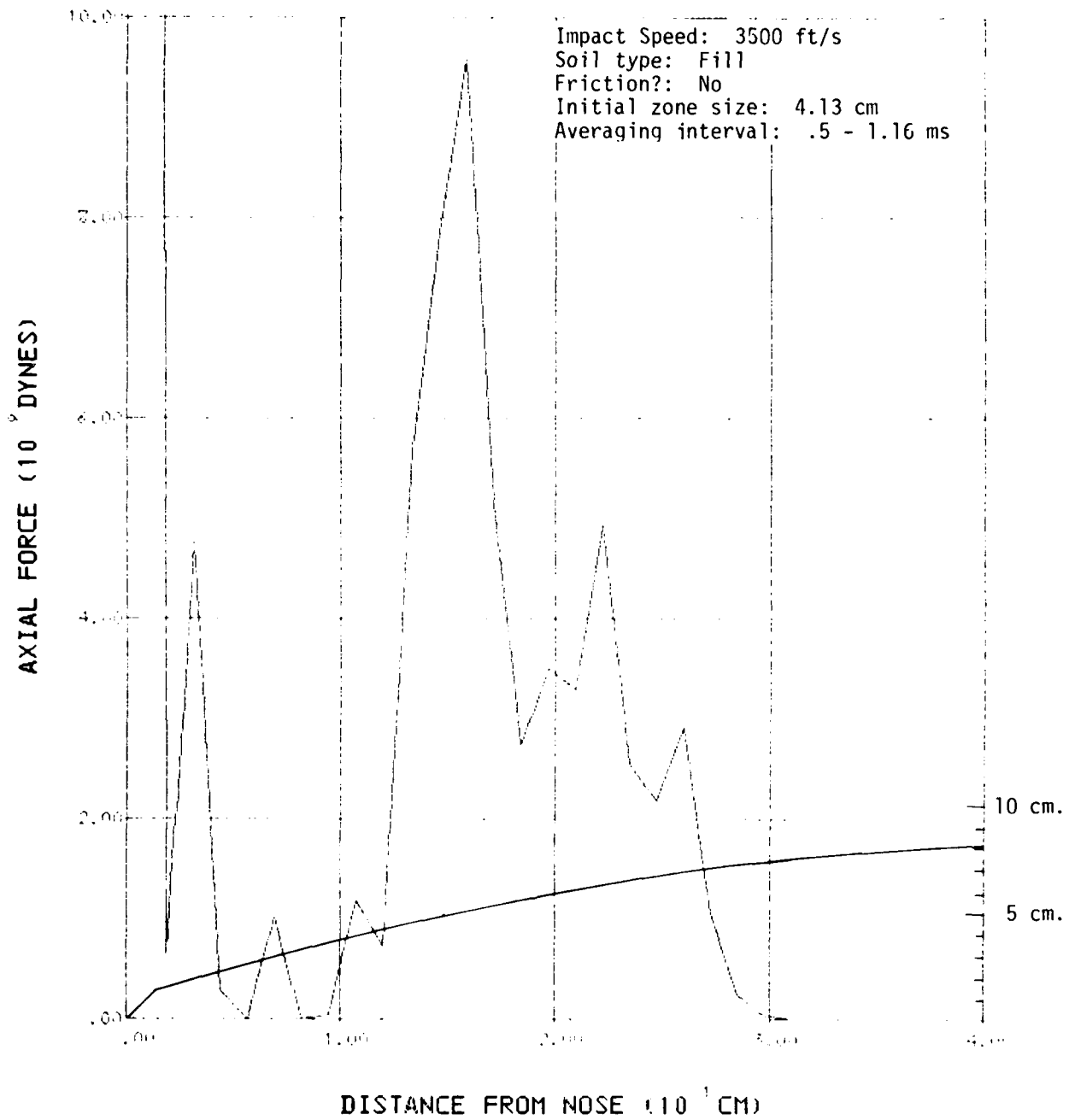Soil type: Layer 1
Friction?: Yes
Initial zone size: 4.13 cm
Averaging interval: 3 - 8 ms

RADIAL FORCE (10⁷ DYNES)

DISTANCE FROM NOSE (10¹ CM)

— 10 cm.

— 5 cm.
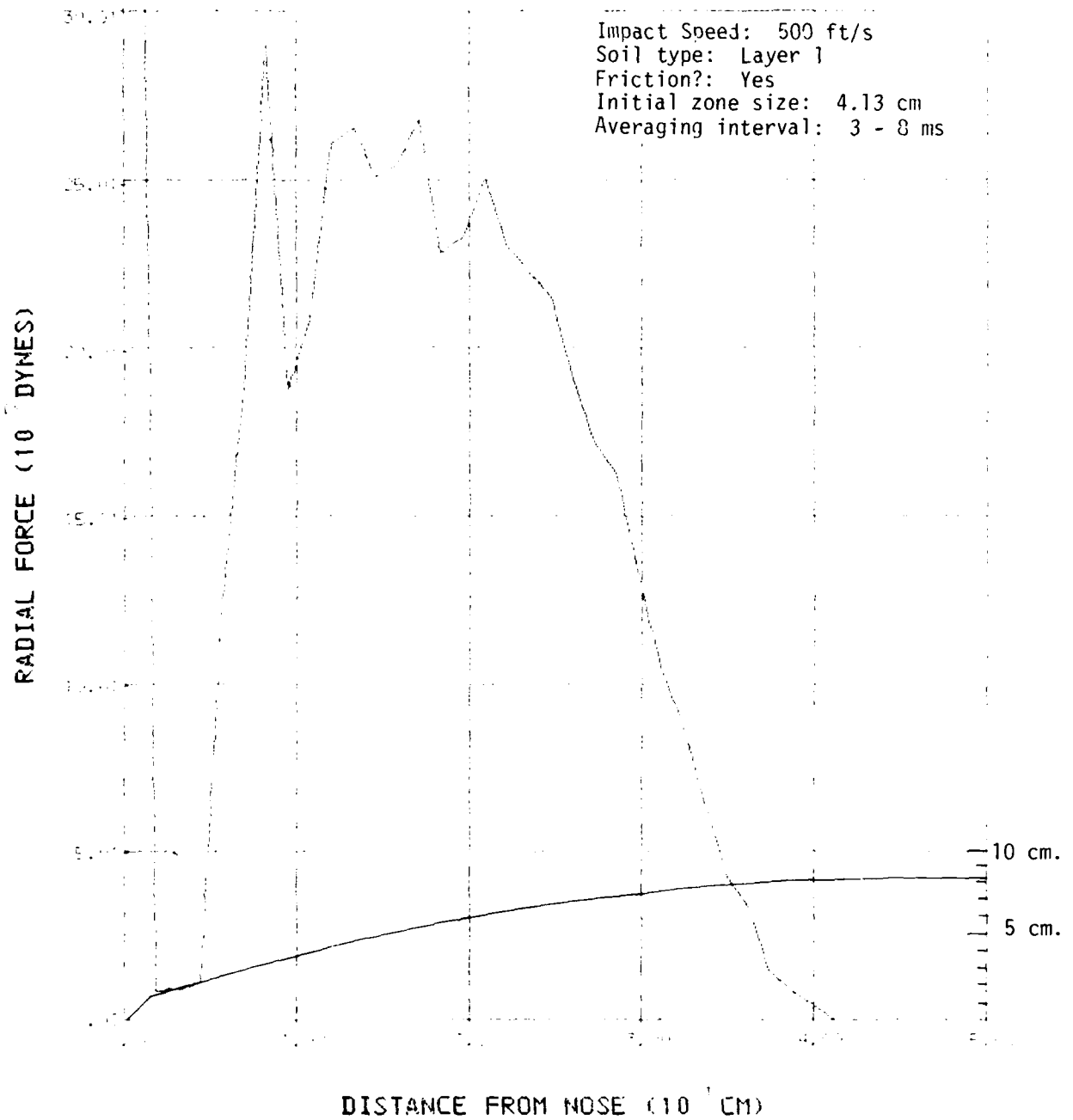
Figure 4.2-2. Time-averaged radial force profile for Case 1.
Force on conical tip = 6.978 x 10⁹ dynes.

EPW PROBLEM 2

Impact speed: 500 ft/s
Soil type: Layer 1
Friction?: No
Initial zone size: 4.13 cm
Averaging interval: 3 - 8 ms

AXIAL FORCE (10⁹ DYNES)

DISTANCE FROM NOSE (10¹ CM)
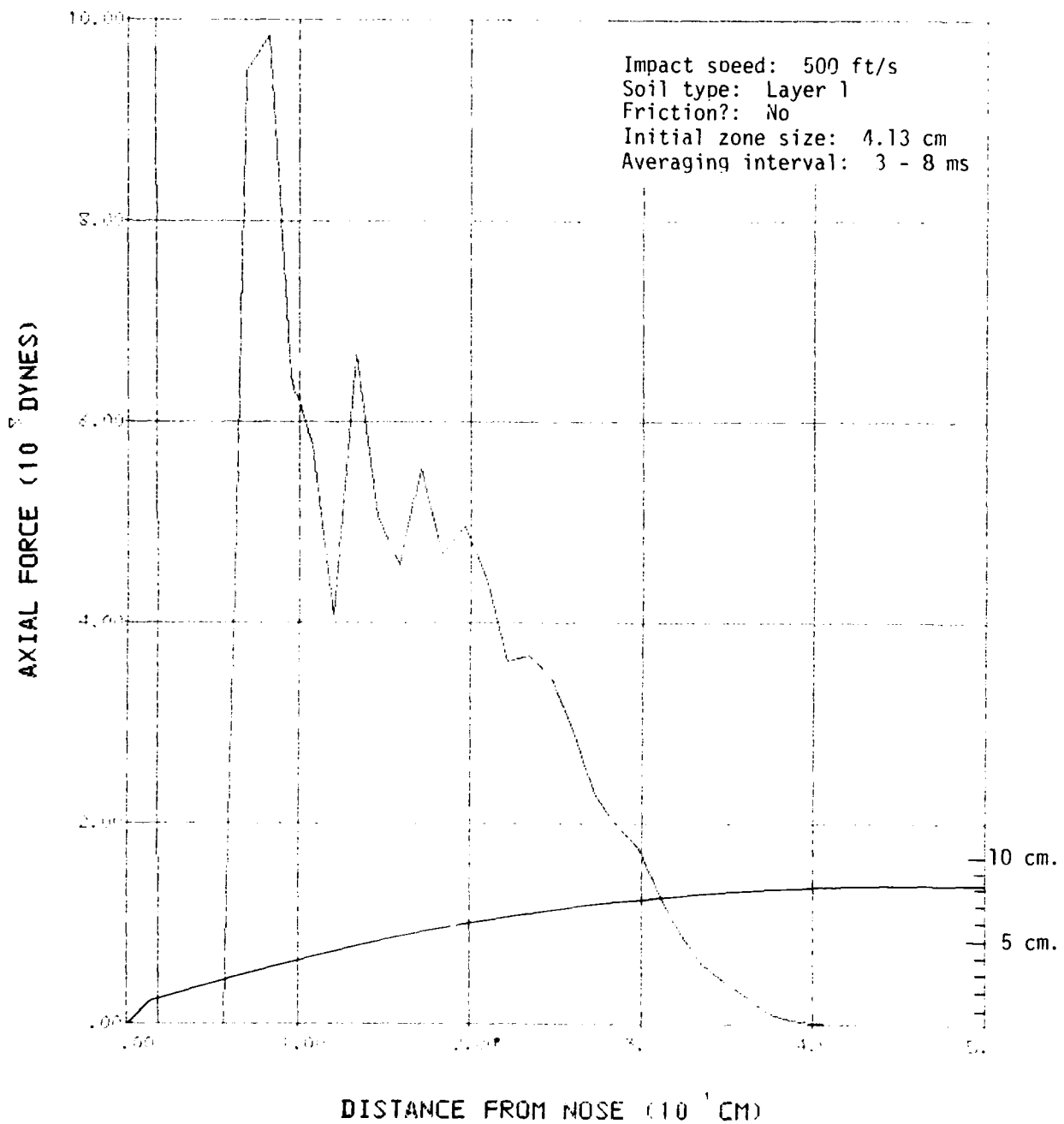
Figure 4.2-3. Time-averaged axial force profile for Case 2.
Force on conical tip = 6.365 x 10⁹ dynes.

EPW PROBLEM 2

Figure 4.2-4. Time-averaged radial force profile for Case 2.
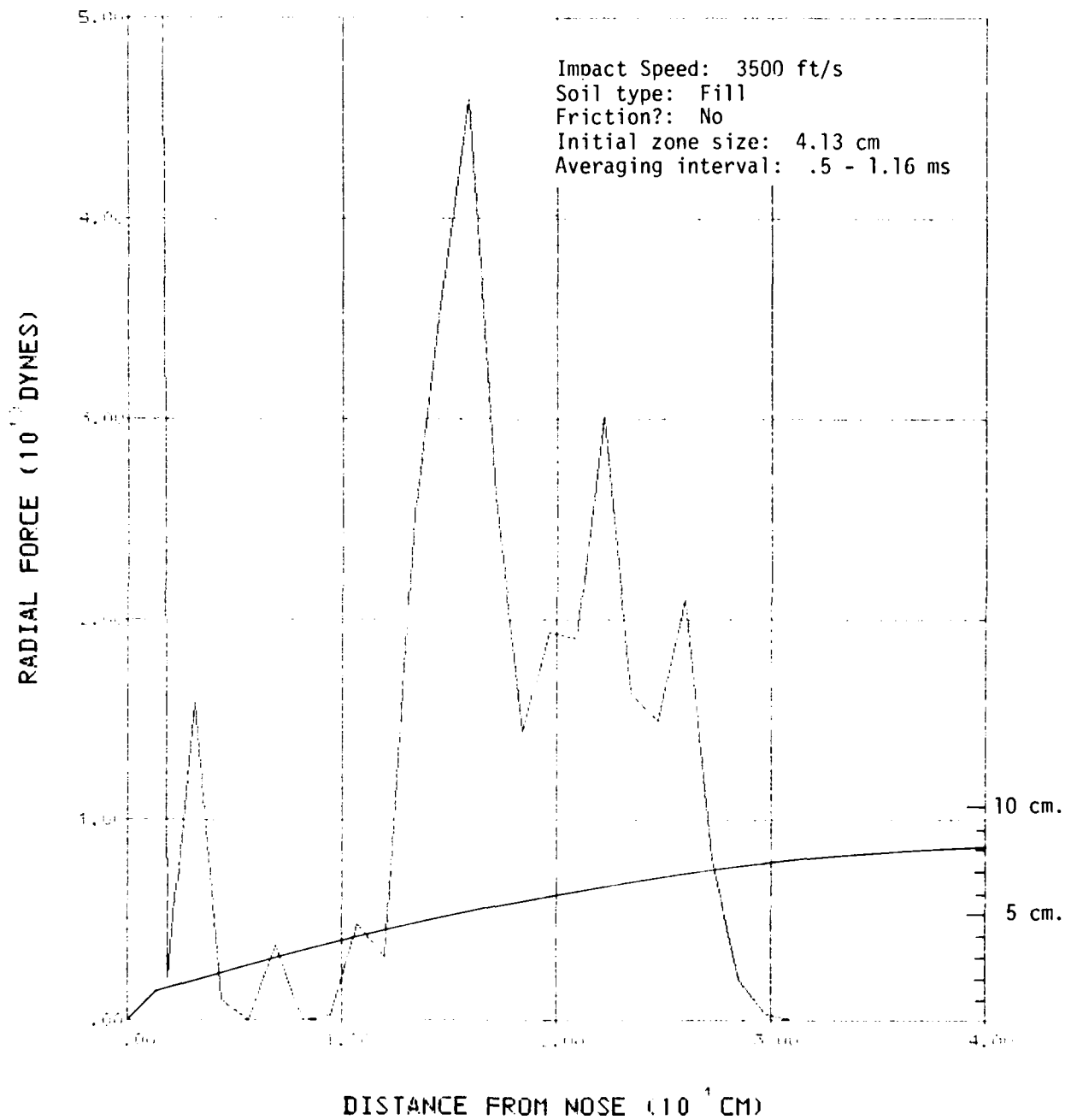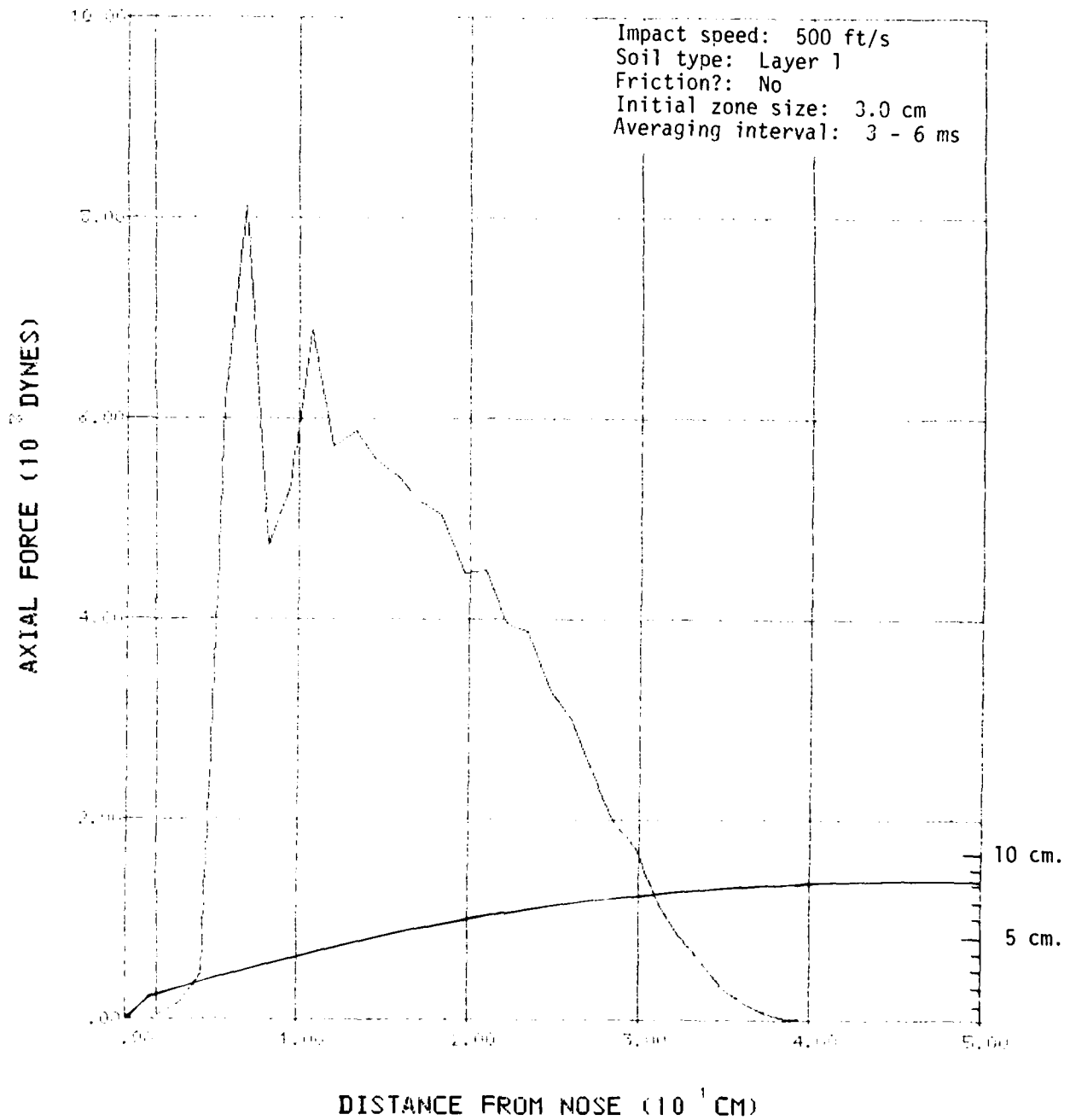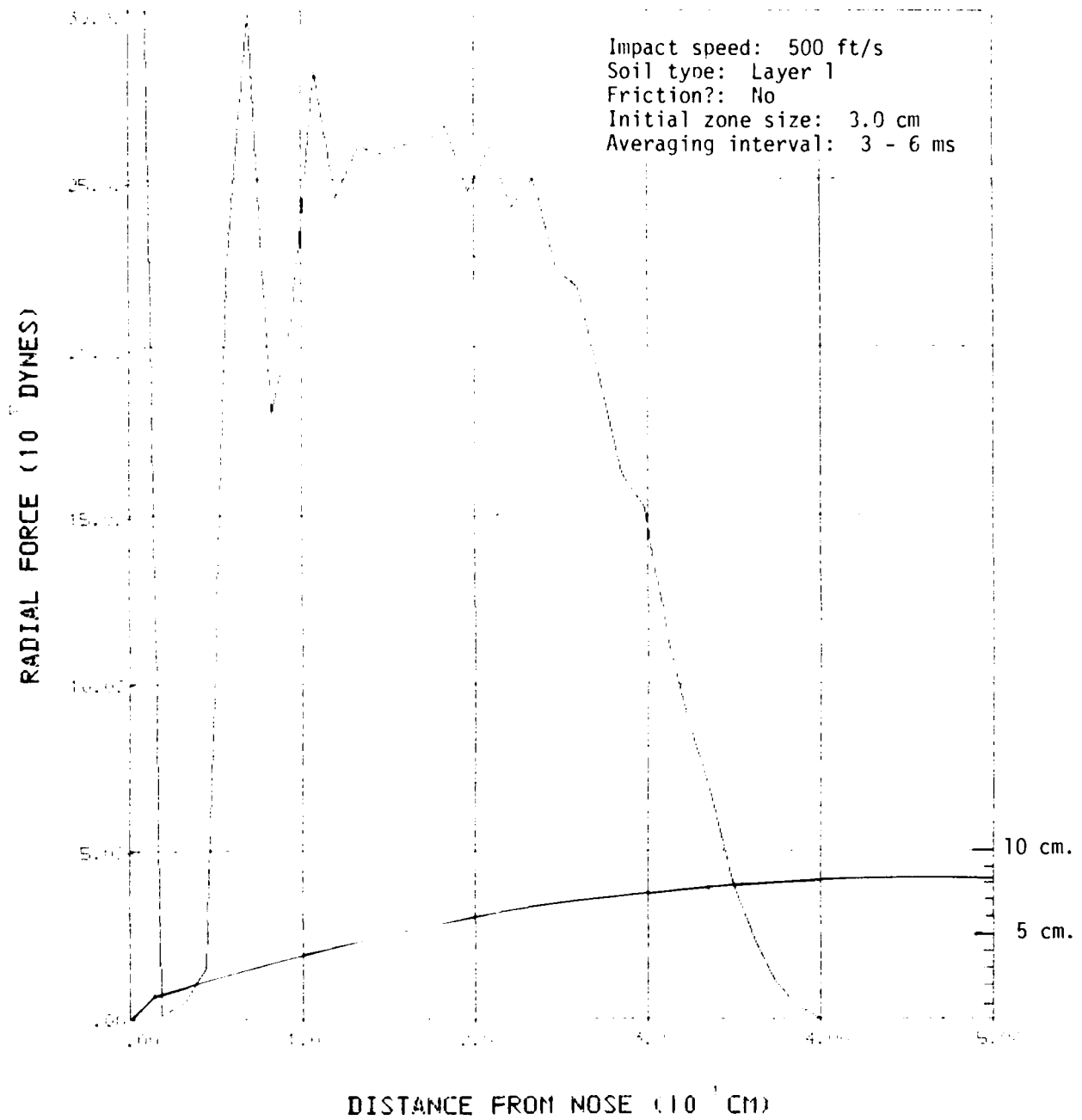Force on conical tip = 6.365 x 10^9 dynes.

EPW PROBLEM 3

Impact speed: 500 ft/s
Soil type: Fill
Friction?: No
Initial zone size: 4.13 cm
Averaging interval: 3 - 8 ms

AXIAL FORCE (10⁹ DYNES)

DISTANCE FROM NOSE (10¹ CM)

Figure 4.2-5. Time-averaged axial force profile for Case 3.
Force on conical tip = 6.103 x 10⁹ dynes.

Figure 4.2-6. Time-averaged radial force profile for Case 3.
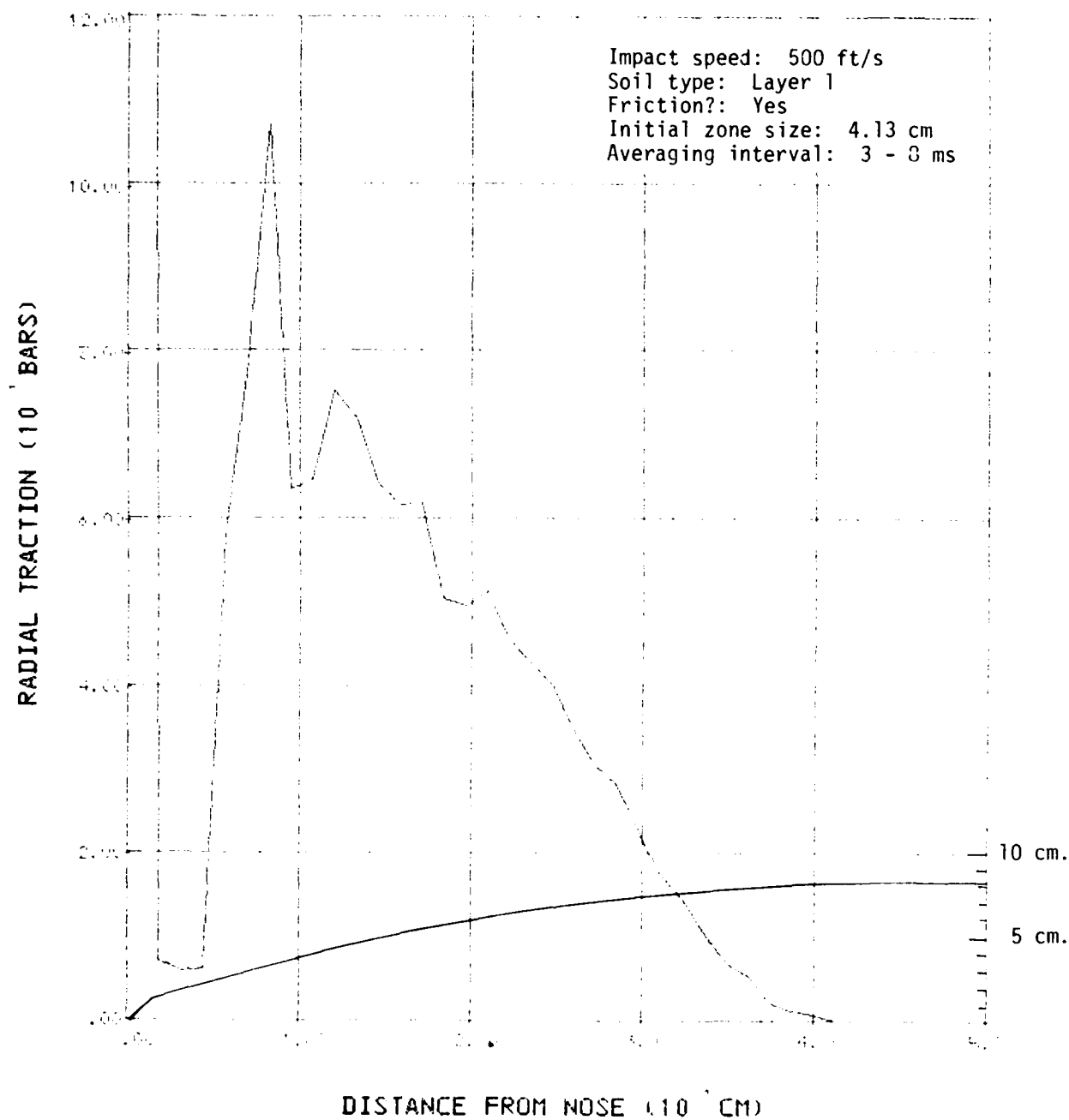Force on conical tip = 6.103×10^9 dynes.

EPW PROBLEM 4

Impact Speed: 3500 ft/s
Soil type: Fill
Friction?: No
Initial zone size: 4.13 cm
Averaging interval: .5 - 1.16 ms

Figure 4.2-7.   Time-averaged axial force profile for Case 4.
Force on conical tip = 3.01 x 10^{11} dynes.

EPW PROBLEM 4

Impact Speed: 3500 ft/s
Soil type: Fill
Friction?: No
Initial zone size: 4.13 cm
Averaging interval: .5 - 1.16 ms

Figure 4.2-8. Time-averaged radial force profile for Case 4.
Force on conical tip = 3.01 x 10^{11} dynes/

EPW PROBLEM 5

Figure 4.2-9. Time-averaged axial force profile for Case 5.
Force on conical tip = 4.856 x 10⁹ dynes/

EPW PROBLEM 5

Impact speed: 500 ft/s
Soil type: Layer 1
Friction?: No
Initial zone size: 3.0 cm
Averaging interval: 3 - 6 ms

RADIAL FORCE (10⁹ DYNES)

DISTANCE FROM NOSE (10¹ CM)

Figure 4.2-10. Time-averaged radial force profile for Case 5.
Force on conical tip = 4.856 x 10⁹ dynes/

EPW PROBLEM 1

Impact speed: 500 ft/s
Soil type: Layer 1
Friction?: Yes
Initial zone size: 4.13 cm
Averaging interval: 3 - 8 ms

Figure 4.2-11. Time-averaged radial traction profile for Case 1.
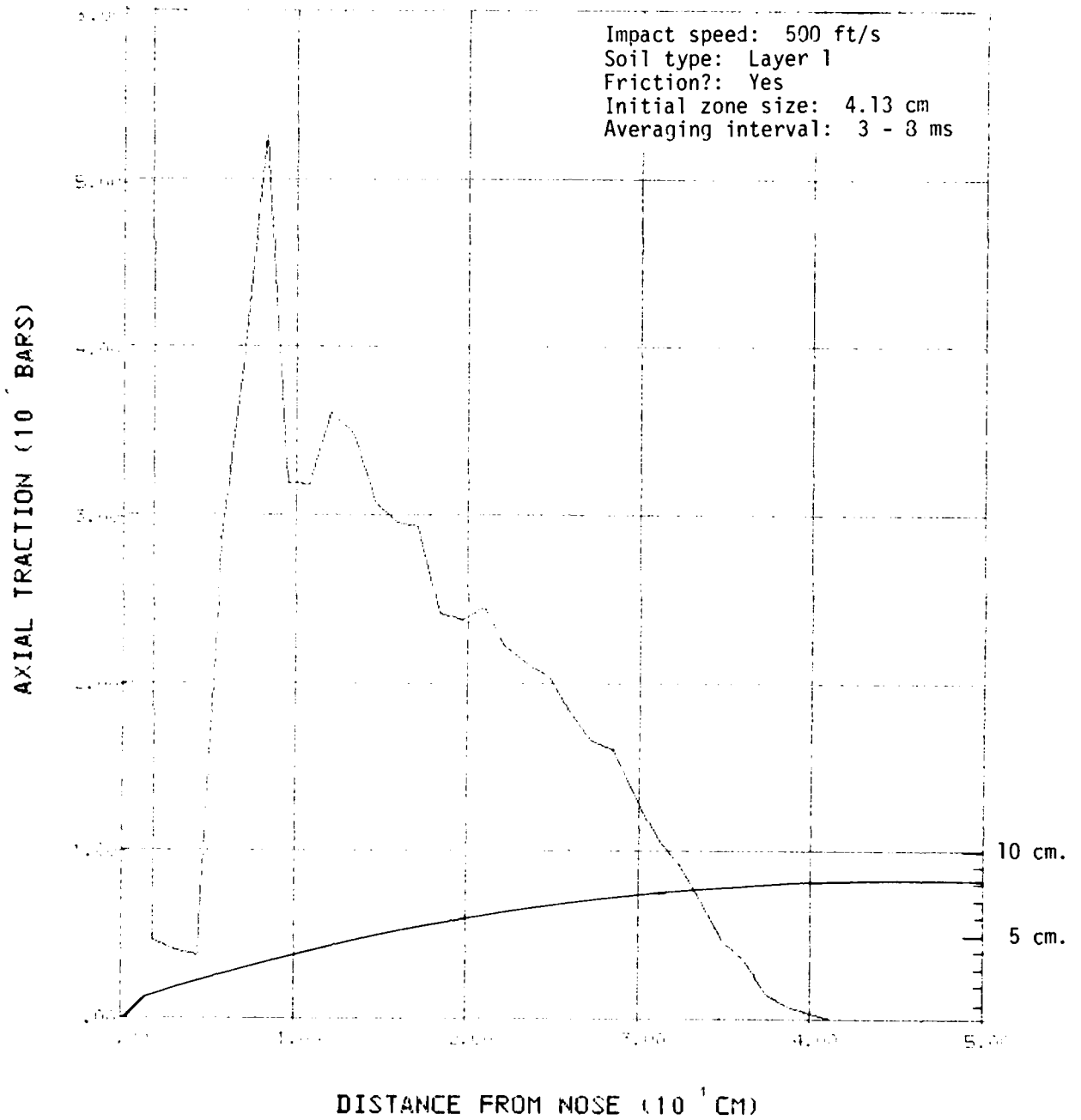
EPW PROBLEM 1

Figure 4.2-12. Time-averaged axial traction profile for Case 1.

EPW PROBLEM 2
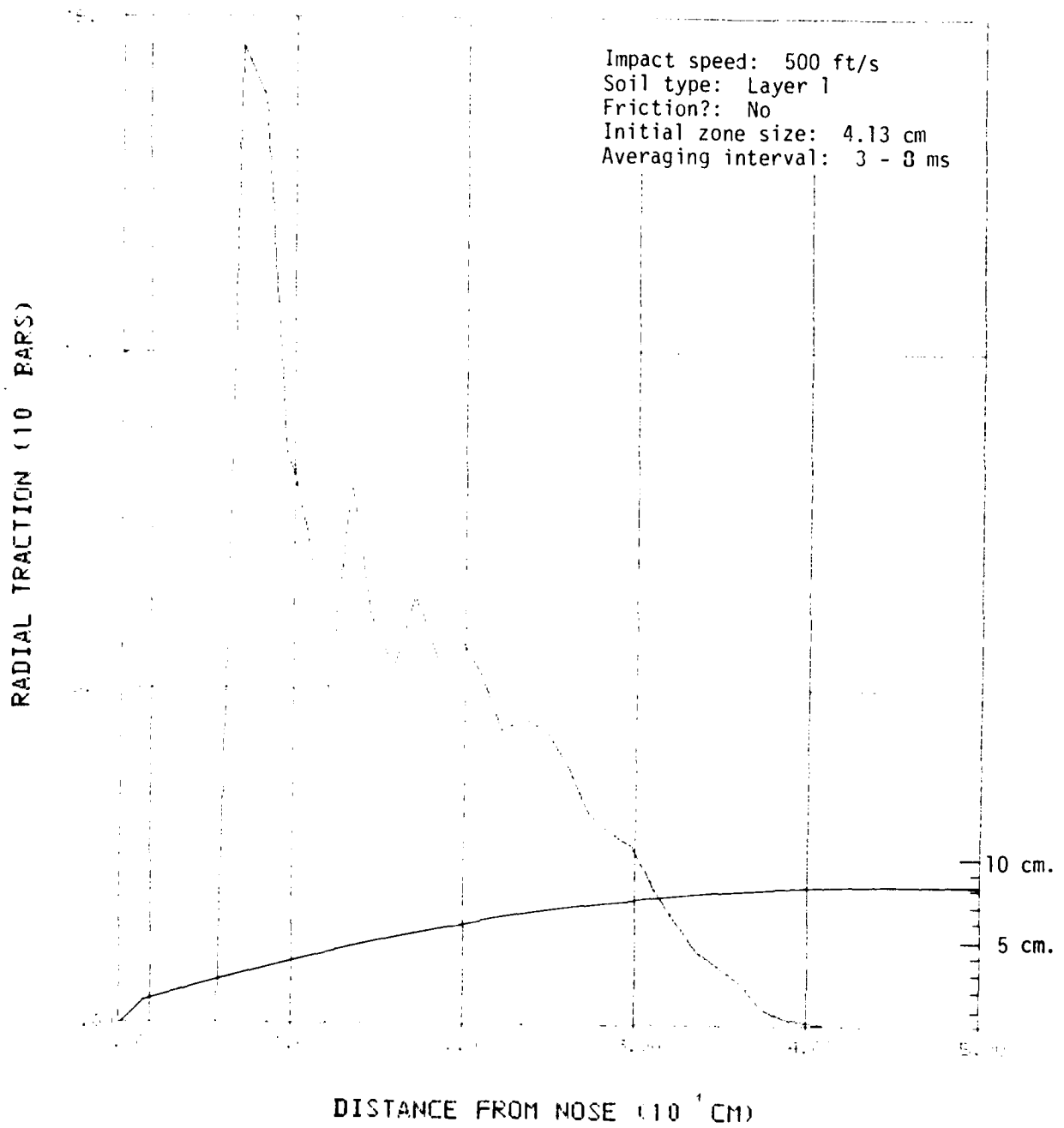
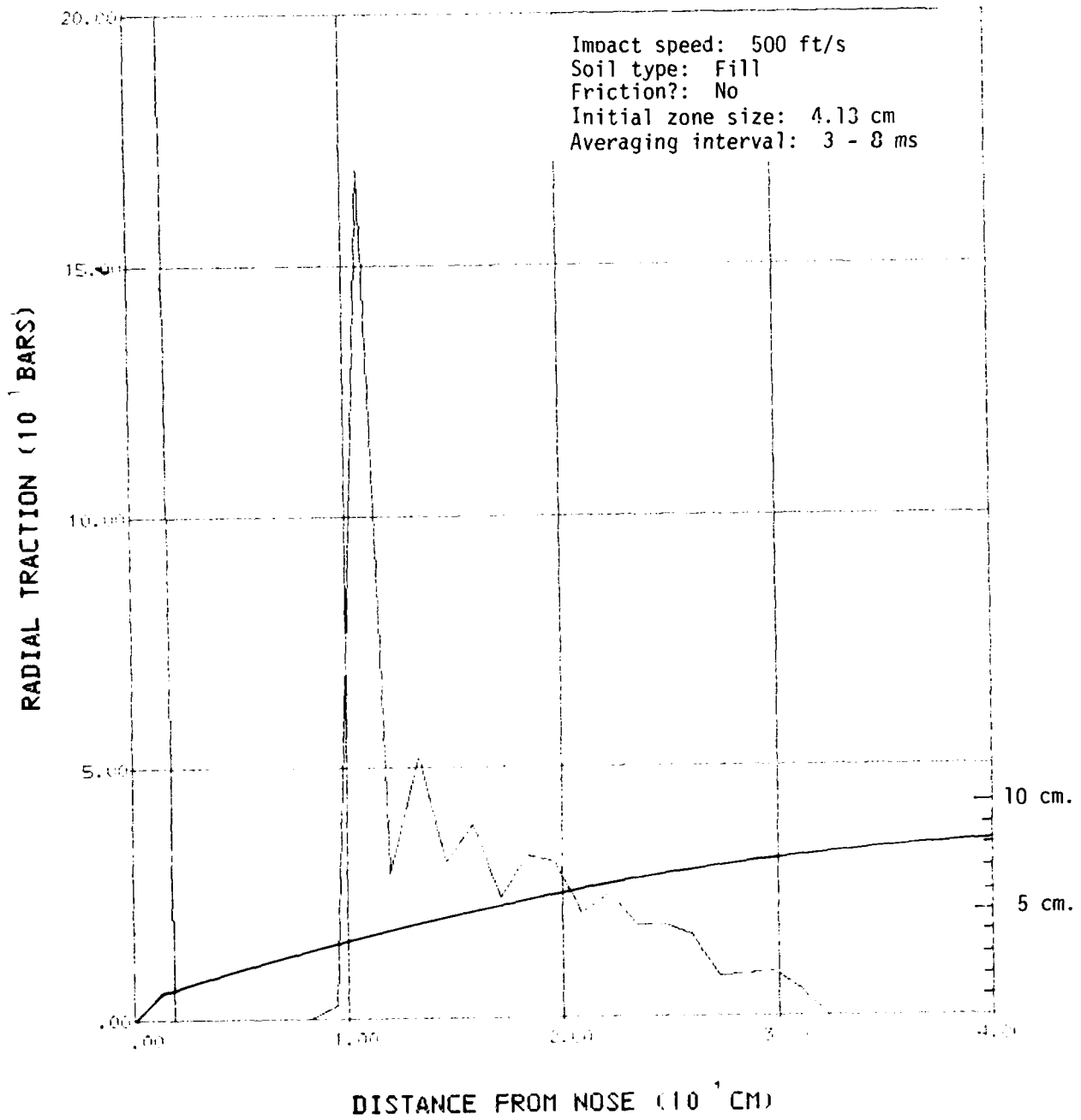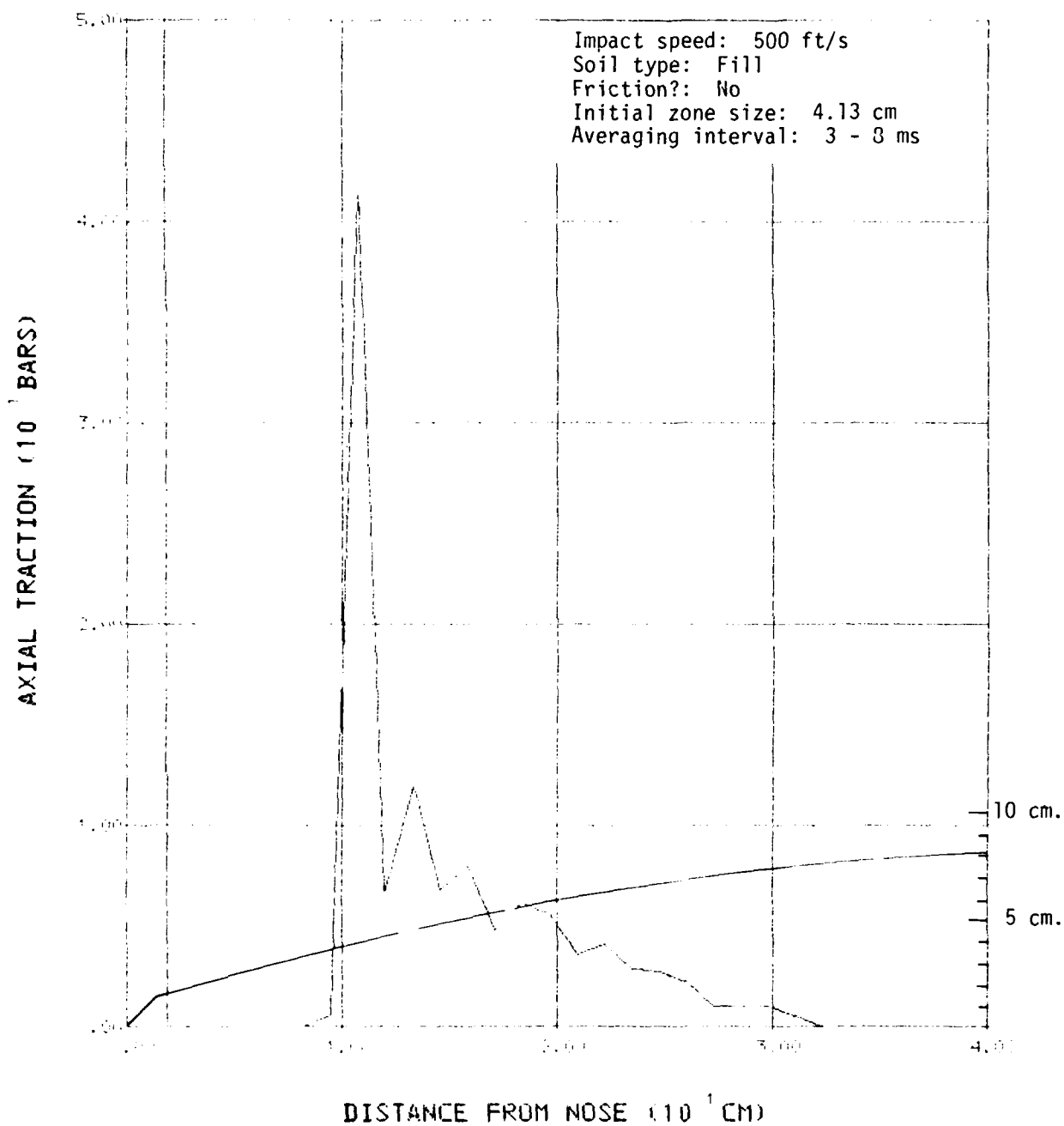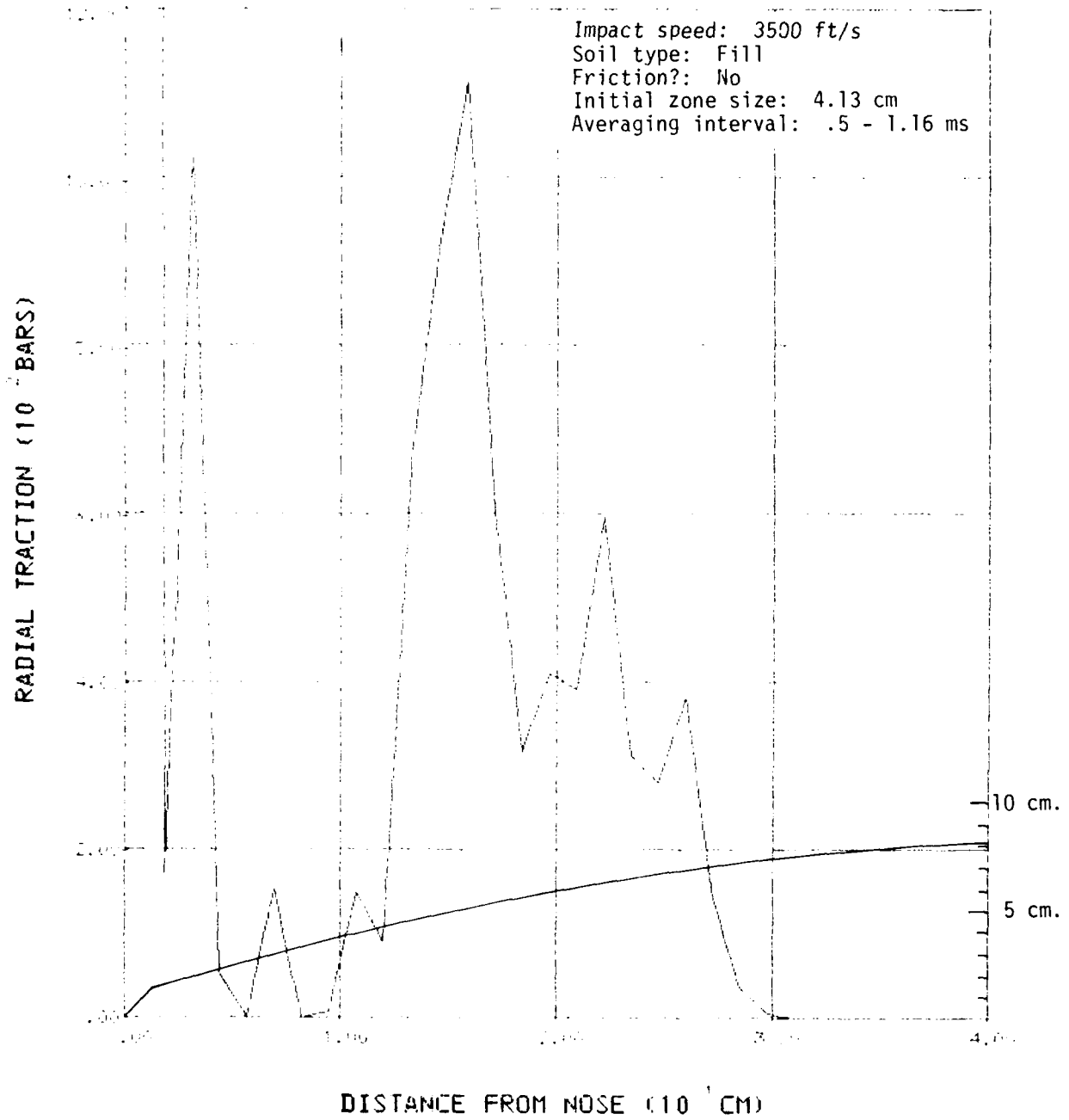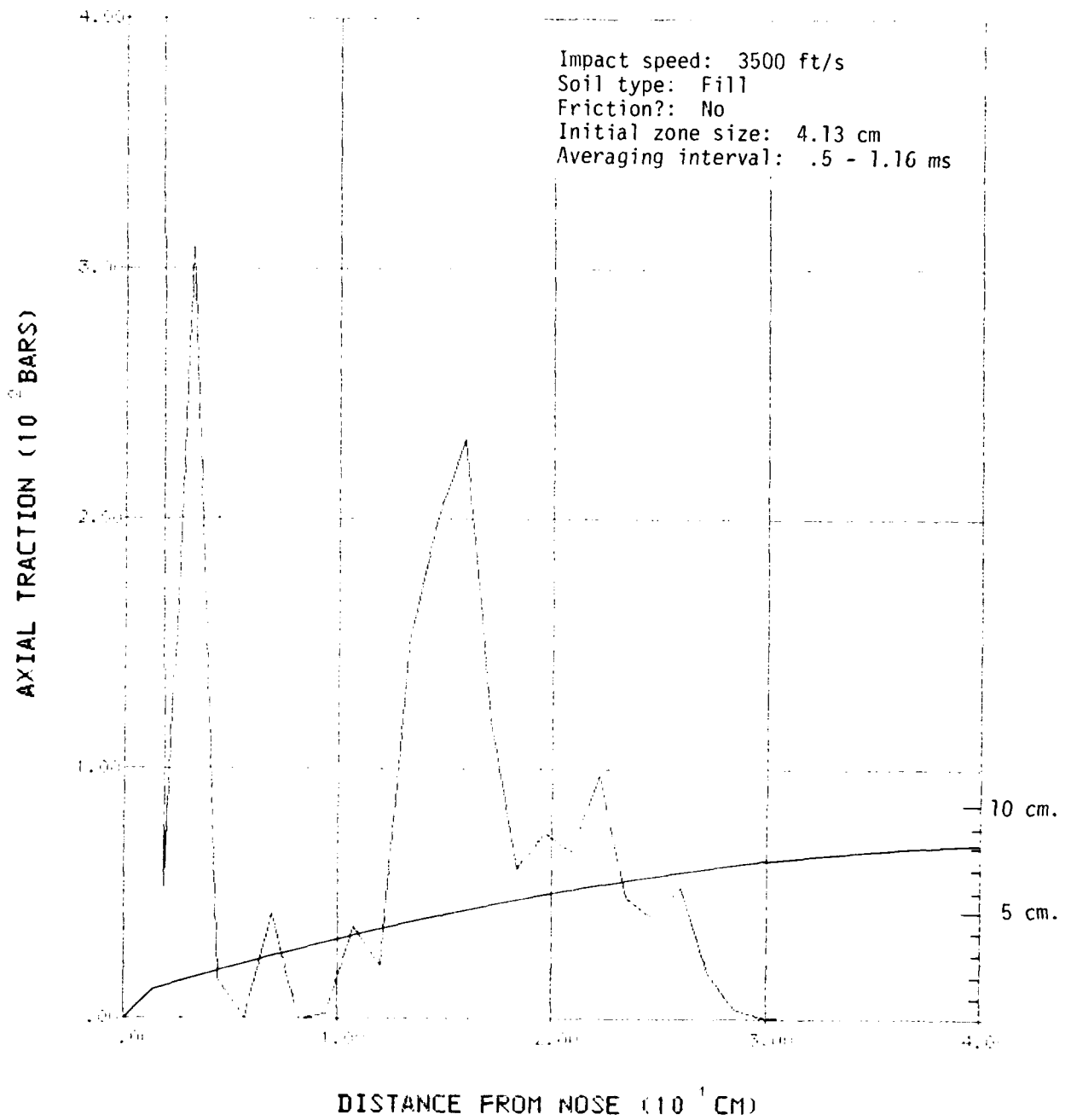Figure 4.2-13. Time-averaged axial traction profile for Case 2.

EPW PROBLEM 2
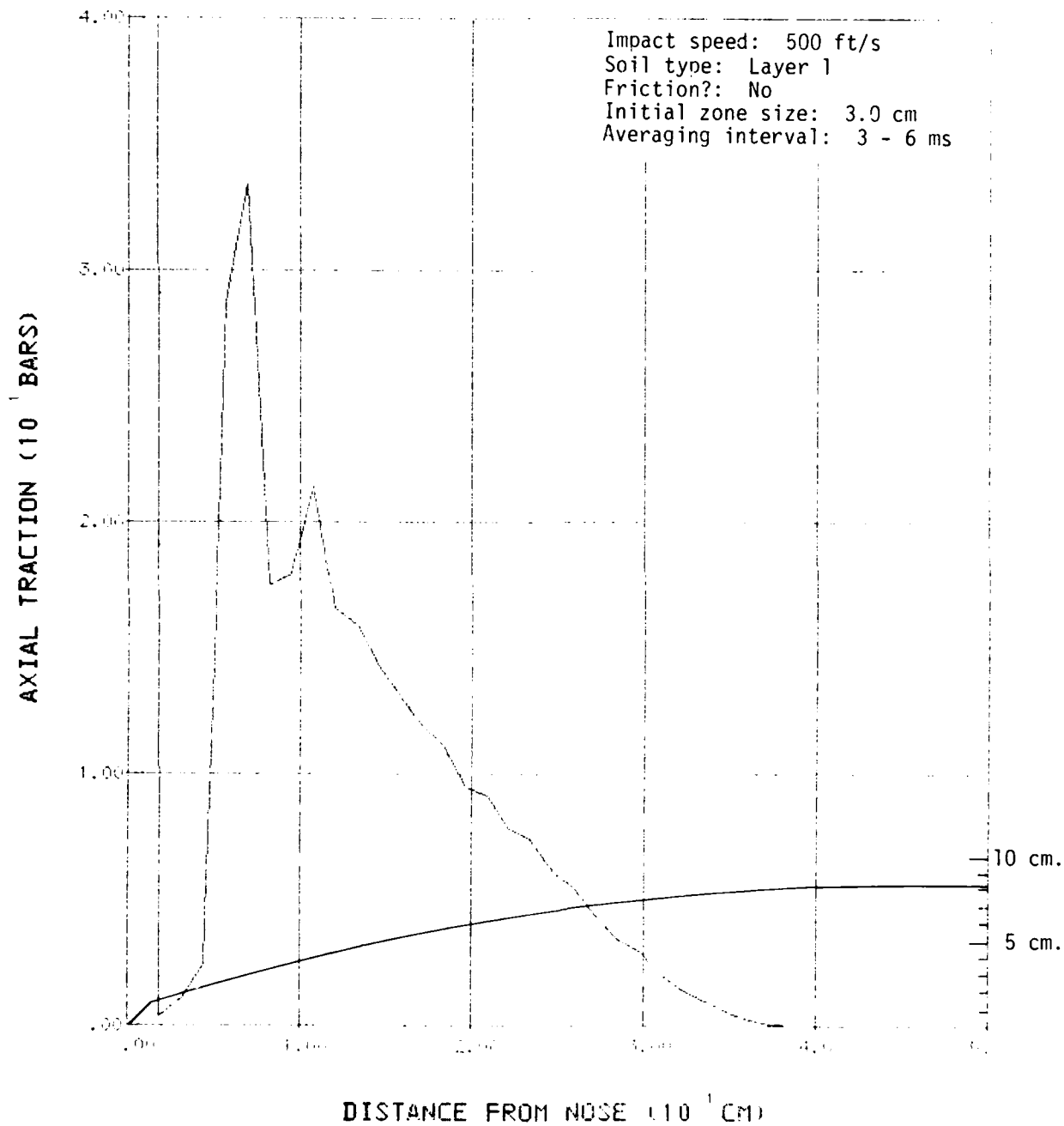
Impact speed: 500 ft/s
Soil type: Layer 1
Friction?: No
Initial zone size: 4.13 cm
Averaging interval: 3 - 8 ms

AXIAL TRACTION (10⁻¹ BARS)

DISTANCE FROM NOSE (10¹ CM)
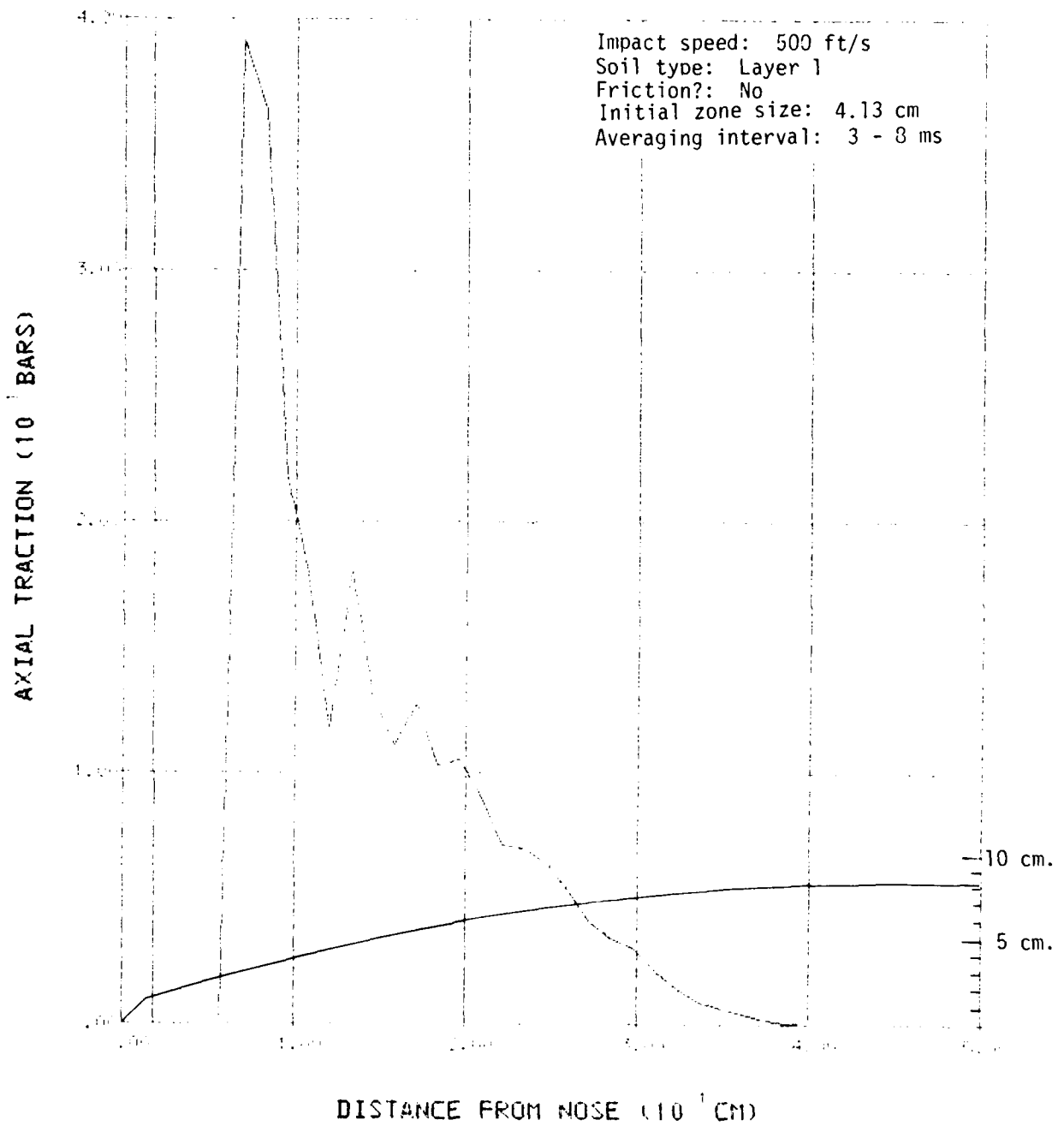
Figure 4.2-14. Time-averaged radial traction profile for Case 2.

EPW PROBLEM 3

Impact speed: 500 ft/s
Soil type: Fill
Friction?: No
Initial zone size: 4.13 cm
Averaging interval: 3 - 8 ms

Figure 4.2-15. Time-averaged axial traction profile for Case 3.

60

EPW PROBLEM 3

Impact speed: 500 ft/s
Soil type: Fill
Friction?: No
Initial zone size: 4.13 cm
Averaging interval: 3 - 8 ms

AXIAL TRACTION (10 ' BARS)

DISTANCE FROM NOSE (10 ' CM)

Figure 4.2-16. Time-averaged radial traction profile for Case 3.

EPW PROBLEM 4

Figure 4.2-17. Time-averaged axial traction profile for Case 4.

62

Figure 4.2-18. Time-averaged radial traction profile for Case 4.

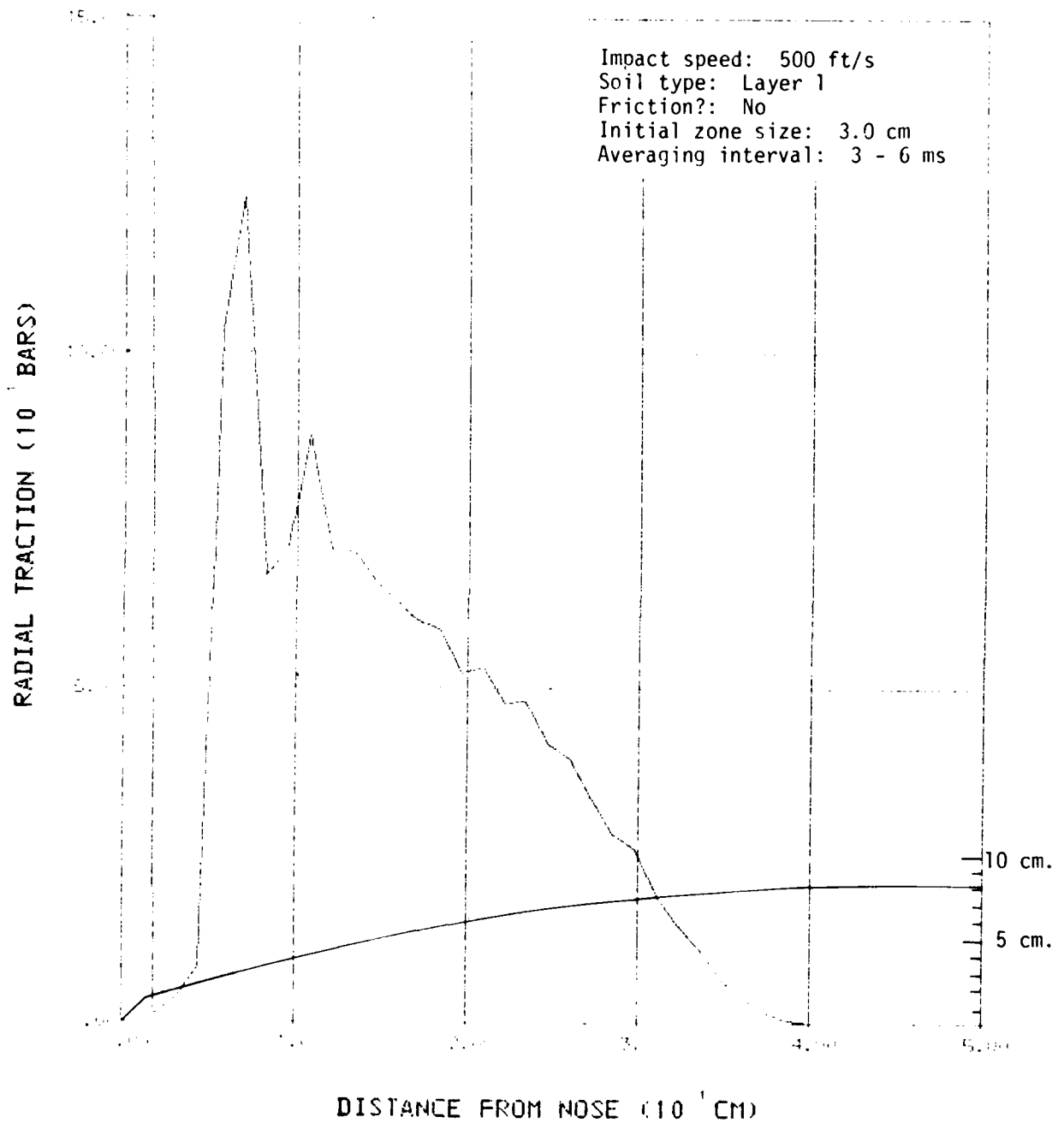Figure 4.2-19. Time-averaged axial traction profile for Case 5.

EPW PROBLEM 5

Impact speed: 500 ft/s
Soil type: Layer 1
Friction?: No
Initial zone size: 3.0 cm
Averaging interval: 3 - 6 ms

RADIAL TRACTION (10 BARS)

DISTANCE FROM NOSE (10 CM)

Figure 4.2-20. Time-averaged radial traction profile for Case 5.

4.3 ADDITIONAL PLOTS OF RESULTS

In this section, additional computational results are
presented in the form of graphs. The graphs labeled 4.3-1
pertain to Case 1, etc. A letter is appended after the case
number to identify the individual plot. The plots shown in each
set are:

a. Velocity versus time
b. Velocity versus depth
c. Computing grid configuration at 2 ms
d. Computing grid configuration at 4 ms
e. Computing grid configuration at 6 ms
f. Computing grid configuration at 8 ms

Figure 4.3-0 presents the initial computing grid configuration.
For Case 4, the impact at 3500 f/s, the configurations are given
at times when the penetration depth was about 1, 2, 3, and 4 feet.
Note that the configurations have been expanded by a factor of
two laterally to provide better resolution of the small zones
near the projectile.

For Case 5, no configuration plots are available for the
report. Instead, a movie was made of Case 5 using a continuous
sequence of configuration plots.

EPW PROBLEM 1
CYCLE   0   TIME = 0.000   SEC.

DEPTH (10 CM.)
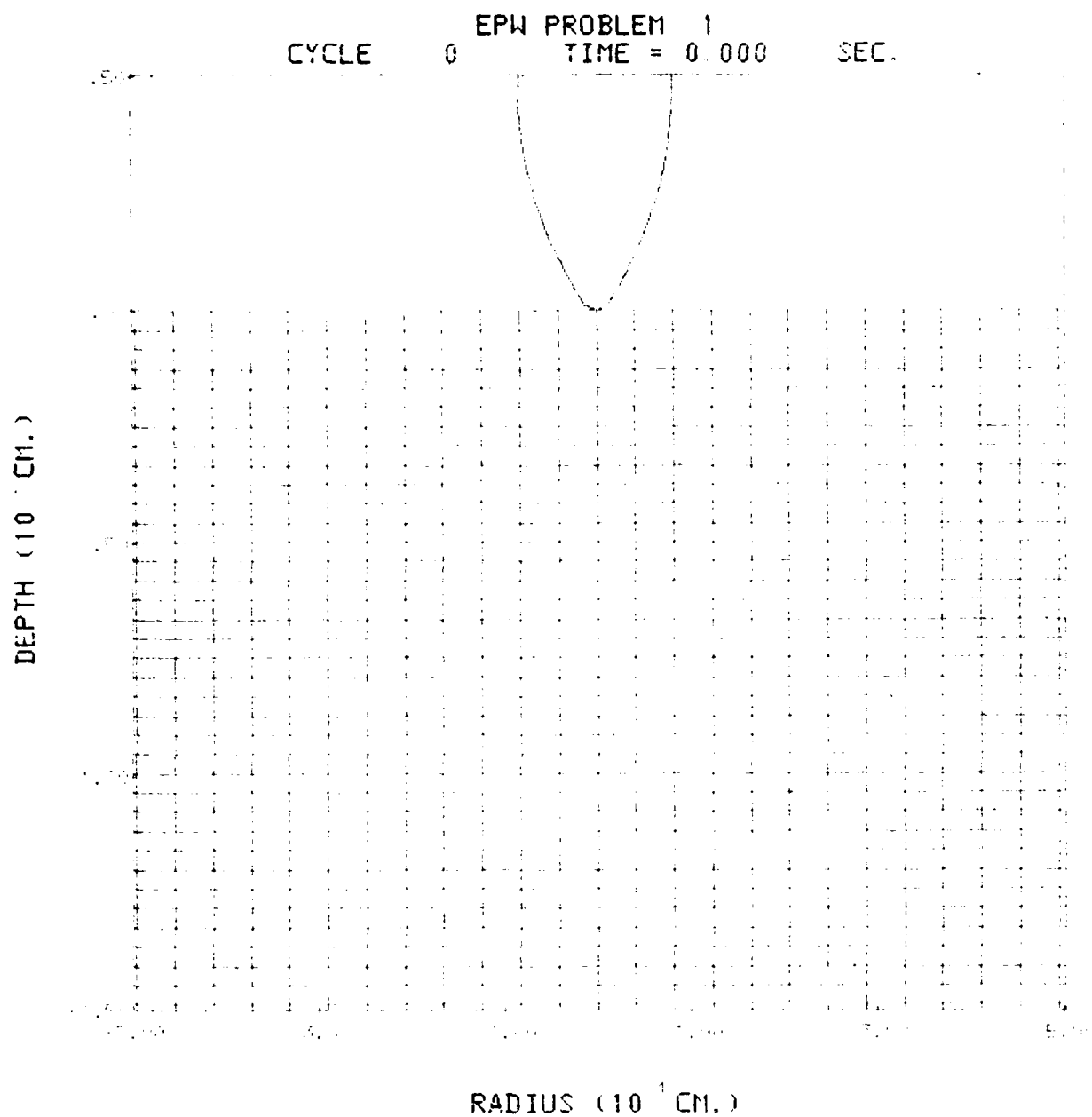
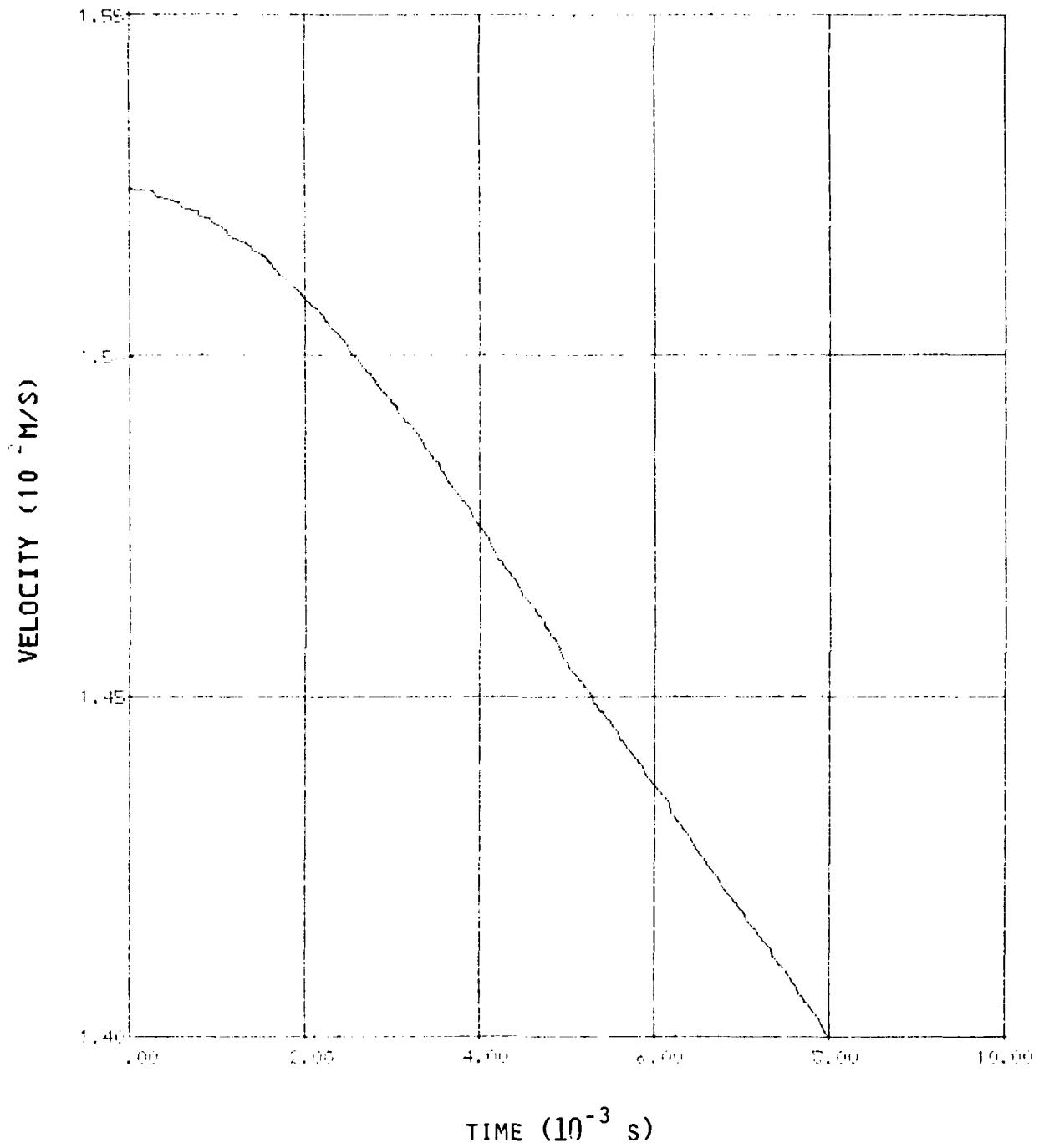RADIUS (10 CM.)

4.3-0. Initial Grid Configuration Plot
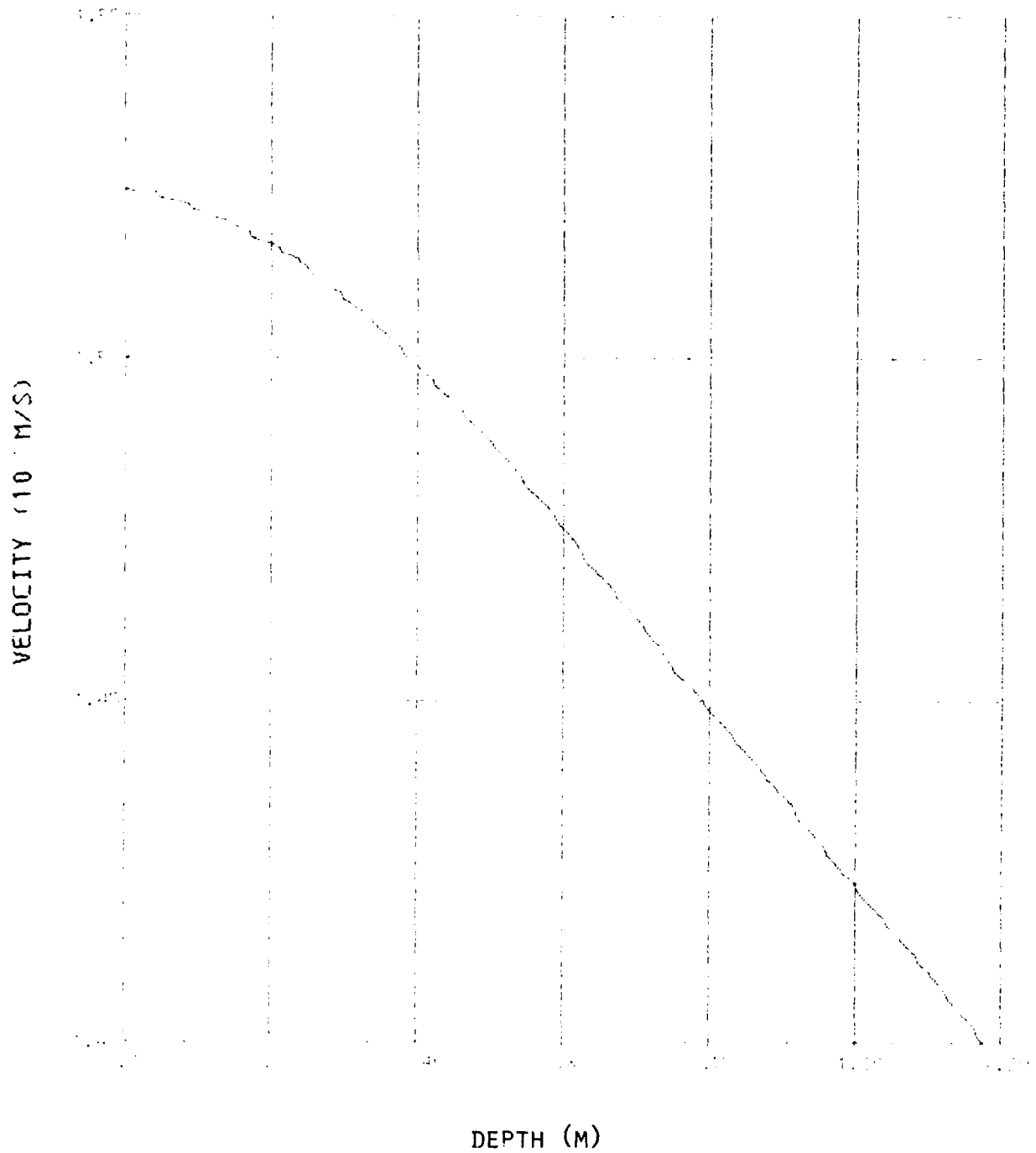
67

EPW PROBLEM 1

Figure 4.3-1a. Penetrator velocity history for Case 1.

Figure 4.3-1b. Velocity penetrator depth cross plot for Case 1.

EPW PROBLEM 1
CYCLE 118   TIME = 2.00S-08 SEC

Figure 4.3-1c.   Computing grid configuration at 2 ms for Case 1.

EPW PROBLEM 1
CYCLE 259   TIME = 4.01e-03 SEC

DEPTH (10 CM.)

RADIUS (10 CM.)

Figure 4.3-1d.   Computing grid configuration at 4 ms for Case 1.

71

EPW PROBLEM 1
CYCLE 335   TIME = 6.020-03 SEC.

DEPTH (10 CM.)

RADIUS (10 CM.)

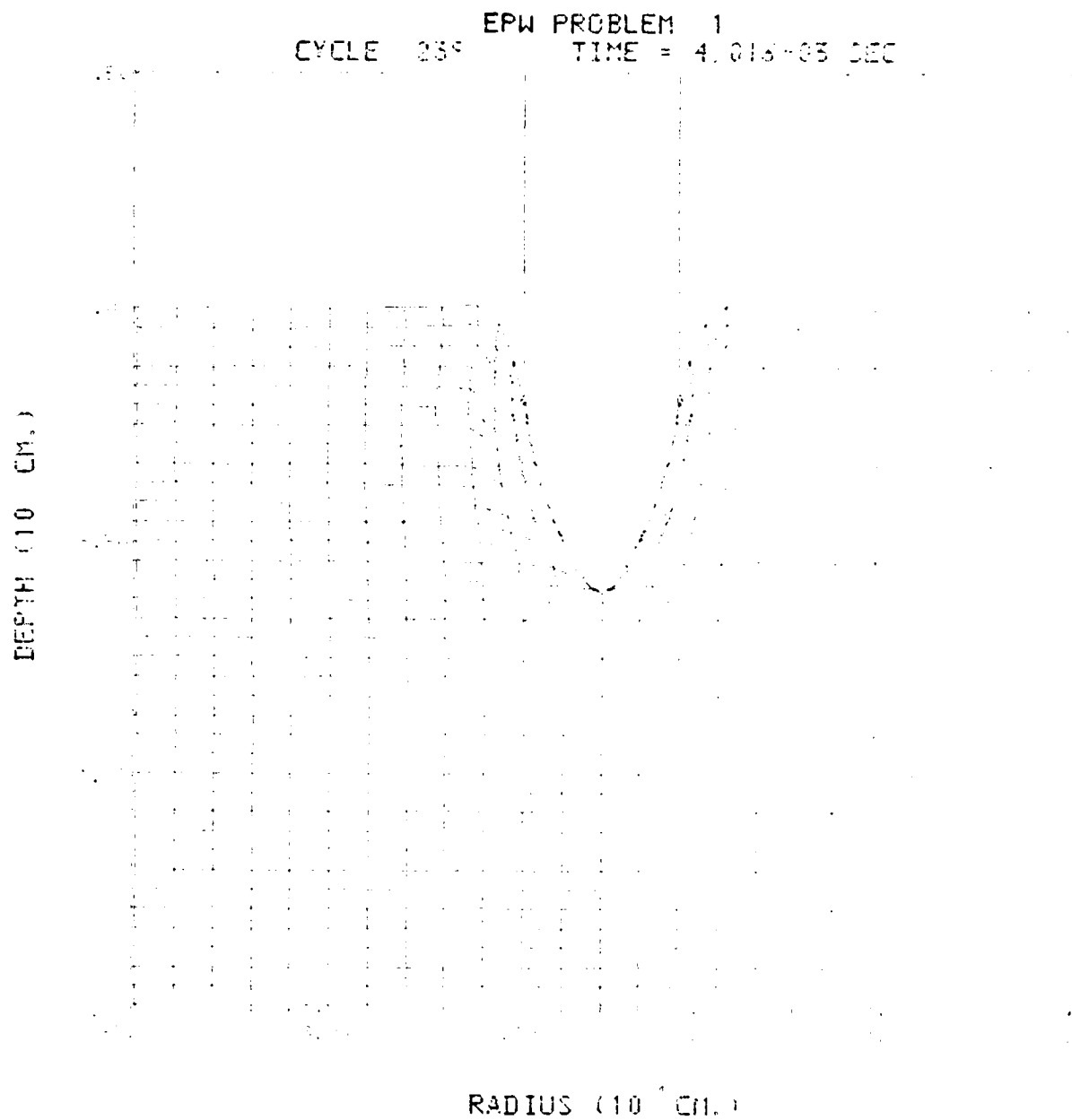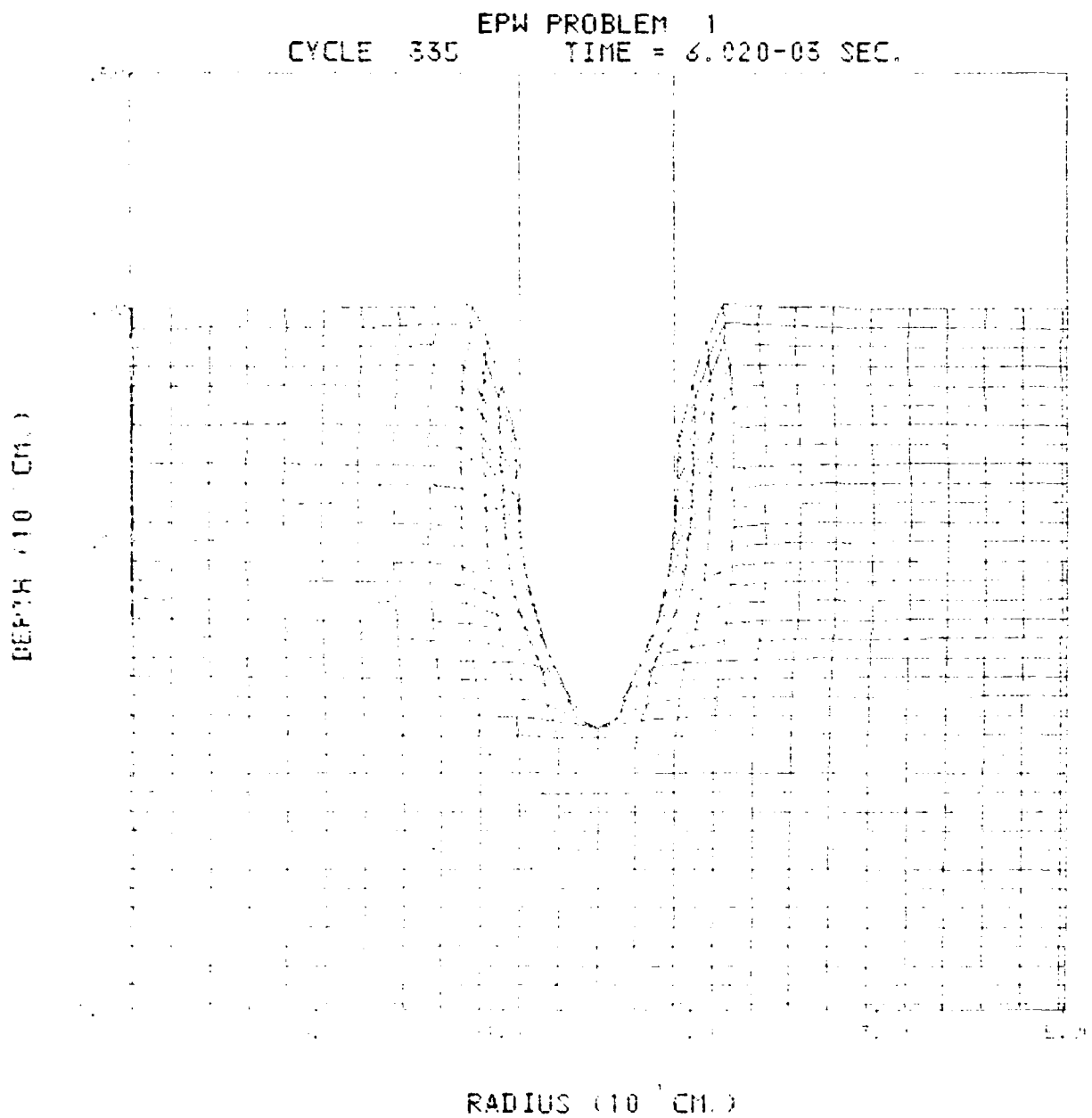Figure 4.3-1e.   Computing grid configuration at 6 ms for Case 1.

EPW PROBLEM 1
CYCLE 430   TIME = 8.016-03 SEC.
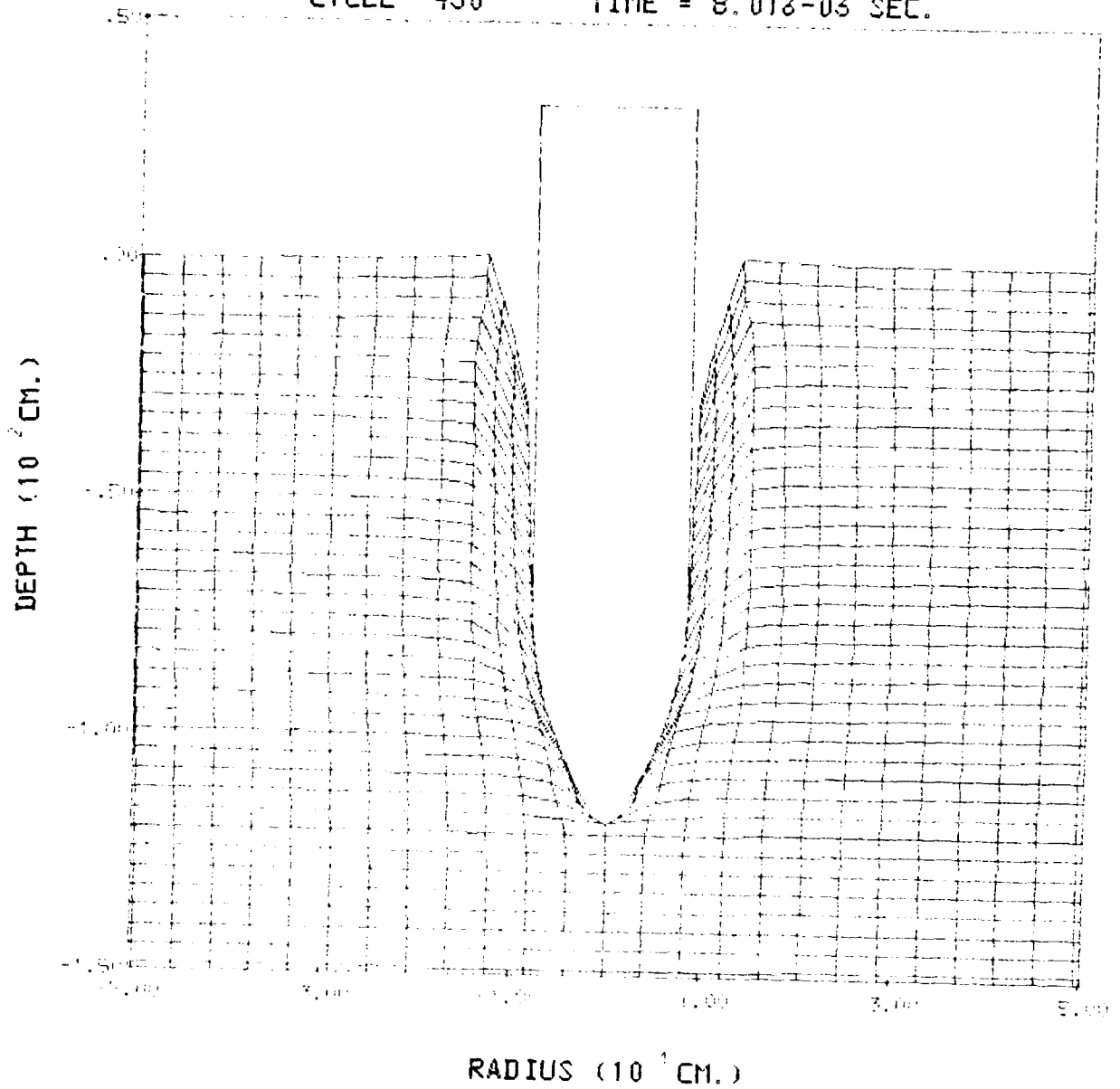
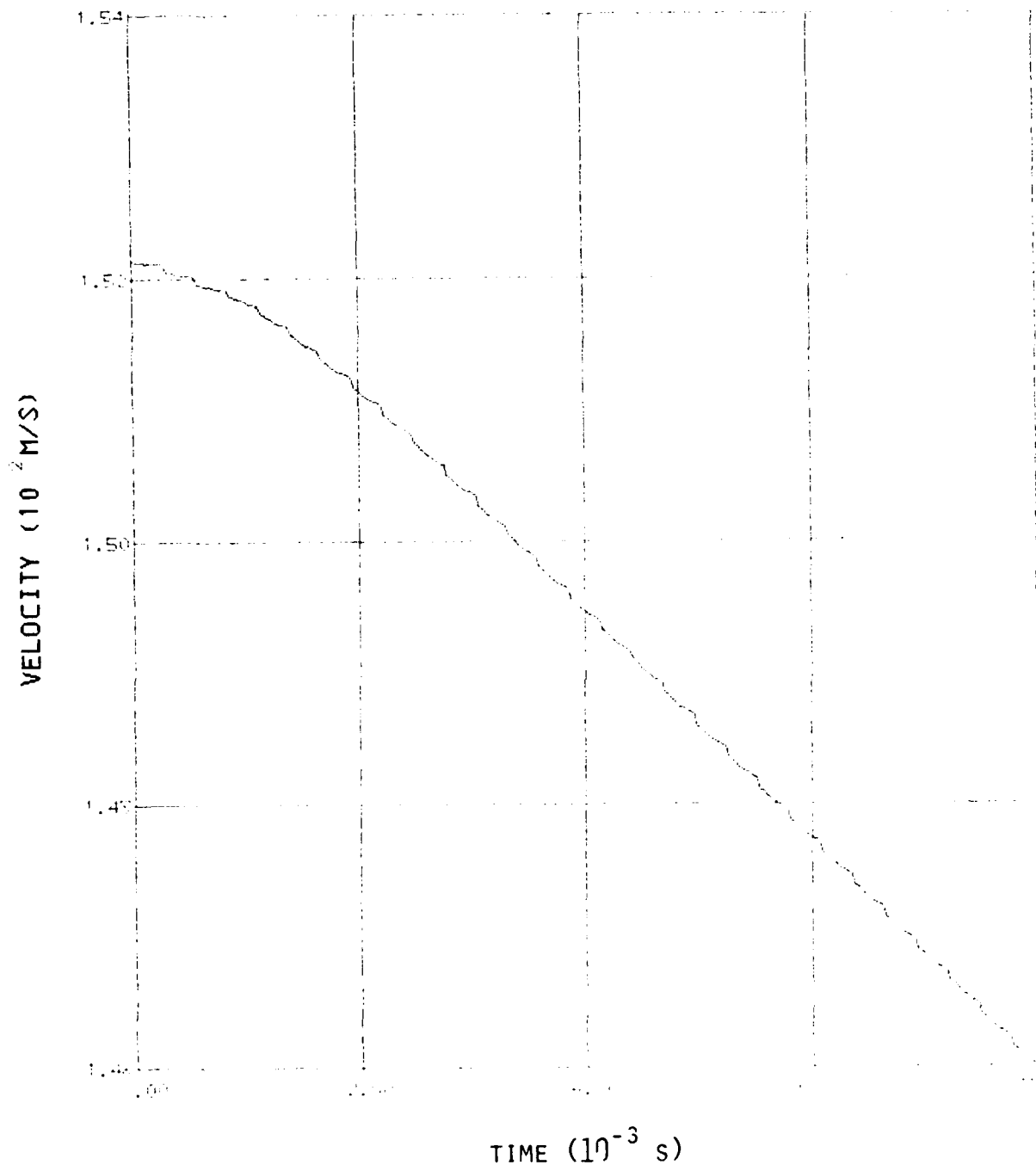Figure 4.3-1f.   Computing grid configuration at 8 ms for Case 1.

73

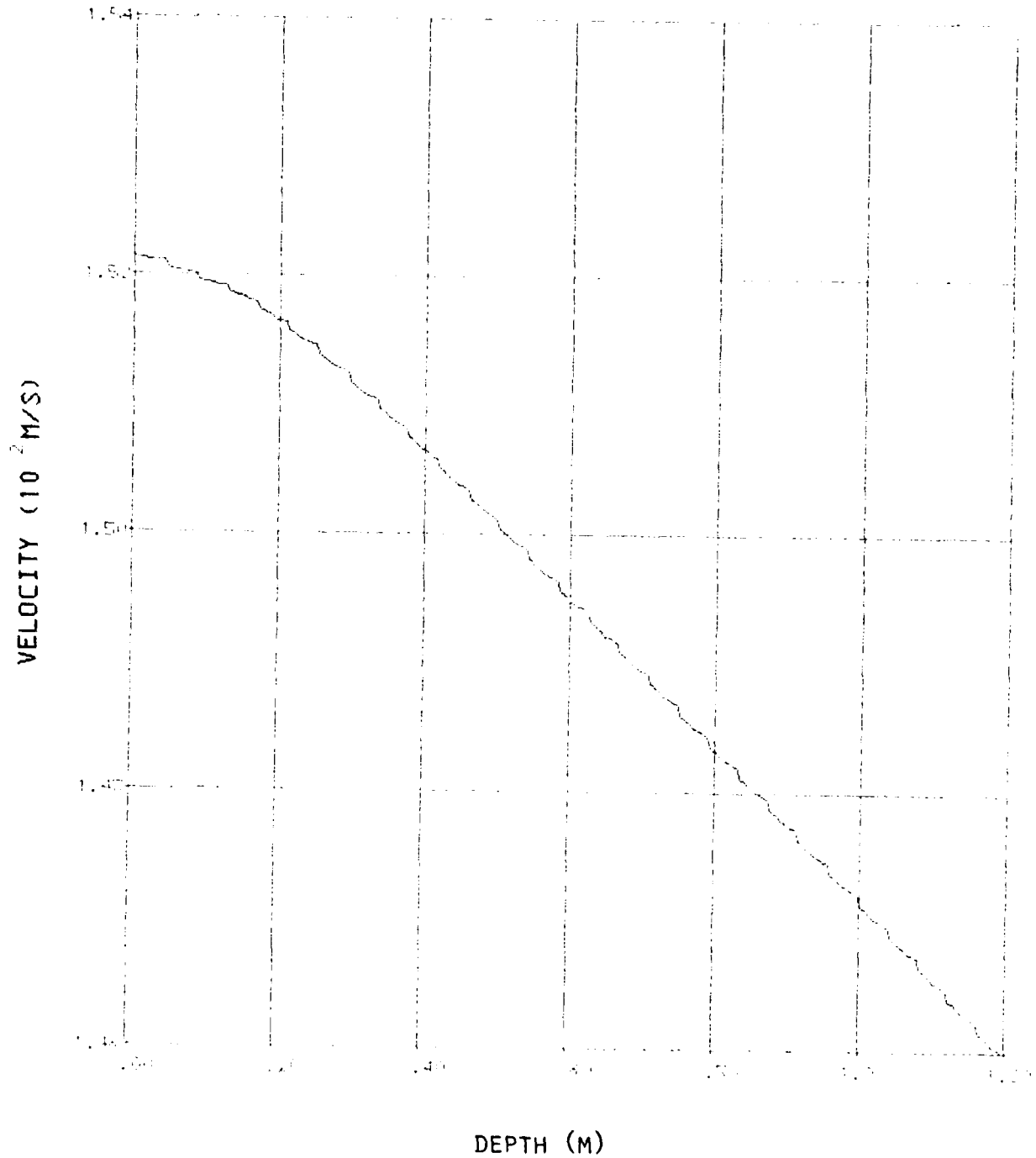Figure 4.3-2a.   Penetrator velocity history for Case 2.

DEPTH (M)

Figure 4.3-2b. Velocity penetrator depth cross plot for Case 2.

Figure 4.3-2c. Computing grid configuration at 2 ms for Case 2.

EPW PROBLEM 2

CYCLE 203   TIME = 4.009-03 SEC.
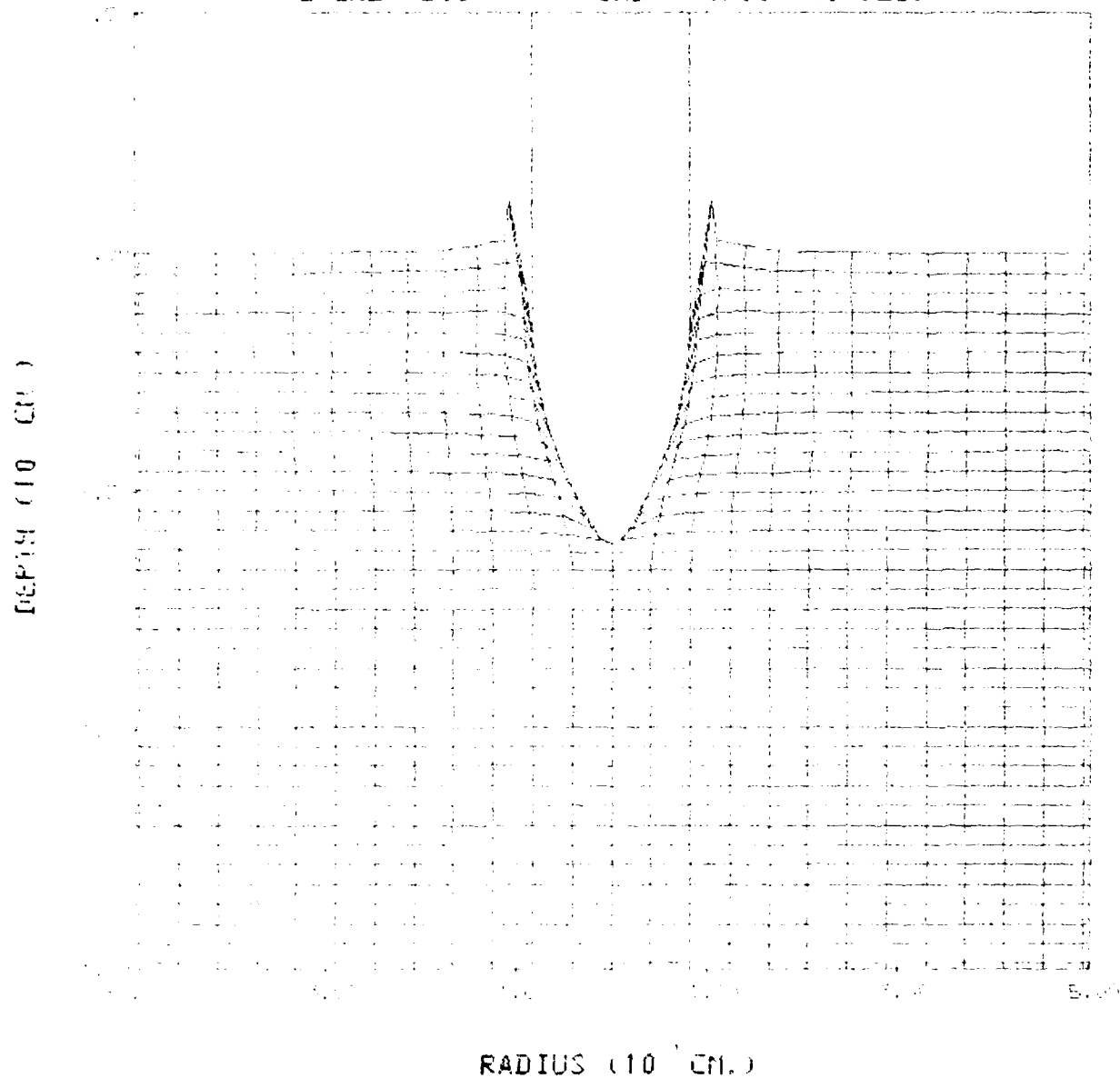
Figure 4.3-2d.   Computing grid configuration at 4 ms for Case 2.

EPW PROBLEM 2

CYCLE 318   TIME = 6.004-03 SEC.

Figure 4.3-2e.   Computing grid configuration at 6 ms for Case 2.

EPW PROBLEM 2
CYCLE 447   TIME = 8.010-03 SEC.

Figure 4.3-2f. Computing grid configuration at 8 ms for Case 2.

79

Figure 4.3-3a. Penetrator velocity history for Case 3.
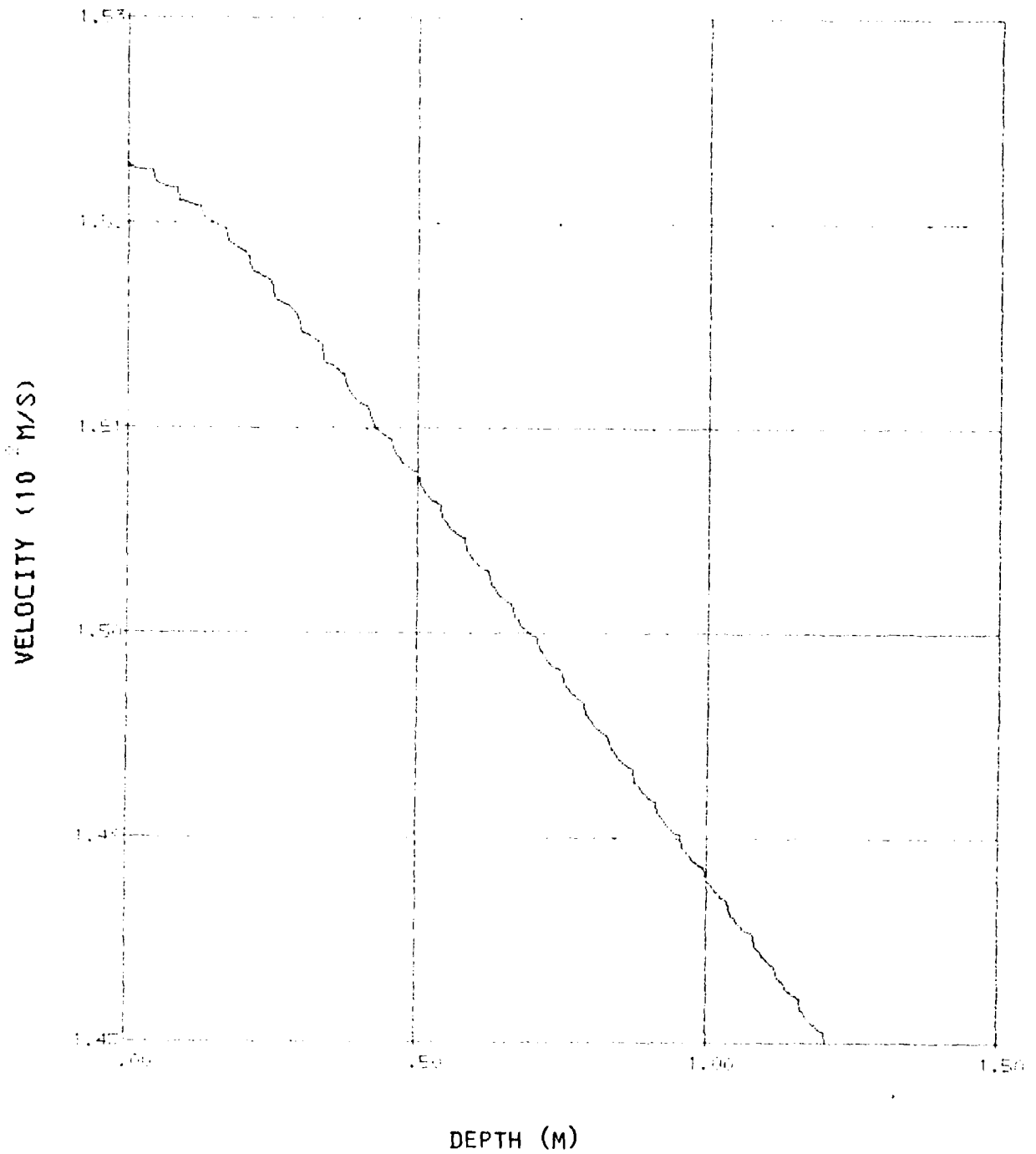
DEPTH (M)

Figure 4.3-3b. Velocity penetrator depth cross plot for Case 3.

EPW PROBLEM 3
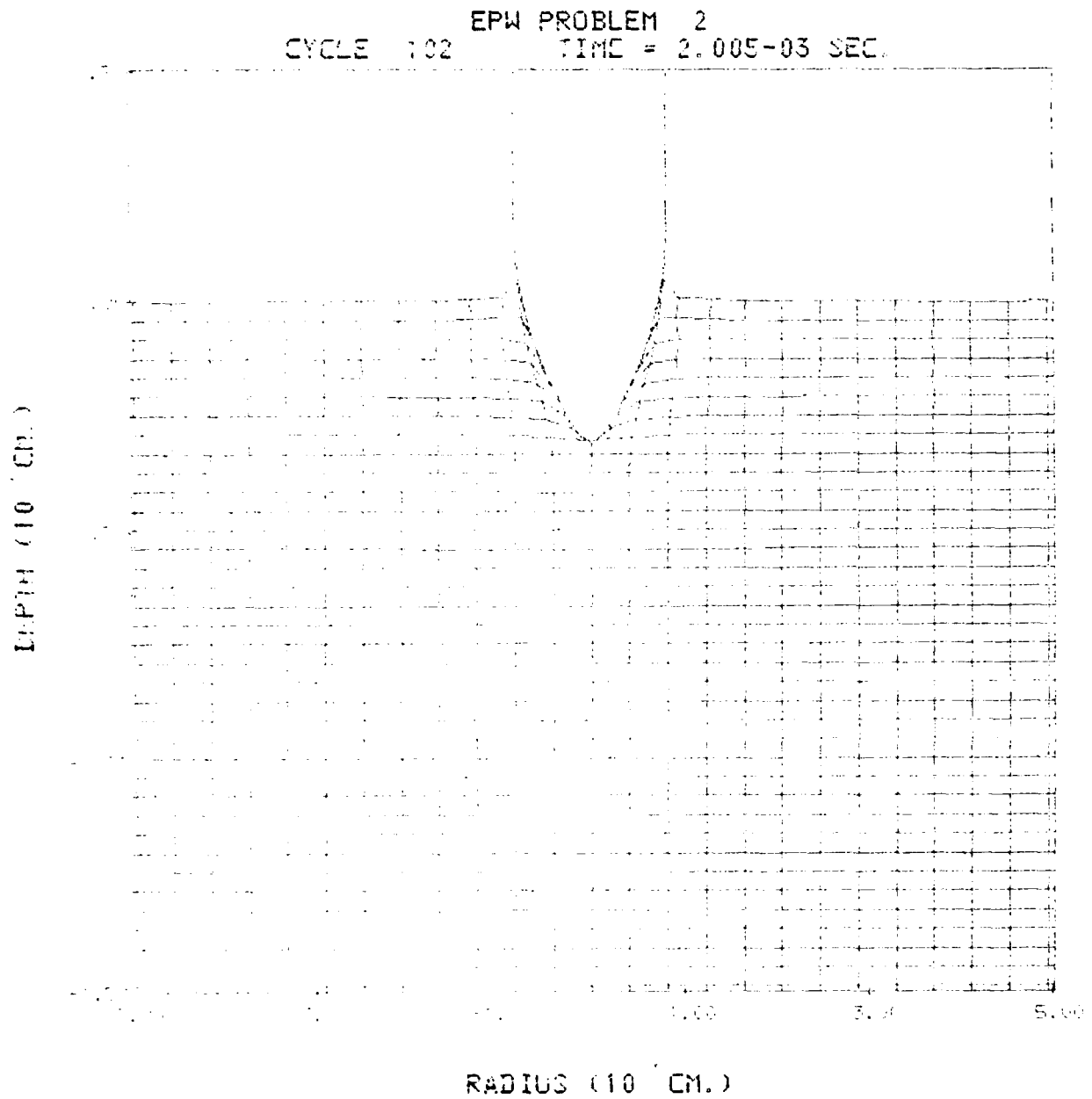CYCLE   71   TIME = 2.004-03 SEC.
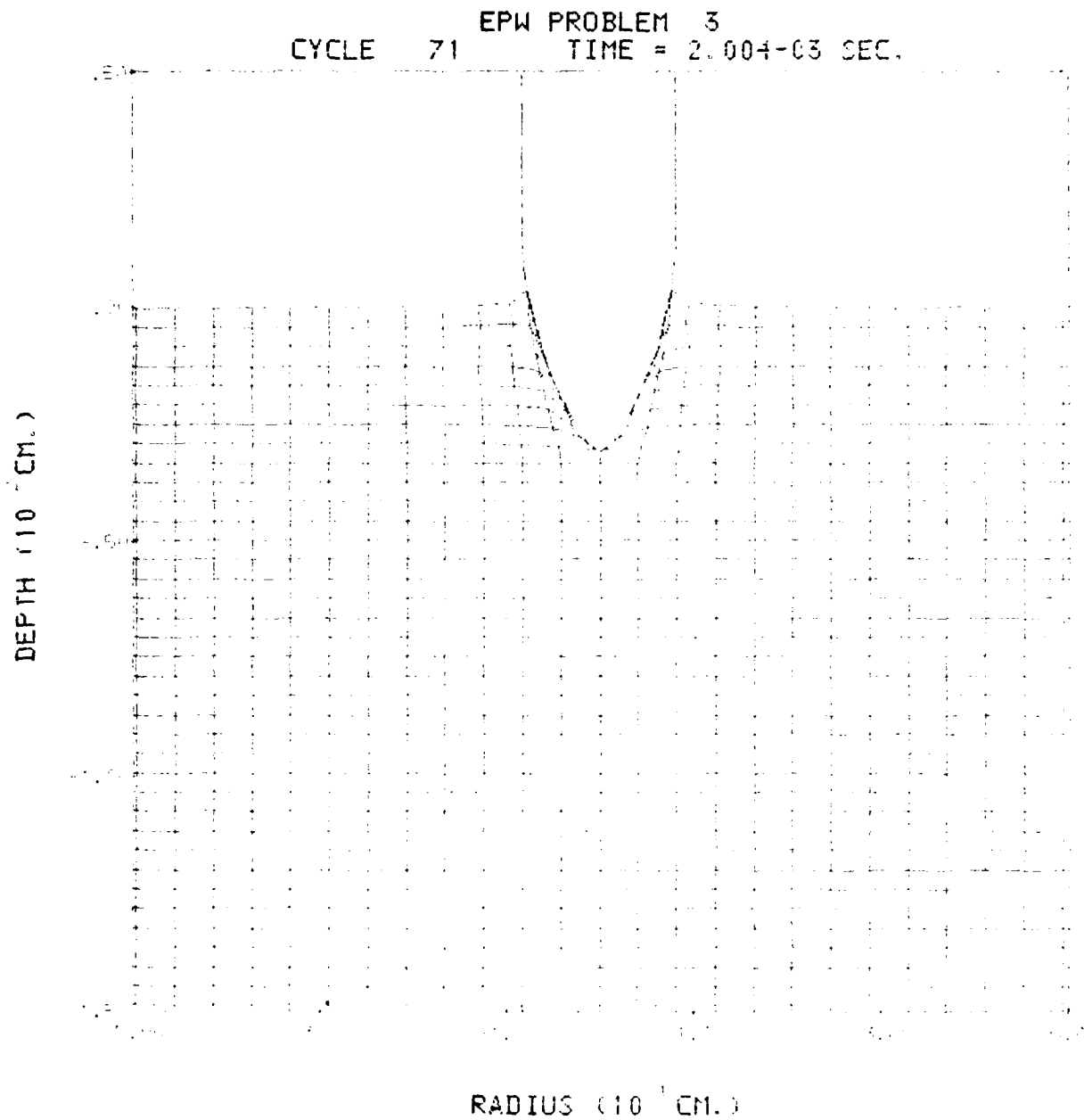
Figure 4.3-3c.   Computing grid configuration at 2 ms for Case 3.

EPW PROBLEM 3
CYCLE 138   TIME = 4.009-03 SEC
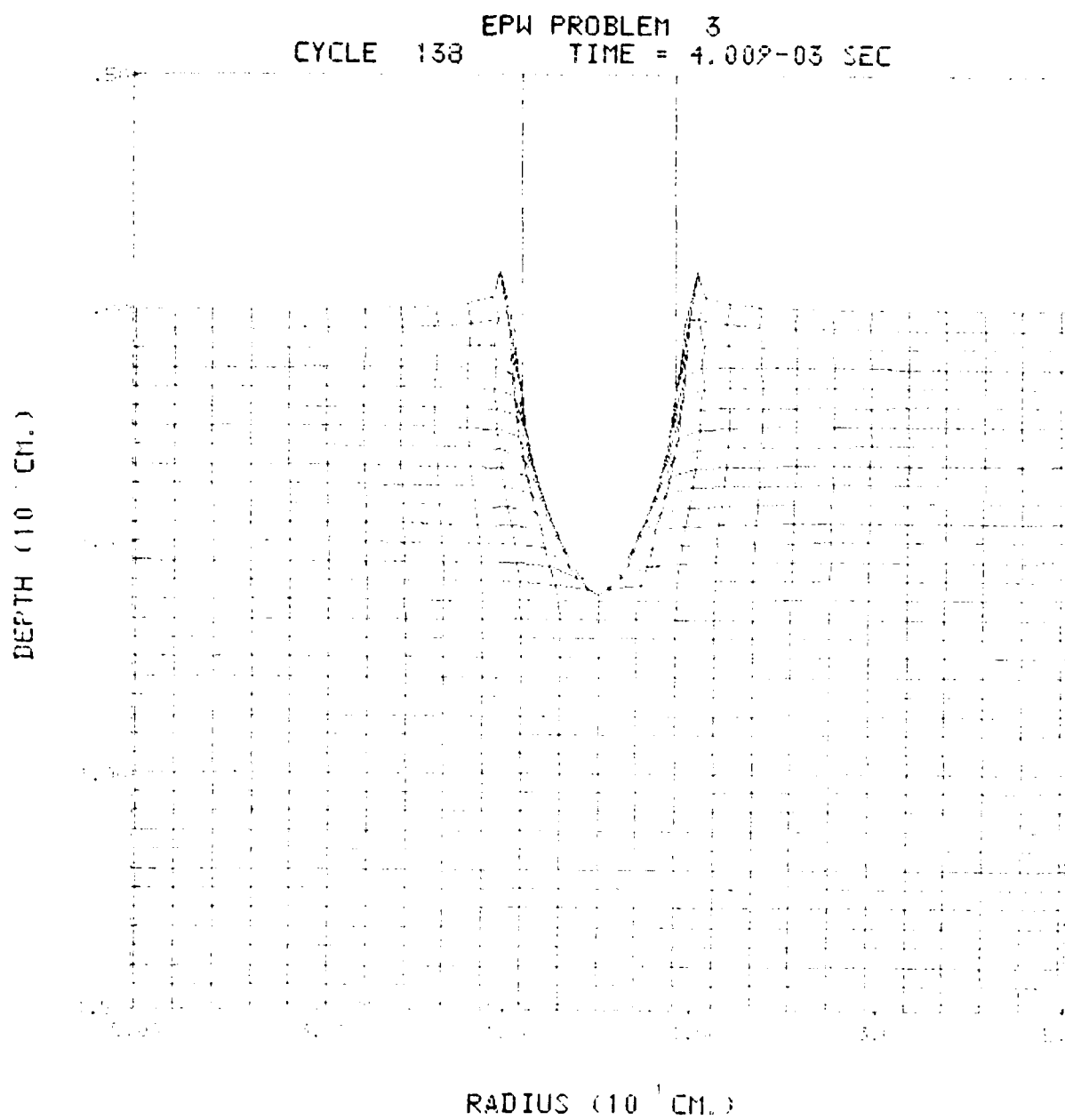
Figure 4.3-3d.   Computing grid configuration at 4 ms for Case 3.

EPW PROBLEM 3
CYCLE 216   TIME = 6.000-03 SEC.

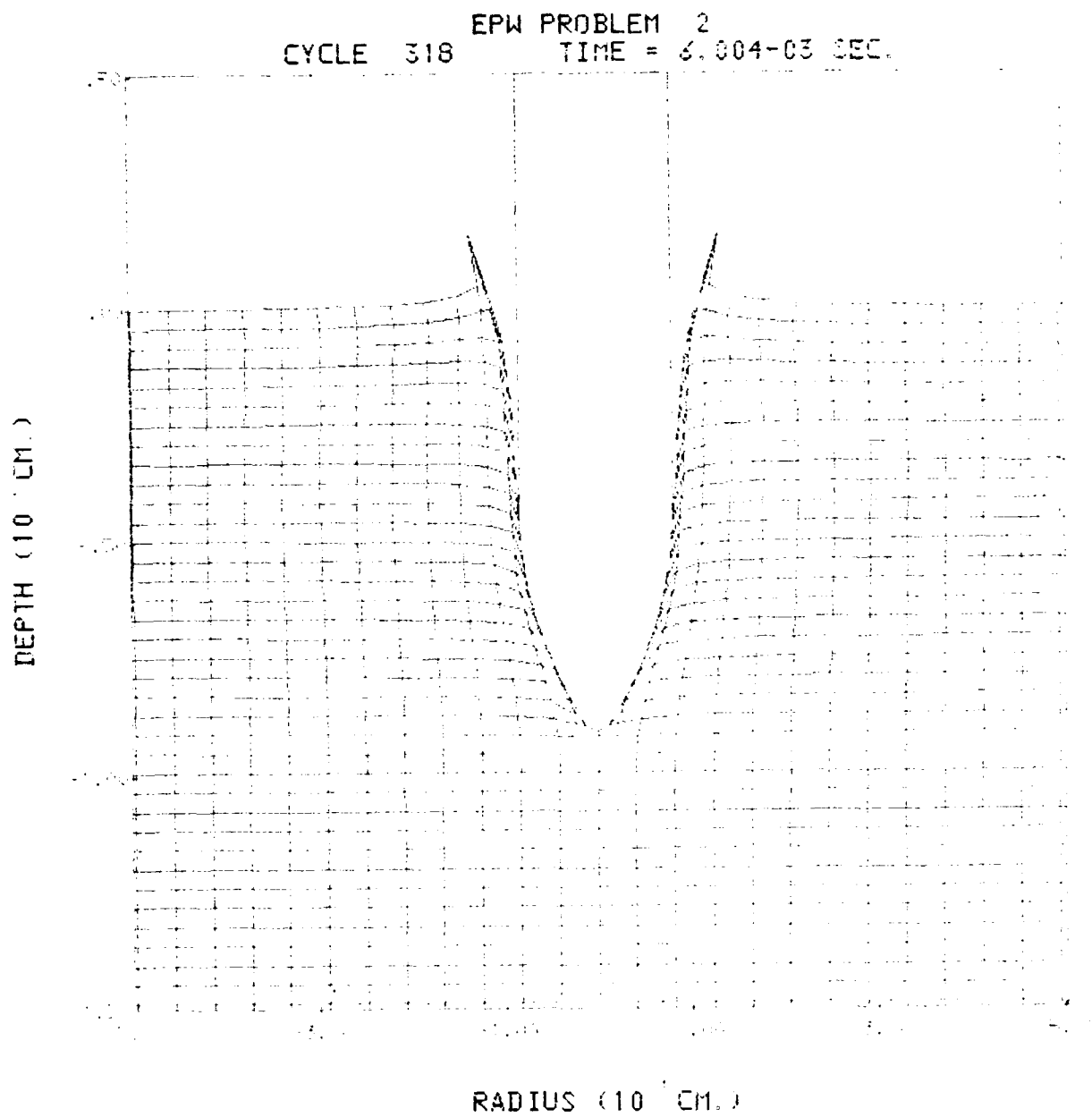DEPTH (10 CM.)

RADIUS (10^1 CM.)
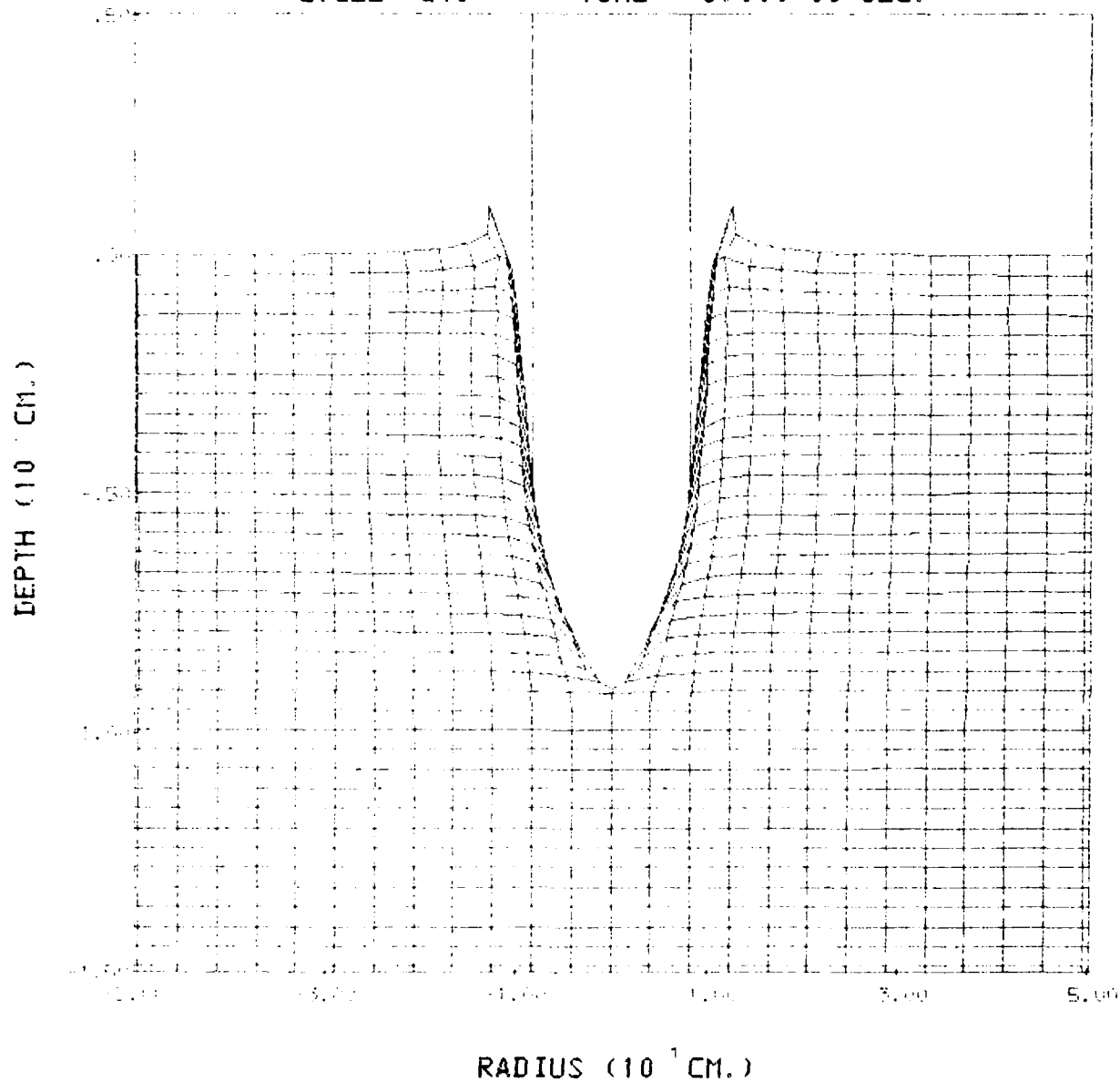
Figure 4.3-3e.   Computing grid configuration at 6 ms for Case 3.
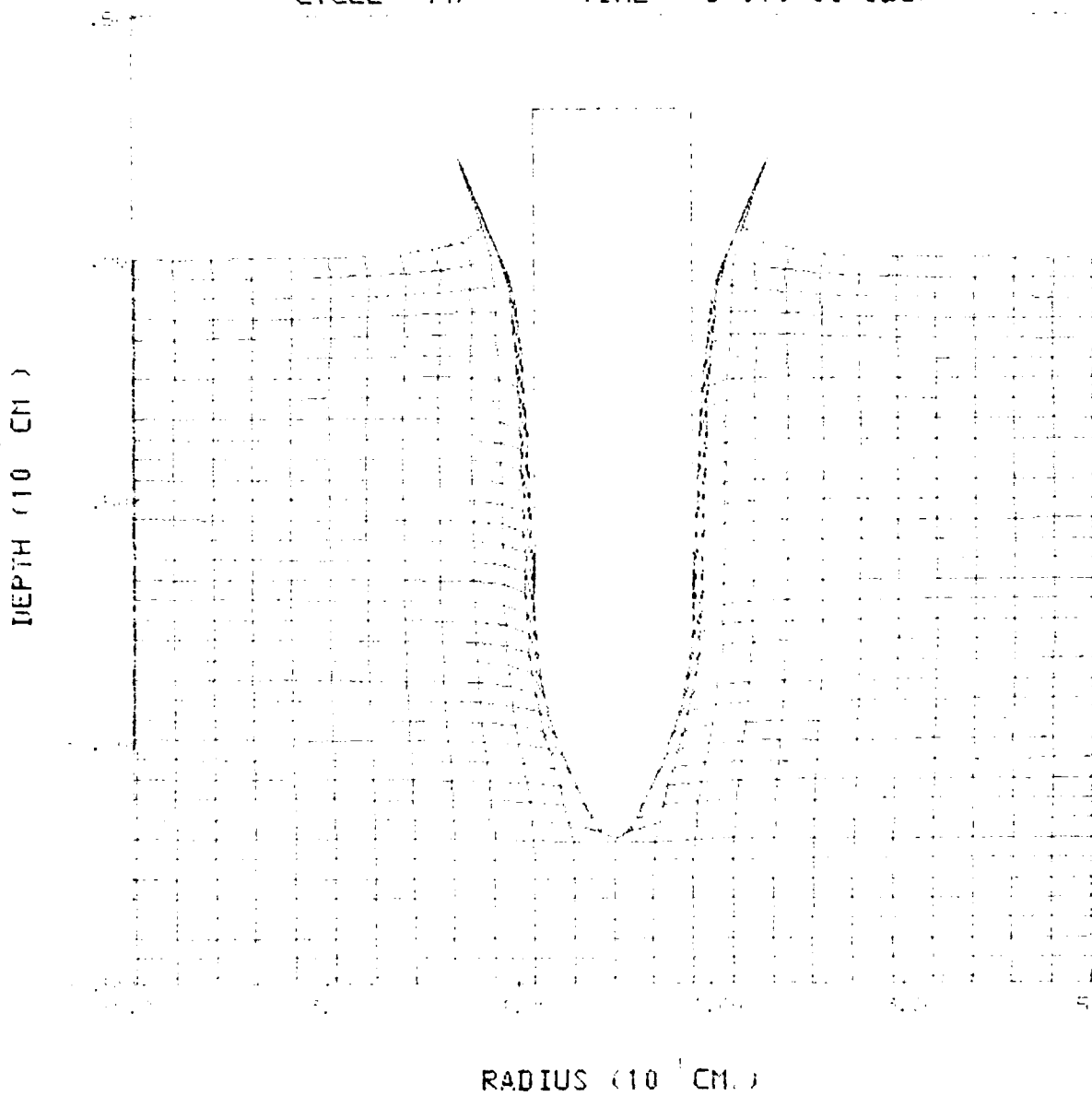
EPW PROBLEM 3
CYCLE 306   TIME = 8.018-03 SEC.

Figure 4.3-3f.   Computing grid configuration at 8 ms for Case 3.

EPW PROBLEM 4

Figure 4.3-4a. Penetrator velocity history for Case 4.

86

Figure 4.3-4b. Velocity penetrator depth cross plot for Case 4.

EPW PROBLEM 4
CYCLE 68   TIME = 2.891-04 SEC.

Figure 4.3-4c. Computing grid configuration at 2 ms for Case 4.

EPW PROBLEM 4
CYCLE 148   TIME = 5.800-04 SEC.

DEPTH (10 CM.)

RADIUS (10 CM.)
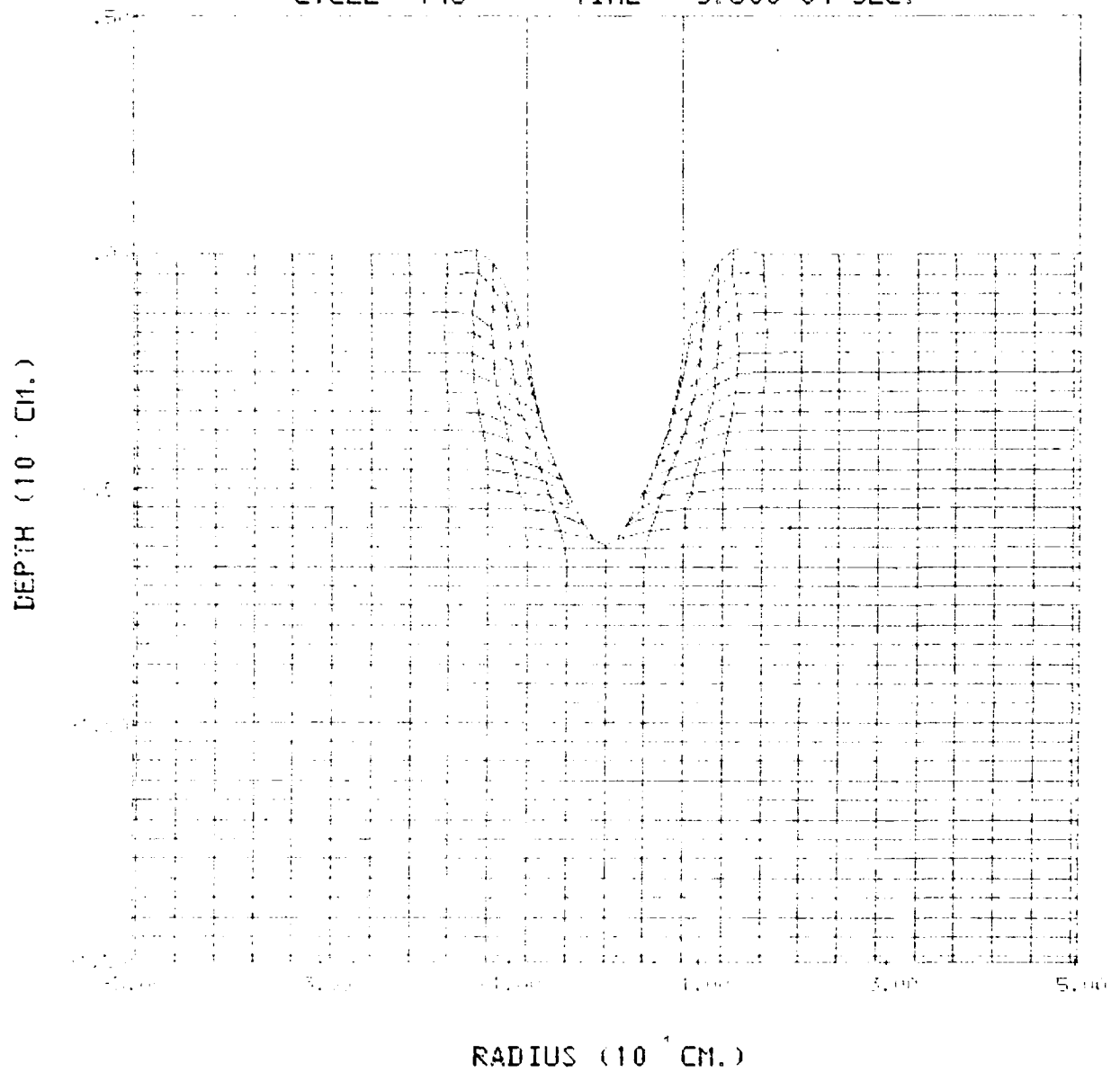
Figure 4.3-4d.   Computing grid configuration at 4 ms for Case 4.

EPW PROBLEM 4
CYCLE 315   TIME = 8.582-04 SEC

DEPTH (10 CM.)

RADIUS (10 CM.)
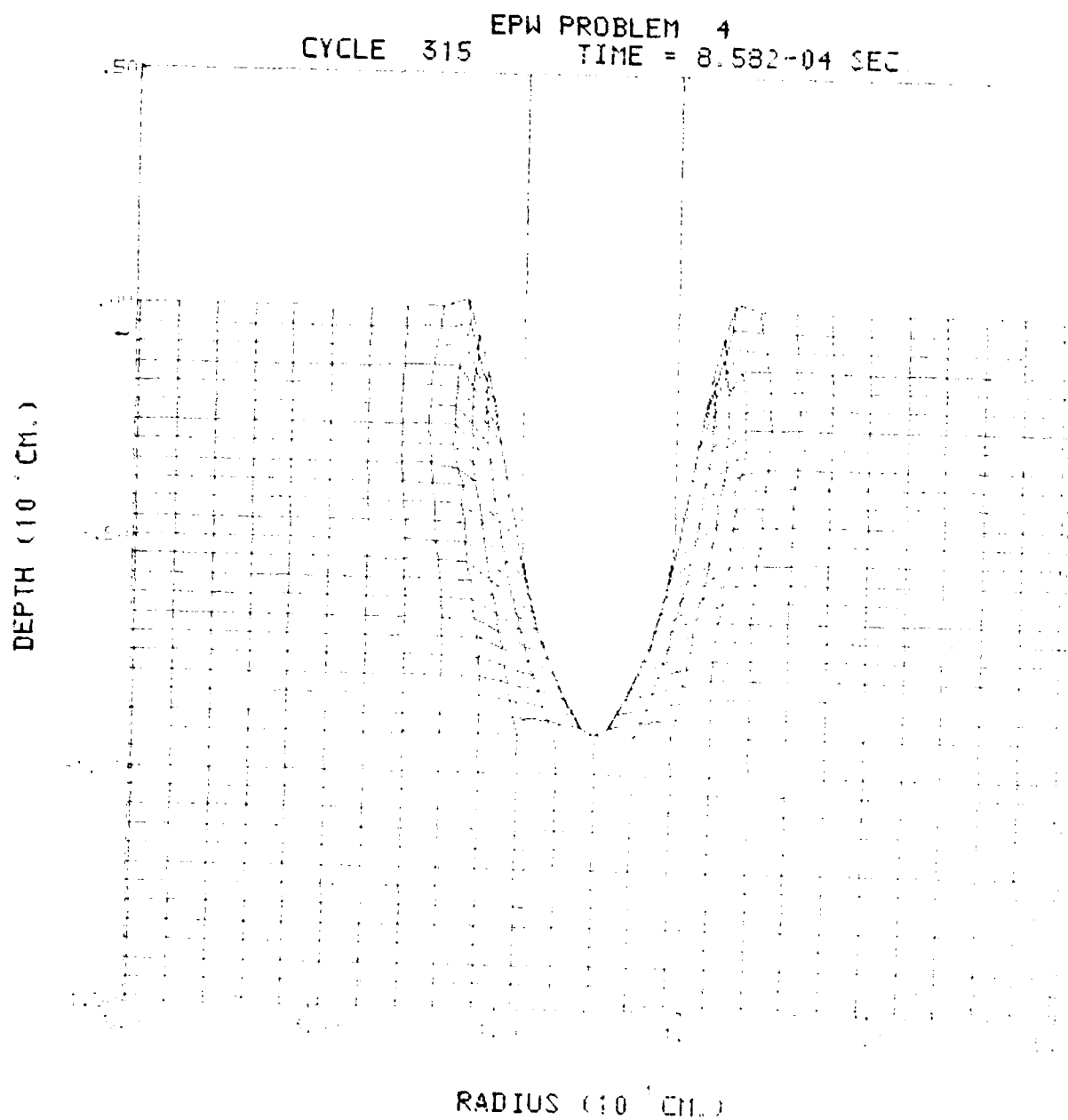
Figure 4.3-4e. Computing grid configuration at 6 ms for Case 4.

EPW PROBLEM 4
CYCLE   575   TIME = 1.146-03 SEC
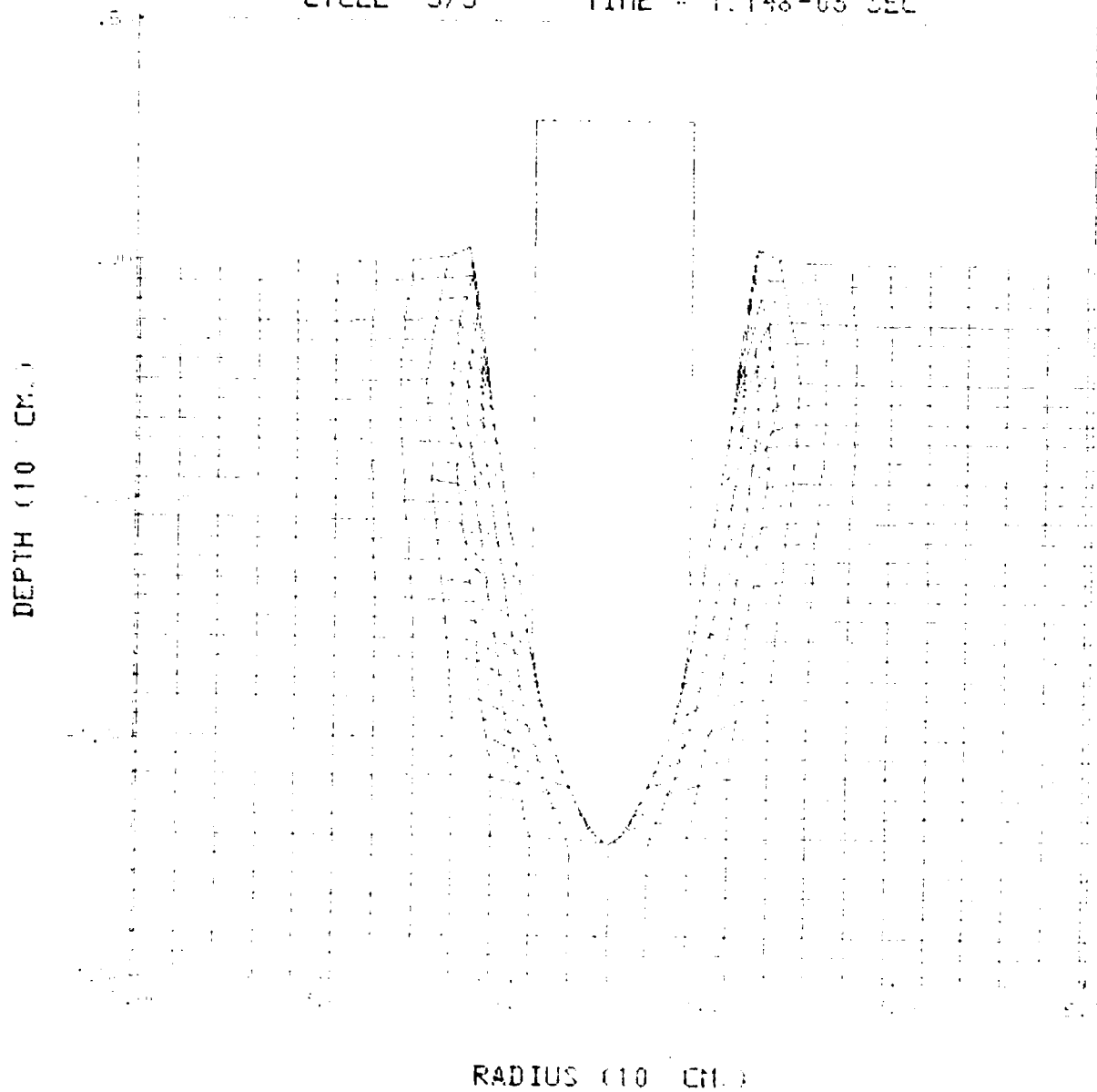
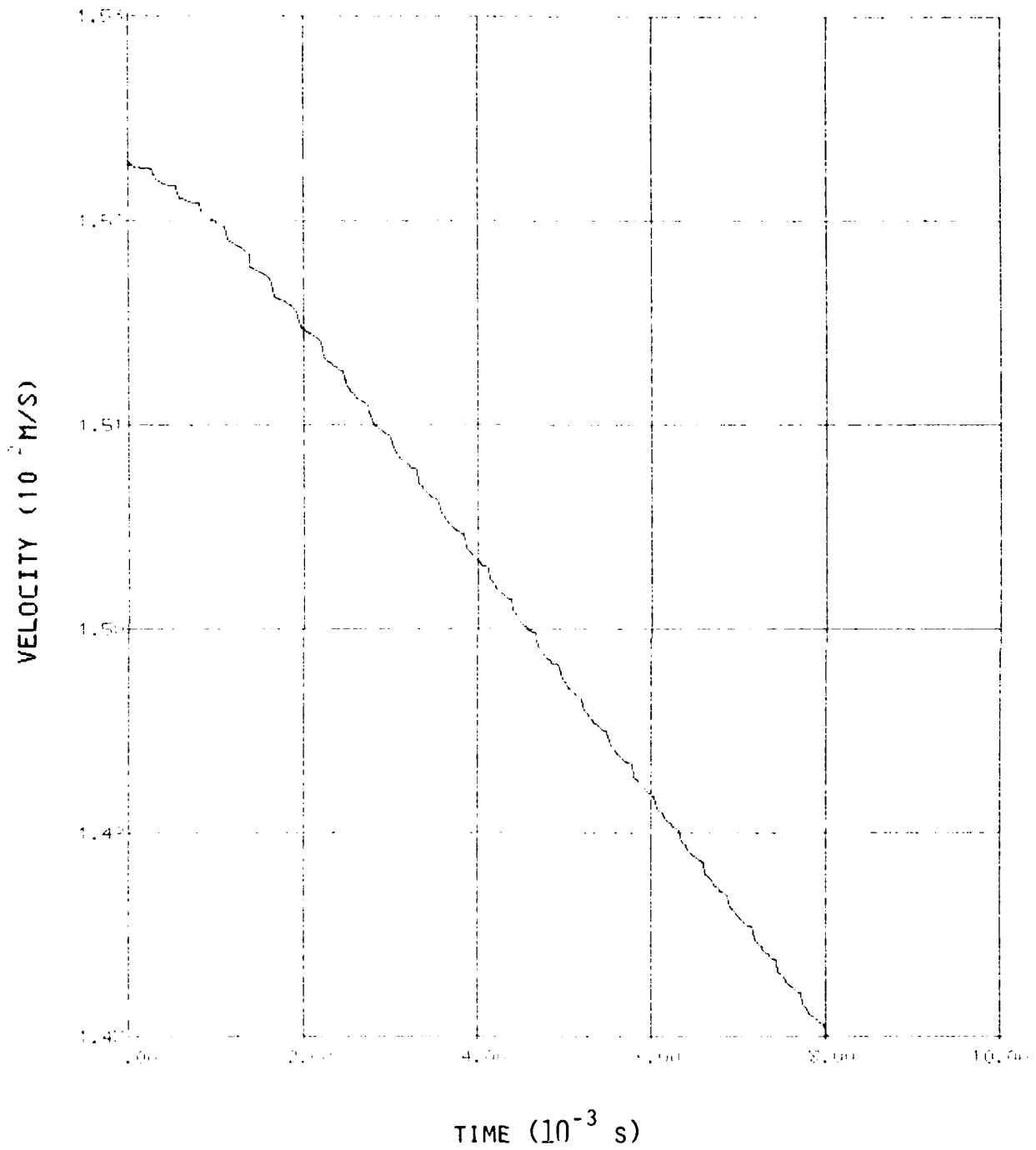Figure 4.3-4f.   Computing grid configuration at 8 ms for Case 4.

91
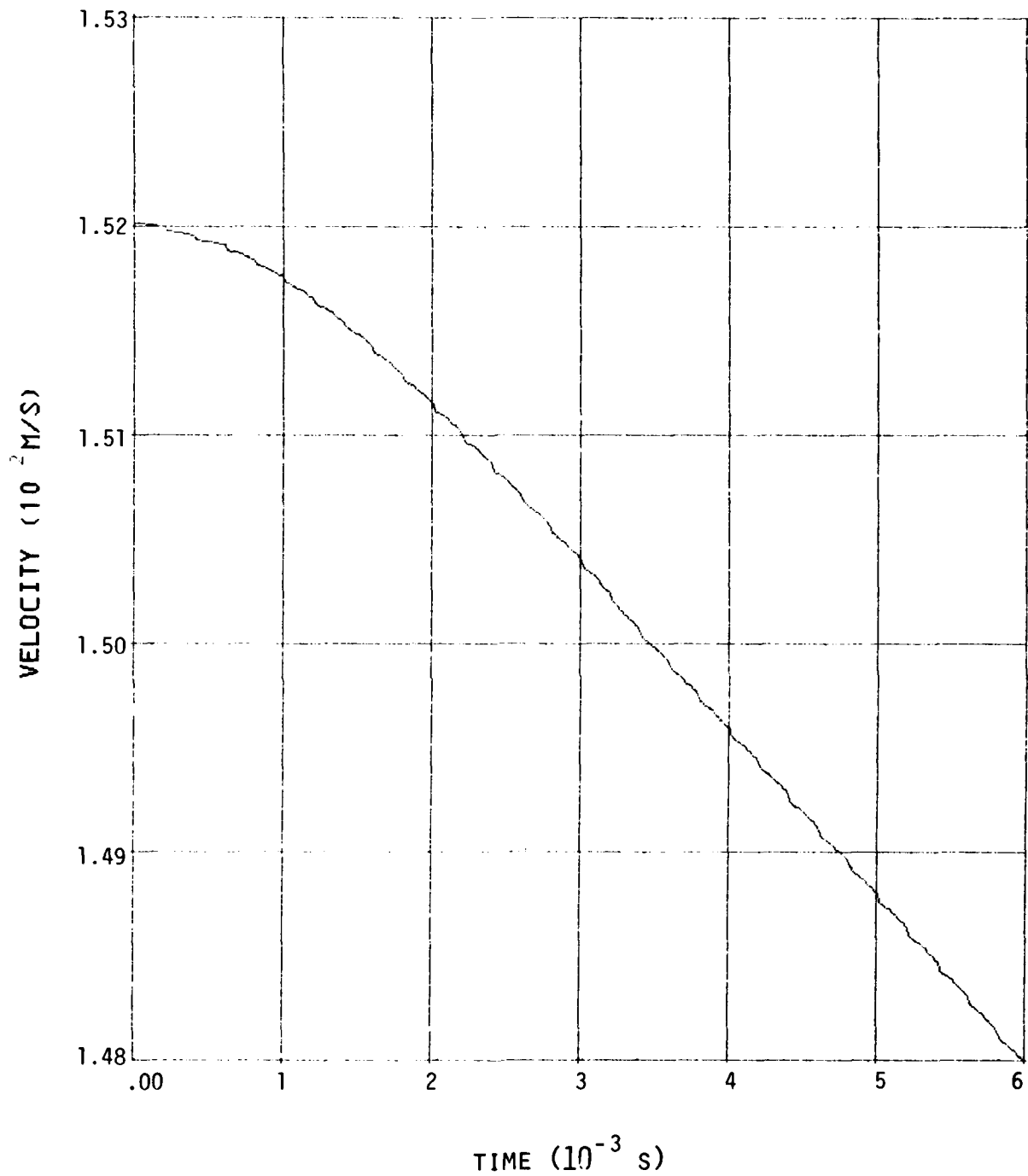
Figure 4.3-5a. Penetrator velocity history for Case 5.

EPW PROBLEM 5

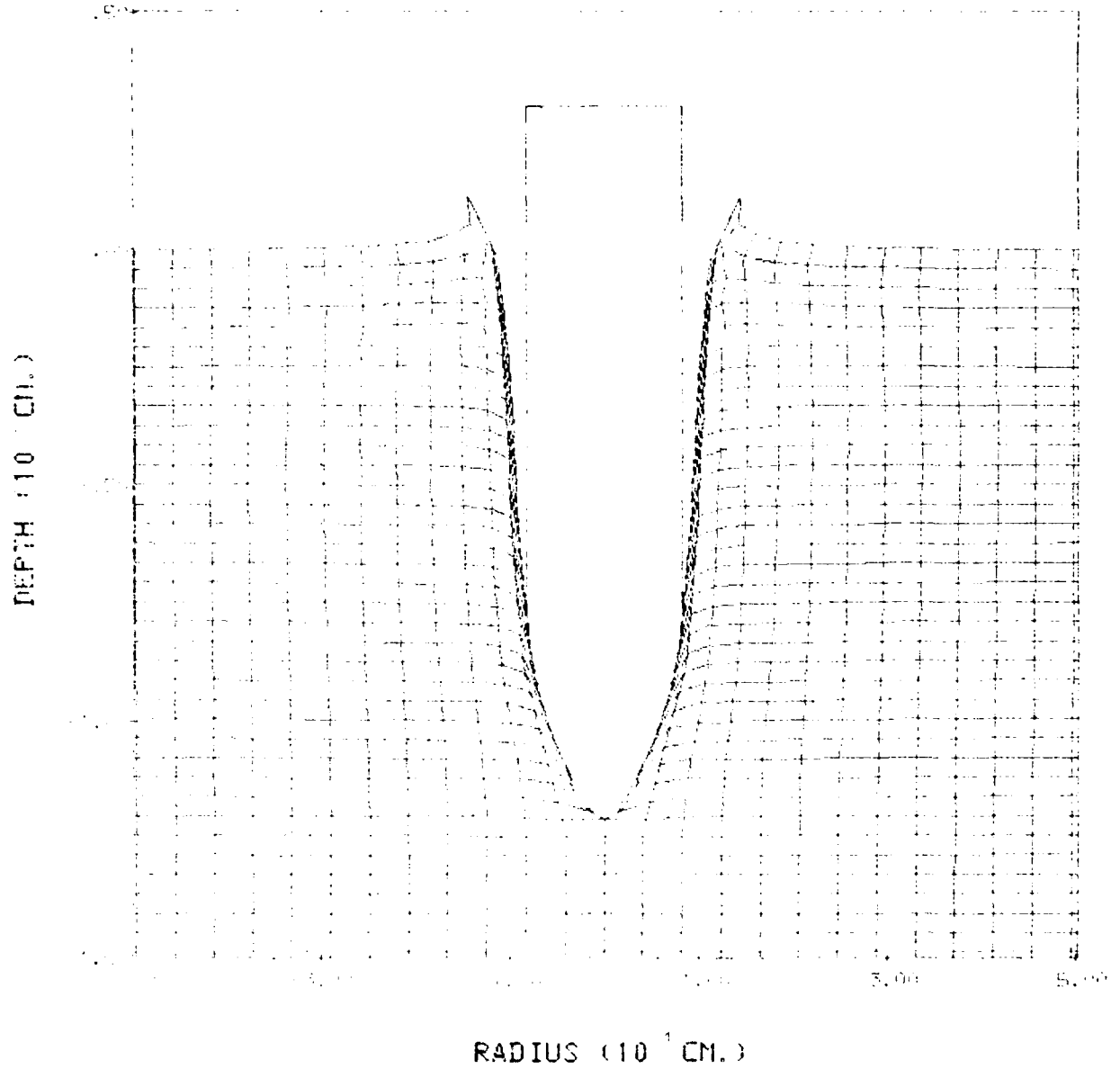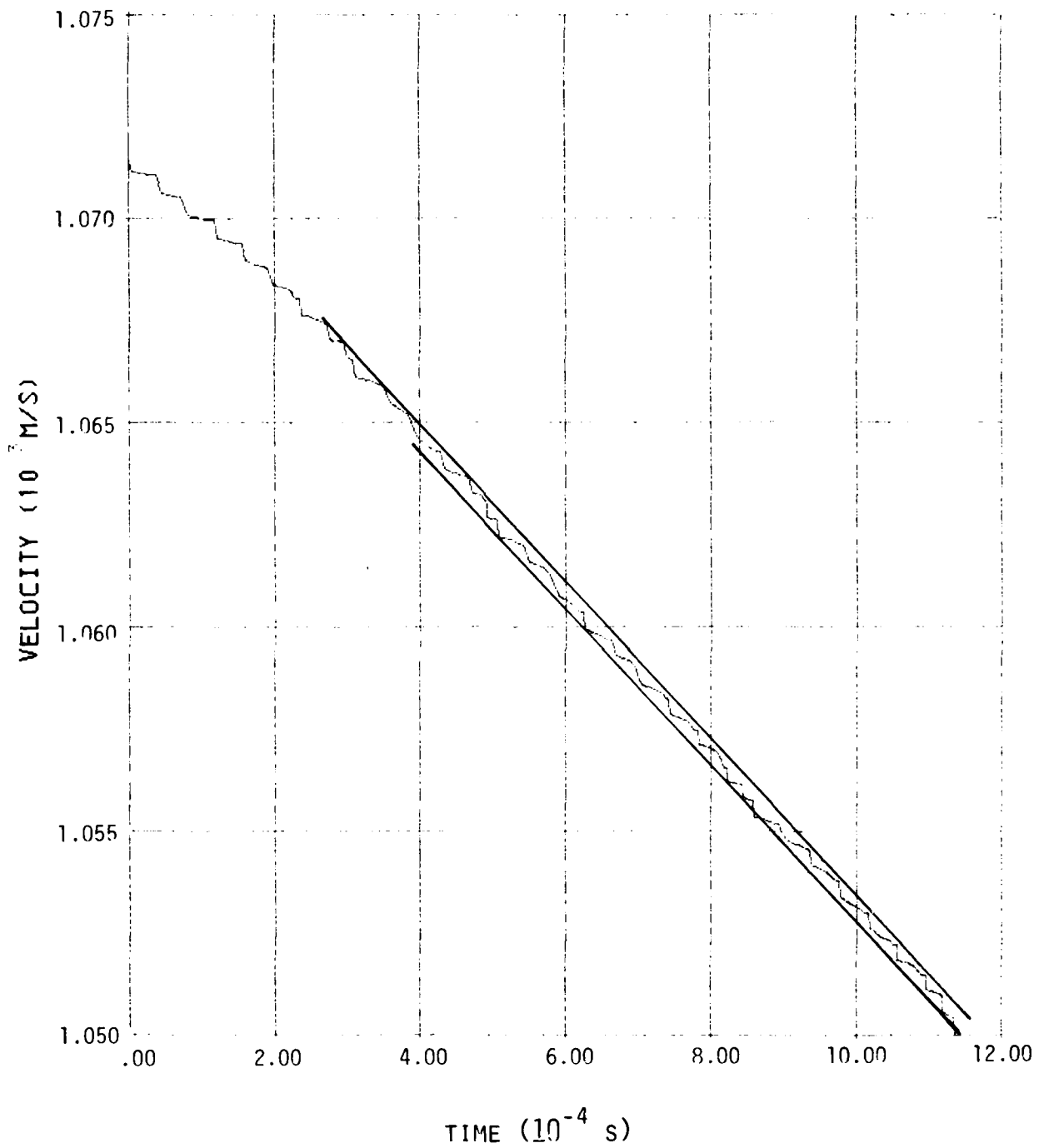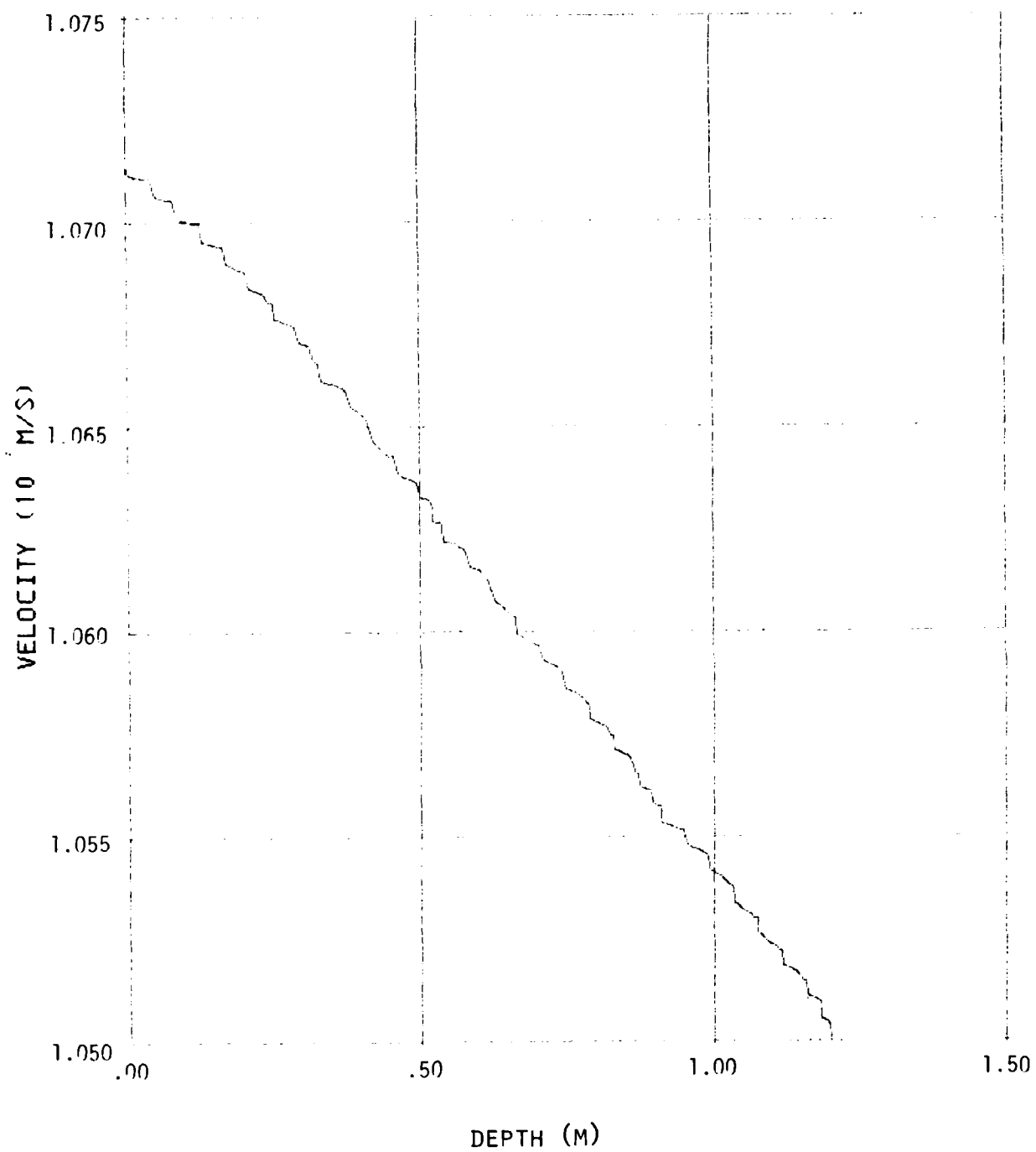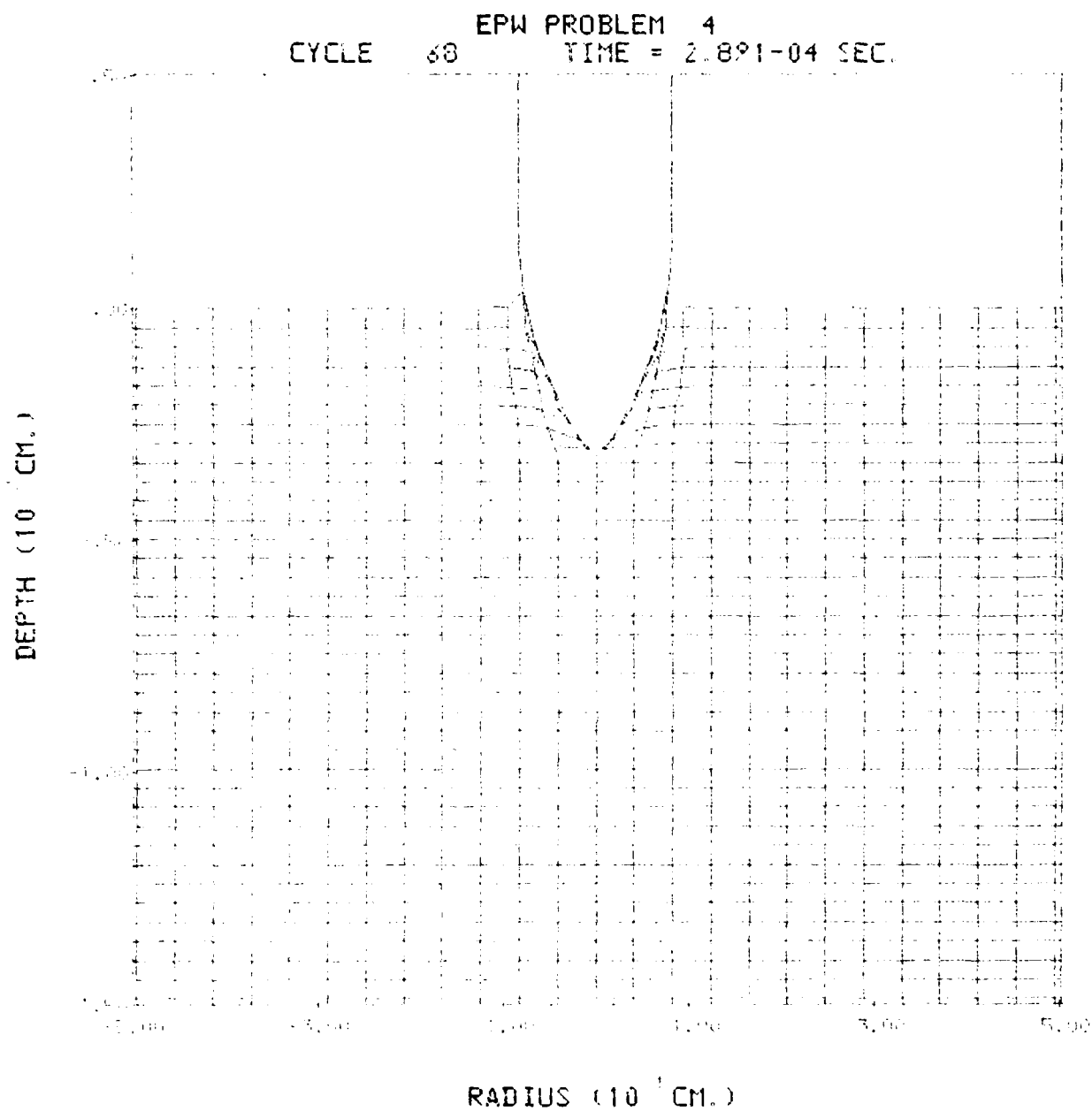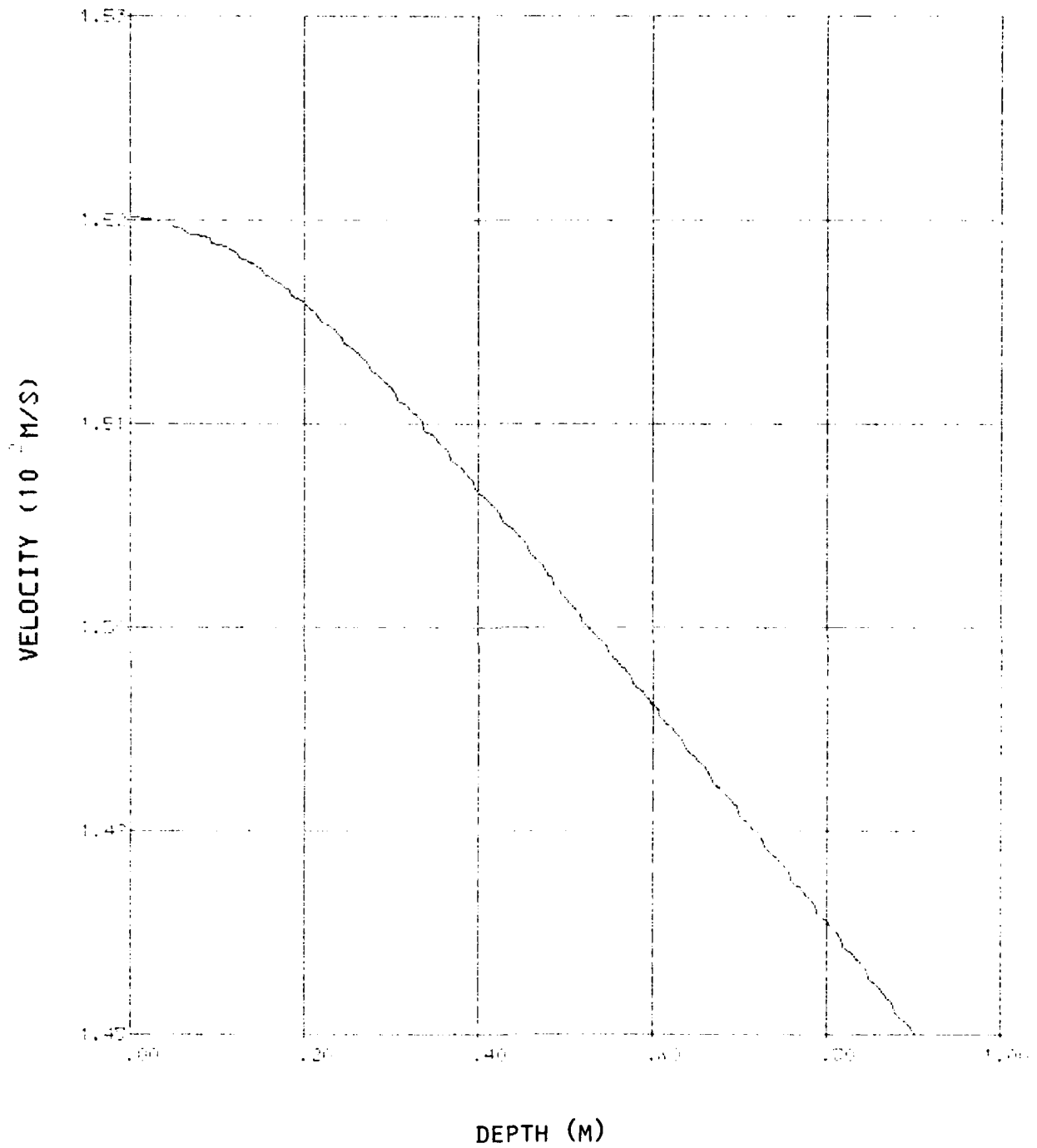Figure 4.3-5b.   Velocity penetrator depth cross plot for Case 5.

5. COMPARISON WITH EXPERIMENTAL DATA AND
OTHER COMPUTATIONS

For the purposes of computing the penetrator's structural response and deceleration, the most useful information which is obtained from these computations of rigid body penetration is the surface tractions which appear on the penetrator. These comprise the proper boundary conditions for other computations which seek to compute the stresses and deformation which arise within the vehicle, the wave propagation within it, and its structural response. The axial and radial components of the traction are presented in Figures 4.2-11 through 4.2-20.

There is no experimental data against which to compare these computed tractions. The measurements of soil stress made in the firings were taken so far from the vehicle that they are very insensitive to the stresses on the vehicle itself. The stress field in the soil decreases extremely rapidly with radial distance from the vehicle. The soil stress measurements were taken at a stress level of less than 3 bars in layer 1, and it appears hopeless to attempt to use them as a base from which to extrapolate back ⁺ the vehicle to find the forces on it.

The only other experimental data is the velocity-time history of the vehicle, which provides a measure of its deceleration. Since the deceleration is given by the integrated axial force on the vehicle divided by its mass, comparing the computed and measured deceleration has some relevance to the computed stresses. This comparison is conducted in Section 5.1. In Section 5.2 the computed tractions are compared with those resulting from previous computations.

5.1 COMPARISON OF THE MEASURED AND CALCULATED DECELERATION

The deceleration was measured by accelerometers which were carried on board the penetrator. The data were read out in two ways. First, the data was transmitted out in real time during the penetration process. Second, the data was recorded in an onboard memory unit during penetration, and was telemetered out after the penetrator came to rest. The two sets of data contain oscillations which are presently unexplained.

As our basis for comparison, we use the smoothed set of data[13] which is presented in Figure 5.1-1. In that figure, the data is approximated by straight-line segments which give the best fit to the onboard memory data which has been filtered to 200 Hz.

The decelerations computed in this study are 61.2 g's for the fill material (Case 3) and 81.9 g's for the material of layer 1 (Case 5). WES has identified that the top 3 to 5 feet of the firing site are composed of fill material, with the most representative depth being 4 feet. The next few feet beneath it are of layer 1 material. These decelerations are plotted in Figure 5.1-1 as the heavy dashed lines, and are to be compared with the measured deceleration for firing 06, which is shown as the heavy solid line in the figure. The computed decelerations compare favorably with the measured values, but are somewhat higher for both media.

As discussed in detail in Section 4.1, zone sizes of 3 or 4 centimeters are too large to resolve the flow about the blunted tip, and their use leads to values of deceleration which are too high. To determine the true decelerations, the calculations should be rerun using smaller zones. If this were done, many useful results would be obtained. If the correctly-computed decelerations proved to agree precisely with the measured values, it would indicate that the material property measurements conducted in WES provided sufficient data to compute penetrator decelerations in these soil types. In particular,
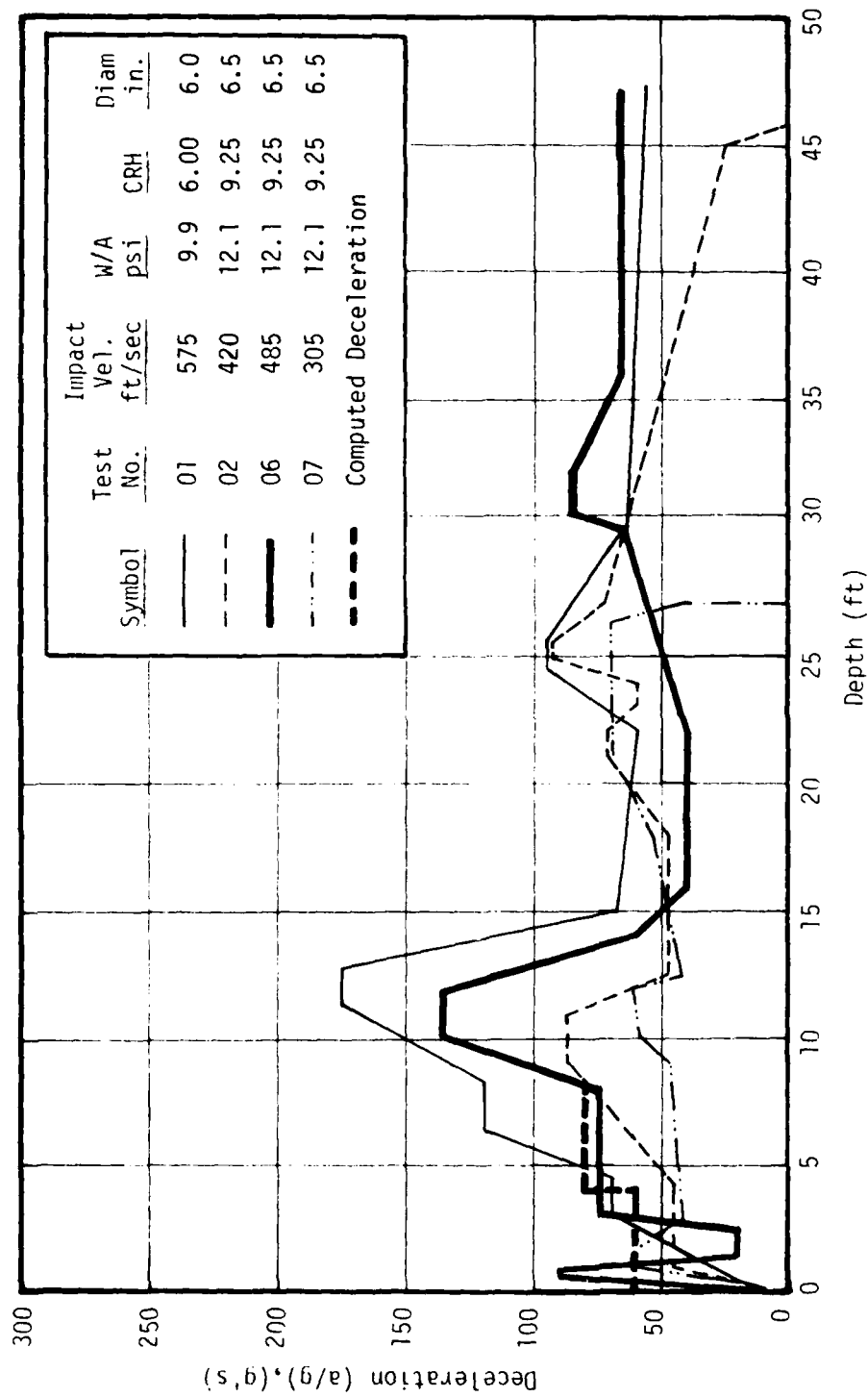
Fig. 5.1-1   Comparison between the computed and measured decelerations for firing 06 at the DRES. (Note that the measured deceleration exhibits a general increase with depth and peaks near 12 feet. The two layers computed reflect this increase, but the material near 12 feet must be used in a computation to obtain a comparison with the measured peak.)

it would not be necessary to include the effects of friction in the calculation. If, on the other hand, the correctly-computed decelerations turned out to be less than the measured values, one could determine the amount of friction which has to be included. It is recognized, of course, that such conclusions assume that the decelerations were accurately measured. If this turns out not to be true, the conclusions would be deferred until correct measurements were taken.

Before the present study was conducted, the opinion had been expressed by others that it was not economically feasible to utilize zones much smaller than 3 cm. It was feared that using small zones would require prohibitively large amounts of computer time. However, our research has resulted in greatly increased computing efficiency. For example, Case 5, in which three feet of penetration were computed using 3 cm zones, required less than $80 of computer time. Using smaller zones to compute the correct deceleration is therefore eminently feasible.

The measured decelerations in Figure 5.1-1 show that a peak of deceleration occurs in the interval between 8 and 13 feet. Peaks at about this same depth are present to some degree in all four of the tests conducted in this area, namely, Tests 01, 02, 06, and 07, whose parameters are called out in the legend of Figure 5.1-1. Data taken from nearby borings, and the pit which was excavated postshot,[13,14] show that a coarse-grained sandy layer occurs near a depth of 12 feet. It would be useful to conduct a computation using the properties of that layer, to see whether the deceleration peak would be reproduced by the computation. If it were, it would add further weight to our hypothesis that our computation, using laboratory data as an input, can predict the deceleration. The calculations in the first two layers show an increasing deceleration with depth. A successful computation of the deceleration near 12 feet would complete a tentative explanation of the increase of measured deceleration with depth, peaking at about 12 feet.

5.2 COMPARISONS WITH OTHER CALCULATIONS

In reviewing the previous computations,[14] it was found that
no two computations had been conducted with the same inputs. The
most similar computations had been conducted by SLA and CRT. However,
CRT had used a blunted tip, a rigid body approximation, and an
artificially-constructed model of friction. SLA had conducted two
usable computations. The first, which we call SLA-R, used a rigid
body, but had assumed a sharp-tipped complete ogive configuration for
the nose. Their second calculation, called SLA-D, used the blunt-tipped
configuration, but assumed that the body was deformable. Other
differences were:

1. Both SLA cases used a different fit of the soil
   properties than CRT, and the fits reflected substantially
   different soil properties.

2. Neither SLA computation included friction.

These inputs are summarized in Table 5-1.

TABLE 5-1

INPUTS TO COMPUTATIONS

(All these computations used Lagrangian codes)

	CRT	SLA-R	SLA-D	Case 1	Case 5
Rigid Body	yes	yes	no	yes	yes
Blunt Tip	yes	no	yes	yes	yes
Friction	yes	no	no	yes	no
Zone Size	4 cm	3 cm	3 cm	4 cm	3 cm
Material Model	CRT 1	SLA 1	SLA 1	CRT 1	CRT 1

CRT 1 denotes the CRT fit to layer 1 material.

SLA 1 denotes the SLA fit to layer 1 material.

For these reasons the computational review[14] concluded that it was not relevant to conduct detailed comparisons between the CRT and SLA computations.

Case 1 of the present study was designed to simulate the CRT calculation as closely as possible. It is therefore relevant to conduct comparisons between the surface tractions calculated in Case 1 and by CRT. This is done in Section 5.2.1.

Case 5 of this study uses the same vehicle configuration as SLA-D, and the same zone size. Like the SLA case, no friction is included. The major differences between the two computations are that SLA-D used a deformable body, and a different soil model. Therefore, it is less relevant to compare Case 5 with SLA-D, but some qualitative comparisons are conducted in Section 5.2.2.

5.2.1 Comparison with the CRT Calculation

The inputs of Case 1 simulated those of the CRT calculation as closely as possible. It is therefore relevant to conduct comparisons between the stresses calculated in the two studies.

Both calculations used the same vehicle geometry (blunted-tip), same soil material (in fact the CRT fit was used in Case 1), the same zone size, and the same physical model of friction. Specifically, the shearing stress on the vehicle is set to

$$\tau = \text{Min}\left[0.6\sigma_n, 0.6\,\frac{Y^{(\sigma_n)}}{\sqrt{3}}\right] \tag{1}$$

Figure 5.2-1 compares the normal stress* on the vehicle given by the two computations, and Figure 5.2-2 compares the computations of tangential stress.* The results for the present study were obtained by summing the appropriate components of the axial and radial tractions shown in Figure 4.2-11 and 12.

---

*While the terms "normal stress" and tangential stress" are coming into common usage, they actually refer to the normal and tangential components of surface traction.
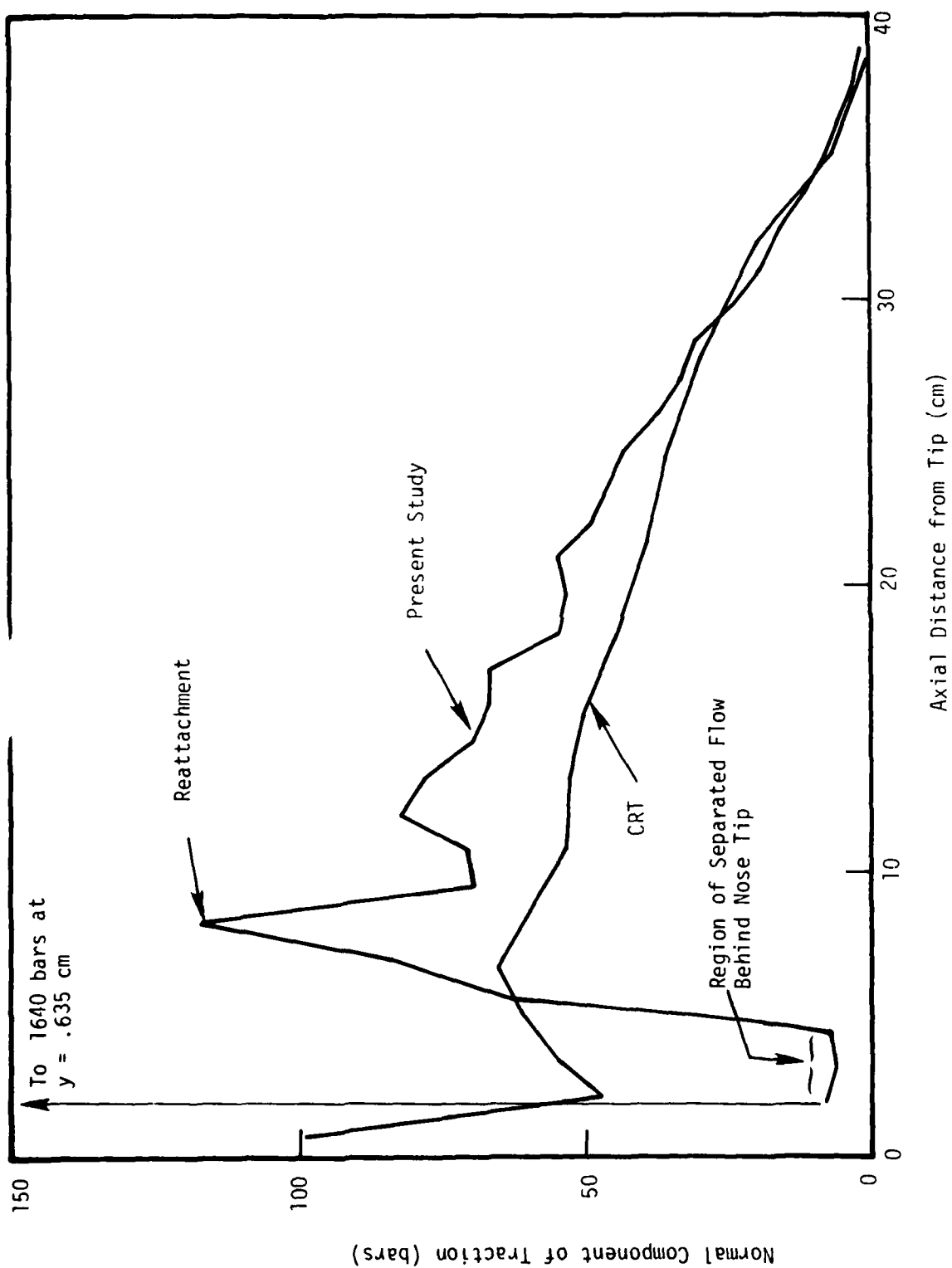
99

Figure 5.2-1. Comparison of normal component of surface traction as computed in this study (Case 1) and by CRT. [10]
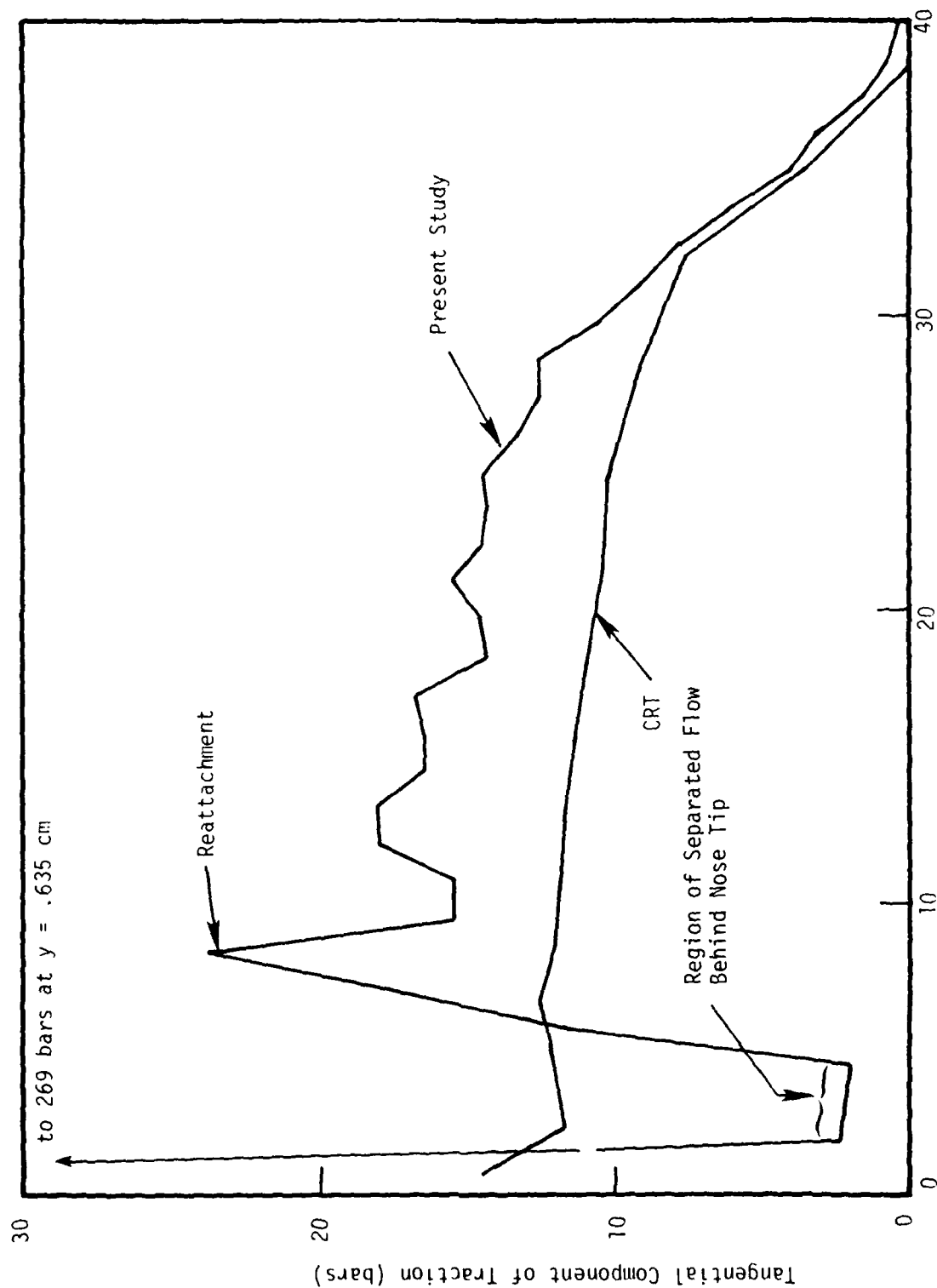
Figure 5.2-2. Comparison of tangential component of surface traction as computed in this study (Case 1) and by CRT. [10]

It may be seen that the results are different in several respects. First, the normal stress computed in this study is in general higher than that computed by CRT. The most important reason for this is that the present study utilizes an algorithm which provides a stress on the vehicle itself, whereas the CRT computation used the stresses in the centers of the computing cells adjacent to the vehicle. Because the stress in the soil varies extremely rapidly with distance from the vehicle, this tends to cause CRT to underestimate the stress. Secondly, the computing algorithms utilized by CRT did not permit the soil to separate from the vehicle as it flowed around the blunted tip. Thus, the region of small stress which occurs just above the conical tip in the present study is not reflected in the CRT result.

The agreement between the two computations of stress becomes better with increasing distance from the penetrator tip. The agreement becomes very good at about 30 cm from the tip, and both computations show that little, if any, stress is present at distances greater than 40 cm from the tip. Inasmuch as the stress gradients in the soil are very large near the tip, and become smaller as one moves back along the penetrator, this variation in agreement is precisely what one would expect.

In the CRT computation, computing nodes which encounter the blunted tip are imparted the velocity necessary to keep them on the tip. This procedure increases the momentum in the soil, but does not decrease the momentum in the penetrator. The decrease in penetrator momentum comes only when the motions produced in the soil generate strains, which results in stresses in the computing grid. The net effect is to produce more axial momentum in the soil than the penetrator has lost. The final result is that the deceleration of and the tractions on the penetrator are underestimated.

One would therefore expect that reducing the grid size in the CRT computations would lead to larger computed decelerations and larger tractions on the penetrator, because the errors which cause the underestimate are reduced thereby. For the reasons discussed in Section 4.2, reducing the grid size in the present study would lead to smaller

decelerations, smaller tractions on the conical tip, and a different traction distribution on the ogive. It is therefore anticipated that the decelerations computed by CRT and those of the present study provide upper and lower bounds on the correct deceleration.

5.2.2   Comparison with the SLA Computation

In this section, we discuss SLA deformable body calculation, which is Case SLA-D in Table 5.1. The inputs for this computation were discussed in Section 5.2.

In the SLA deformable body calculation, the interaction between the soil and the penetrator is accomplished using a slide line formulation similar to that of Wilkins.[16] The slide line formulation permits differential motion between the soil and penetrator, but computes the stresses which arise in both media. The formulatio. used by SLA does not permit the soil to separate from the penetrator   Therefore, as in the CRT calculation, soil nodes which encounter the proiectile are imparted the velocity necessary to keep them on the blunted tip. The essential difference is that the stress in the penetrator required to produce the soil acceleration is taken into account. The stresses are the agency which impart momentum to the soil, and by Newton's third law impart an equal and opposite momentum to the projectile. Therefore, in the SLA computation, the momentum acquired by the soil comes at the expense of a momentum loss of the projectile. The computing algorithms of the calculations presented here accomplish the same end, even though a rigid body is used.

The SLA computations used 3 cm computing cells. For the reasons discussed in Section 4.2, use of these large computing cells causes the momentum imparted to the soil to be overestimated, which tends to overestimate the vehicle deceleration. In addition the large cells should generate stresses on the blunted tip of the same order as those which were computed in the present study. As shown in Table 4.2-1, the time-average value of the surface axial surface traction for Case 5 is

.678 kbars, and substantial oscillations about the average value occurred. The oscillations in traction are generated as each cell encounters the blunted tip, and we would expect the same phenomena to be present in the SLA computation. This would cause large oscillation of the stress and strain fields within the projectile. An examination of the computed SLA data confirms that this is true. The oscillations in the velocity field within the penetrator were sufficiently large to mask the computed deceleration. In addition, mean stresses as high as 1.02 kbars and octahedral shear stresses as high as 2.9 kbars were computed within the penetrator.

Because only the pressure (mean stress) and octahedral shear stress are available in the SLA results, it is not possible to determine the surface tractions and conduct a comparison.

Our interpretation of these results is that much finer zoning in the soil would be required in the SLA computations to compute the correct stresses within the vehicle and its deceleration.

6. REFERENCES

1.   Patterson, W. J., DNA/Sandia Soil Penetration Experiment
      at DRES Results and Analysis, Sandia Laboratories,
      Albuquerque, New Mexico, SAND-75-0001, January 1975.

2.   Jackson, J. G. Jr., Physical Property and Dynamic Compress-
      ibility Analysis of the Watching Hill Blast Range, U. S.
      Army Engineer Waterways Experiment Station, Vicksburg,
      Mississippi, Technical Report S-72-4, April 1972.

3.   Letter, Jackson, J. G. Jr., Waterways Experiment Station
      to Distribution, Recommended Soil Profile and Properties
      for DNA Penetrator Test Site, DRES, Canada, March 25, 1974.

4.   Letter, Jackson, J. G. Jr., Waterways Experiment Station to
      Distribution, Soil Classification and Triaxial Shear Test
      Data for DNA Penetrator Test Site, DRES, Canada, May 30, 1974.

5.   Rohani, B., "Pretest Penetration Calculations for DNA
      Earth Penetrator Experiments at DRES, Canada"; (unpublished
      report), June 1974; U. S. Army Engineer Waterways Experiment
      Station, CE, Vicksburg, Miss.; (transmitted by letter to
      Director, Defense Nuclear Agency, ATTN: SPSS, from
      J. G. Jackson, Jr., dated 20 June 1974).

6.   Bernard, R. S. and S. V. Hanagud; "Development of a
      Projectile Penetration Theory; Penetration Theory for
      Shallow to Moderate Depths"; Technical Report (in preparation);
      U. S. Army Engineer Waterways Experiment Station, CE,
      Vicksburg, Mississippi.

7.   Norwood; "Section V, Analytical Calculations" (unpublished
      technical note handed out at WES on 23 July 1974); Sandia
      Laboratories, Albuquerque, New Mexico.

8.   Allen, R. T.; "Prediction of the Deceleration of an Earth
      Penetrating Vehicle"; Informal Report SSS-IR-74-2192,
      April 1974; Systems, Science and Software, La Jolla,
      California.

9.   AVCO Corporation; "Impact and Penetration Study Program
      Final Report"; Contract No. DNA-001-74-C-0233 (draft),
      July 1974; Wilmington, Massachusetts.

REFERENCES (CONT'D.)

10. Wagner, M. H., et al., "Numerical Analysis of DNA Earth
    Penetrator Experiment at DRES, "California Research &
    Technology, Inc. CRT 2050-2, October 1974.

11. Byers, R. K., et al., "Predictions of Projectile Penetration
    Phenomena and comparison with experiments in a Soil
    Medium, SAND 75-0174, April 1975.

12. Orphal, D. L., et al., "A Computation of a DNA Earth
    Penetration Experiment at the Watching Hill Site, DRES,
    Canada," Physics International Report PIFR-678, DNA Contract
    DNA001-74-C-0223. December. 1974.

13. Hadala, P. F., "Evaluation of Empirical and Analytical
    Procedures Used for Predicting the Rigid Body Motion of
    an Earth Penetrator," U. S. Army Engineer Waterways
    Experiment Station, Miscellaneous Paper S-75-15, June, 1975.

14. Bjork, R. L., "A Review of Earth Penetrating Weapon
    Calculations," Pacifica Technology Report PT-U75-0013,
    DNA Contract DNA001-75-C-0148, May, 1975.

15. Letter, Hadala, P. F., Waterways Experimental Station to
    R. L. Bjork, Pacifica Technology, dated 8 August 1975.

16. Wilkins, M. L., "Calculation of Elastic-Plastic Flow,"
    Methods in Computational Physics, edited by Alder, B.,
    et al., Academic Press, New York (1964). p. 211ff.

DISTRIBUTION LIST

DEPARTMENT OF DEFENSE

Director
Defense Advanced Research Proj. Agency
    ATTN: Technical Library

Director
Defense Civil Preparedness Agency
Assistant Director for Research
    ATTN: Admin. Officer

Defense Documentation Center
Cameron Station
12 cy ATTN: TC

Director
Defense Intelligence Agency
    ATTN: Technical Library
    ATTN: DT-2, Wpns. & Sys. Div.
    ATTN: DB-4C, Edward O'Farrell
    ATTN: DI-7E
    ATTN: Charles A. Fowler

Director
Defense Nuclear Agency
 5 cy ATTN: SPSS
    ATTN: TISI, Archives
 3 cy ATTN: TITL, Tech. Library
    ATTN: DDST
    ATTN: SPAS

Dir. of Defense Rsch. & Engineering
Department of Defense
    ATTN: S&SS (OS)

Commander
Field Command
Defense Nuclear Agency
    ATTN: FCPR

Director
Interservice Nuclear Weapons School
    ATTN: Document Control

Director
Joint Strat. Target Planning Staff, JCS
    ATTN: STINFO, Library

Chief
Livermore Division, Field Command, DNA
Lawrence Livermore Laboratory
    ATTN: FCPRL

DEPARTMENT OF THE ARMY

Dep. Chief of Staff for Research Dev. & Acq.
Department of the Army
    ATTN: DAMA-CSM-N, LTC G. Ogden
    ATTN: Technical Library
    ATTN: DAMA(CS), MAJ A. Gleim

Chief of Engineers
Department of the Army
 2 cy ATTN: DAEN-MCE-D
 2 cy ATTN: DAEN-RDM

DEPARTMENT OF THE ARMY (Continued)

Deputy Chief of Staff for Ops. & Plans
Department of the Army
    ATTN: Technical Library
    ATTN: Dir. of Chem. & Nuc. Ops.

Chief
Engineer Strategic Studies Group
    ATTN: DAEN-FES

Commander
Frankford Arsenal
    ATTN: L. Baldini

Project Manager
Gator Mine Program
    ATTN: E. J. Linddsey

Commander
Harry Diamond Laboratories
    ATTN: DRXDO-NP
    ATTN: DRXDO-RBH, James H. Gwaltney

Commander
Picatinny Arsenal
    ATTN: Ray Moesner
    ATTN: Technical Library
    ATTN: SMUPA-AD-D-A
    ATTN: SMUPA-AD-D-A-7
    ATTN: Ernie Zimpo
    ATTN: Paul Harris
    ATTN: P. Angelloti
    ATTN: Jerry Pental
    ATTN: Marty Margolin
    ATTN: SMUPA-AD-D-M
    ATTN: DR-DAR-L-C-FA, B. Shulman

Commander
Redstone Scientific Information Center
US Army Missile Command
    ATTN: Chief, Documents

Commander
US Army Armament Command
    ATTN: Tech. Lib.

Director
US Army Ballistic Research Labs.
    ATTN: DRXBR-TB
 2 cy ATTN: Tech. Lib., Edward Baicy
    ATTN: DRDAR-BLE, J. H. Keefer
    ATTN: DRXBR-X
    ATTN: A. Ricchiazzi
    ATTN: G. Roecker
    ATTN: G. Grabarek
    ATTN: J. W. Apgar

Commander & Director
US Army Cold Region Res. Engr. Lab.
    ATTN: G. Swinzow

Commander
US Army Comb. Arms Combat Dev. Acty.
    ATTN: LTC G. Steger
    ATTN: LTC Pullen

DEPARTMENT OF THE ARMY (Continued)

Commander
US Army Engineer Center
    ATTN: ATSEN-SY-L

Division Engineer
US Army Engineer Div. Huntsville
    ATTN: HNDED-SR

Division Engineer
US Army Engineer Div. Missouri Rvr.
    ATTN: Tech. Library

Commandant
US Army Engineer School
    ATTN: ATSE-CTD-CS
    ATTN: ATSE-TEA-AD

Director
US Army Engr. Waterways Exper. Sta.
    ATTN: Leo Ingram
    ATTN: D. K. Butler
    ATTN: P. Hadala
    ATTN: Guy Jackson
    ATTN: John N. Strange
    ATTN: Technical Library
    ATTN: William Flathau
    ATTN: Behzad Rohani

Commander
US Army Mat. & Mechanics Research Center
    ATTN: *Technical Library*

Commander
US Army Materiel Dev. & Readiness Cmd.
    ATTN: Technical Library

Director
US Army Materiel Sys. Analysis Acty.
    ATTN: Joseph Sperazza

Commander
US Army Missile Command
    ATTN: F. Fleming
    ATTN: W. Jann
    ATTN: J. Hogan

Commander
US Army Mobility Equip. R & D Center
    ATTN: STSFB-XS
    ATTN: Technical Library
    ATTN: STSFB-MW

Commander
US Army Nuclear Agency
    ATTN: Doc. Con.
    ATTN: Tech. Lib.

Commander
US Army Training & Doctrine Command
    ATTN: LTC Auveduti, COL Enger
    ATTN: LTC J. Foss

Commandant
US Army War College
    ATTN: Library

US Army Mat. Cmd. Proj. Mngr. for Nuc. Munitions
    ATTN: DRCPM-NUC

DEPARTMENT OF THE NAVY

Chief of Naval Operations
Navy Department
    ATTN: OP 982, LCDR Smith
    ATTN: OP 982, CAPT Toole
    ATTN: Code 604C3, Robert Piacesi
    ATTN: OP 982, LTC Dubac

Chief of Naval Research
Navy Department
    ATTN: Technical Library

Officer in Charge
Civil Engineering Laboratory
Naval Construction Battalion Center
    ATTN: R. J. Odello
    ATTN: Technical Library

Commandant of the Marine Corps
Navy Department
    ATTN: POM

Commanding General
Development Center
Fire Support Branch
MCDEC
    ATTN: LTC Gapenski
    ATTN: CAPT Hartneady

Commander
Naval Air Systems Command
Headquarters
    ATTN: F. Marquardt

Commanding Officer
Naval Explosive Ord. Disposal Fac.
    ATTN: Code 504, Jim Petrousky

Commander
Naval Facilities Engineering Command
Headquarters
    ATTN: Technical Library

Superintendent (Code 1424)
Naval Postgraduate School
    ATTN: Code 2124, Tech. Rpts. Librarian

Director
Naval Research Laboratory
    ATTN: Code 2600, Tech. Lib.

Commander
Naval Sea Systems Command
Navy Department
    ATTN: ORD-033
    ATTN: SEA-9931G

Officer in Charge
Naval Surface Weapons Center
    ATTN: Code WX21, Tech. Lib.
    ATTN: Code WA501, Navy Nuc. Prgms. Off.
    ATTN: M. Kleinerman

Commander
Naval Surface Weapons Center
Dahlgren Laboratory
    ATTN: Technical Library

DEPARTMENT OF THE NAVY (Continued)

Commander
Naval Weapons Center
 ATTN: Carl Austin
 ATTN: Code 533, Tech. Lib.

Commanding Officer
Naval Weapons Evaluation Facility
 ATTN: Technical Library

Director
Strategic Systems Project Office
Navy Department
 ATTN: NSP-43, Tech. Lib.

DEPARTMENT OF THE AIR FORCE

AF Armament Laboratory, AFSC
 ATTN: Masey Valentine
3 cy ATTN: John Collins, AFATL/DLYV
 ATTN: Maj Thomas Tomasetti
 ATTN: William Cramer

AF Institute of Technology, AU
 ATTN: Library AFIT Bldg. 640, Area B

AF Weapons Laboratory, AFSC
 ATTN: SUL

Headquarters
Air Force Systems Command
 ATTN: Technical Library

Commander
Armament Development & Test Center
 ATTN: Tech. Library

Assistant Secretary of the Air Force
Research & Development
Headquarters, US Air Force
 ATTN: Col R. E. Steere

Deputy Chief of Staff
Research & Development
Headquarters, US Air Force
 ATTN: Col J. L. Gilbert

Commander
Foreign Technology Division, AFSC
 ATTN: NICD, Library

Hq. USAF/IN
 ATTN: INATA

Hq. USAF/RD
 ATTN: RDPM

Oklahoma State University
Fld. Off. for Wpns. Effectiveness
 ATTN: Edward Jackett

Commander
Rome Air Development Center, AFSC
 ATTN: EMTLD, Doc. Library

SAMSO/RS
 ATTN: RSS

ENERGY RESEARCH & DEVELOPMENT ADMINISTRATION

Division of Military Application
US Energy Research & Dev. Admin.
 ATTN: Doc. Con. for Test Office

University of California
Lawrence Livermore Laboratory
 ATTN: Jerry Goudreau
 ATTN: Mark Wilkins, L-504
 ATTN: Tech. Info. Dept. L-3

Los Alamos Scientific Laboratory
 ATTN: Doc. Con. for Tom Dowler
 ATTN: Doc. Con. for Reports Lib.

Sandia Laboratories
Livermore Laboratory
 ATTN: Doc. Con. for Tech. Library

Sandia Laboratories
 ATTN: Doc. Con. for William Caudle
 ATTN: Doc. Con. for W. Altsmeirer
 ATTN: Doc. Con. for 3141, Sandia Rpt. Coll.
 ATTN: Doc. Con. for John Colp
 ATTN: Doc. Con. for William Patterson
 ATTN: Doc. Con. for Walter Herrmann
 ATTN: Doc. Con. for John Keizur

US Energy Rsch. & Dev. Admin.
Albuquerque Operations Office
 ATTN: Doc. Con. for Tech. Library

US Energy Rsch. & Dev. Admin.
Division of Headquarters Services
Library Branch G-043
 ATTN: Doc. Con. for Class Tech. Lib.

US Energy Rsch. & Dev. Admin.
Nevada Operations Office
 ATTN: Doc. Con. for Tech. Lib.

OTHER GOVERNMENT AGENCIES

NASA
Ames Research Center
 ATTN: Robert W. Jackson

Office of Nuclear Reactor Regulation
Nuclear Regulatory Commission
 ATTN: Robert Heineman
 ATTN: Lawrence Shao

DEPARTMENT OF DEFENSE CONTRACTORS

Aerospace Corporation
 ATTN: Tech. Info. Services

Agbabian Associates
 ATTN: M. Agbabian

Applied Theory, Inc.
2 cy ATTN: John G. Trulio

Avco Research & Systems Group
 ATTN: David Henderson
 ATTN: Research Lib. A830, Rm. 7201
 ATTN: Pat Grady

DEPARTMENT OF DEFENSE CONTRACTORS (Continued)

Battelle Memorial Institute
    ATTN: Technical Library

The BDM Corporation
    ATTN: Technical Library

The Boeing Company
    ATTN: Aerospace Library

California Research & Technology, Inc.
    ATTN: Ken Krew hagen
    ATTN: Technical brary

Civil/Nuclear Systems
    ATTN: Robert Cra c

EG&G, Inc.
Albuquerque Division
    ATTN: Technical Library

Engineering Societies Library
    ATTN: Ann Mott

General Dynamics Corp.
Pomona Division
    ATTN: Keith Anderson

General Electric Company
TEMPO-Center for Advanced Studies
    ATTN: DASIAC

Georgia Institute of Technology
Georgia Tech. Research Institute
    ATTN: S. V. Hanagud
    ATTN: L. W. Rehfield

Honeywell Incorporated
Defense Systems Division
    ATTN: T. N. Helvig

Institute for Defense Analyses
    ATTN: IDA Librarian, Ruth S. Smith

Kaman AviDyne
Division of Kaman Sciences Corp.
    ATTN: Norman P. Hobbs
    ATTN: E. S. Criscione
    ATTN: Technical Library

Kaman Sciences Corporation
    ATTN: Library

Lockheed Missiles & Space Company, Inc.
    ATTN: M. Culp
    ATTN: Technical Library

Lockheed Missiles & Space Company, Inc.
    ATTN: Tech. Info. Center, D/COLL

Martin Marietta Aerospace
Orlando Division
    ATTN: Al Cowen
    ATTN: H. McQuaig
    ATTN: M. Anthony

DEPARTMENT OF DEFENSE CONTRACTORS (Continued)

Merritt Cases, Incorporated
    ATTN: Technical Library
    ATTN: J. L. Merritt

University of New Mexico
Dept. of Campus Security & Police
    ATTN: G. E. Triandafalidis

Nathan M. Newmark
Consulting Engineering Services
    ATTN: Nathan M. Newmark
    ATTN: William J. Hall

Pacifica Technology
    ATTN: G. Kent
    ATTN: R. Bjork

Physics International Company
    ATTN: Doc. Con. for Charles Godfrey
    ATTN: Doc. Con. for Tech. Lib.
    ATTN: Doc. Con. for Larry A. Behrmann
    ATTN: Doc. Con. for Dennis Orphal

R & D Associates
    ATTN: Arlen Fields
    ATTN: J. G. Lewis
    ATTN: Henry Cooper
    ATTN: Cyrus P. Knowles
    ATTN: Technical Library
    ATTN: William B. Wright, Jr.
    ATTN: Paul Rausch
    ATTN: Harold L. Brode

The Rand Corporation
    ATTN: Technical Library

Science Applications, Inc.
    ATTN: Technical Library

Stanford Research Institute
    ATTN: George R. Abrahamson

Systems, Science & Software, Inc.
    ATTN: Robert Sedgewick
    ATTN: Technical Library

Terra Tek, Inc.
    ATTN: Technical Library

TRW Defense & Space Sys. Group
    ATTN: Peter K. Dai, R1/2170
    ATTN: Tech. Info. Center/S-1930

TRW Defense & Space Sys. Group
San Bernardino Operations
    ATTN: E. Y. Wong, 527/712

Weidlinger Assoc. Consulting Engineers
    ATTN: J. M. McCormick
    ATTN: Melvin L. Baron

Weidlinger Assoc. Consulting Engineers
    ATTN: J. Isenberg